

See discussions, stats, and author profiles for this publication at: <http://www.researchgate.net/publication/24161468>

Radiometer Design Analysis Based Upon Measurement Uncertainty

ARTICLE *in* RADIO SCIENCE · FEBRUARY 2004

Impact Factor: 1.45 · DOI: 10.1029/2004RS003132 · Source: NTRS

CITATIONS

10

DOWNLOADS

44

VIEWS

91

2 AUTHORS, INCLUDING:



P. Racette

NASA

70 PUBLICATIONS 559 CITATIONS

SEE PROFILE

**RADIOMETER DESIGN ANALYSIS
BASED UPON MEASUREMENT UNCERTAINTY**

By

Paul Edward Racette

B.S. in Electrical Engineering, May 1988, University of Kansas
M.S. in Electrical Engineering, October 1990, University of Kansas

A Dissertation submitted to
The Faculty of
The School of Engineering and Applied Science
of The George Washington University in partial satisfaction
of the requirements for the degree of Doctor of Science

May 22, 2005

Dissertation directed by
Roger H. Lang
Professor of Electrical Engineering and Applied Science

ABSTRACT

This dissertation introduces a method for predicting the performance of a radiometer design based on calculating the measurement uncertainty. The variety in radiometer designs and the demand for improved radiometric measurements justify the need for a more general and comprehensive method to assess system performance. Radiometric resolution, or sensitivity, is a figure of merit that has been commonly used to characterize the performance of a radiometer. However when evaluating the performance of a calibration design for a radiometer, the use of radiometric resolution has limited application. These limitations are overcome by considering instead the measurement uncertainty. A method for calculating measurement uncertainty for a generic radiometer design including its calibration algorithm is presented. The technique entails decomposing a radiometer design into a set of subsystems from which a set of characteristic equations can be derived. The set of equations are used to form an estimator for the radiometer input. The expected value of the mean square error of the estimator is the measurement uncertainty and is the basis for quantitative comparative analysis. The result is a generalized technique by which system calibration architectures and design parameters can be evaluated to optimize instrument performance for given requirements and constraints. Least squares regression is presented as a framework by which a wide variety of calibration schemes can be analyzed. Example applications demonstrate the utility of using measurement uncertainty as a figure of merit. An experiment was conducted to validate some model predictions. Comparisons of model calculations with measurements using different calibration algorithms demonstrate the viability of the technique.

ACKNOWLEDGEMENT

There are many people that have helped me throughout the many years of study leading to the culmination of this work, certainly, more than I can acknowledge by name on this one page. I wish to acknowledge and thank each of them for all they've done to help me in my achievements. There are a few I would like to give special acknowledgement. First I want to acknowledge my family and friends. I wish to thank: my wife Sara for the love and care she gives me and our daughters, Zoe and Kelsey, who bring euphoric joy and frantic frustration to my life in all the ways that only toddler-age offspring can; my mother and father and grandparents whose love and care has let me live a prosperous life filled with happiness and wonder; my brother and sisters who have challenged me to see the world in new ways; and my network of friends, who are my extended family, through their love and camaraderie I get to live a dozen lives vicariously.

Nearly all of my post-graduate education has been supported by the National Aeronautics and Space Administration for which I am extremely grateful. I have always received unyielding support from my supervisors to pursue my educational endeavors, which is a credit to the agency that values and fosters a highly educated work force. And I must acknowledge and thank all my colleagues who have helped me along the way. I am blessed to have the opportunity to work with so many exceptionally talented people. I wish to thank my mentors, colleagues and friends, Dr. James Wang and Dr. Gerald Heymsfield, who have supported me through my professional development and challenged me to be a better engineer and a decent scientist. And I would also like to thank Dr. Edgeworth Westwater, Dr. Jeffrey Piepmeier, Dr. David Le Vine, and Dr. Robert Meneghini, Dr. Rafael Rincon, Dr. Steven Bidwell, and Mr. Mathew McLinden for their suggestions and insight that have improved the work presented, and Dr. Zhaonan Zhang who helped implement the MIR 2002 Calibration Experiment.

Finally, I would like to thank the faculty and staff at The George Washington University for all that I have learned while at the University. I would especially like to thank Professor Roger Lang whose contributions to this work through his keen attention to detail and mastery of applied mathematics and stochastic processes are unmistakable.

DEDICATION

This work is dedicated to my family and friends
who give me the strength and courage to pursue the hero's adventure.

TABLE OF CONTENTS

ABSTRACT.....	ii
ACKNOWLEDGEMENT.....	iii
DEDICATION.....	iv
TABLE OF CONTENTS.....	v
LIST OF FIGURES.....	vii
CHAPTER 1: INTRODUCTION.....	1
1.1 Motivation for Improved Microwave Radiometer Measurements.....	1
1.2 Examples of Radiometers.....	3
1.2.1 Millimeter-wave Imaging Radiometer.....	3
1.2.2 Department of Energy Microwave Radiometer.....	5
1.2.3 Compact Scanning Submillimeter-wave Imaging Radiometer.....	7
1.3 Research Objectives and Thesis Outline.....	9
CHAPTER 2: PREVIOUS WORK.....	12
2.1 Background.....	12
2.2 Review of Literature.....	13
2.3 Radiometric Resolution Defined.....	15
2.4 Summary.....	19
CHAPTER 3: RADIOMETER DESIGN AND MEASUREMENT UNCERTAINTY.....	20
3.1 Introduction.....	20
3.2 Radiometer Calibration Architectures.....	20
3.3 Calculation of Measurement Uncertainty.....	23
3.3.1 Model Decomposition and Measurement Estimator.....	23
3.3.2 Estimator of the Measurand and Measurement Uncertainty.....	27
3.4 Least Squares Regression.....	28
3.5 Discussion.....	33
CHAPTER 4: APPLICATION OF THE THEORY.....	35
4.1 Introduction.....	35
4.2 Cross-Track Imaging Radiometer.....	35
4.3 Calibration Using More Than Two References.....	44

4.4 Reference Averaging.....	46
4.5 Weighted Regression of Calibration Data.....	50
4.6 Two-point Versus Three-Point Calibration: A Case Study.....	52
4.7 Noise Source Injection and Tier 3 Calibration.....	54
4.7.1 Internal Calibration.....	55
4.7.2 External Calibration.....	62
4.8 Summary.....	67
CHAPTER 5: COMPARISONS WITH MEASUREMENTS	68
5.1 Introduction.....	68
5.2 The MIR 2002 Calibration Experiment.....	68
5.3 Three Calibration Algorithms.....	73
5.4 Summary.....	77
CHAPTER 6: CONCLUSION.....	78
REFERENCES.....	81
APPENDIX A: RADIOMETRIC RESOLUTION.....	86
A.1 Derivation of Resolution for a Radiometer Receiver With Gain Fluctuations.....	86
A.2 Comparison with Other Developments.....	91
APPENDIX B: REGRESSION OF CALIBRATION DATA.....	95
B.1 Regression of Data for estimating m and b	95
B.2 Unbiased Estimators.....	96
B.3 Uncertainty in \hat{T}_A	97
B.4 Weighted Least Squares Regression.....	99
APPENDIX C: CODE TO CALCULATE SYMBOLIC SOLUTIONS.....	102

LIST OF FIGURES

Figure 1: Millimeter-wave Imaging Radiometer.....	4
Figure 2: Department of Energy Microwave Radiometer	6
Figure 3: Compact Scanning Submillimeter-wave Imaging Radiometer	8
Figure 4: Basic radiometer model and principle of measurement resolution.....	13
Figure 5: Block diagram of a direct detection radiometer making a total-power mode measurement.....	17
Figure 6: Generic model for radiometer calibration architecture illustrating three tiers of calibration.....	21
Figure 7: Decomposition of a general radiometer model.....	25
Figure 8: Graphical illustration of a calibration data set of n measurements made at N different temperatures with $n > N$	30
Figure 9: Measurement uncertainty versus measurand brightness temperature for two pairs of calibration target temperatures.....	38
Figure 10: Measurement uncertainty as a function of time spent at each calibration reference and time spent observing the measurand for one pair of calibration target temperatures.....	39
Figure 11: A composite of curves illustrating the relationship between measurement uncertainty, calibration reference integration time, and hot reference load temperature.....	41
Figure 12: Measurement uncertainty as a function of time spent at each calibration reference illustrating the effect of latency.....	42
Figure 13: Measurement uncertainty as a function of calibration reference integration times for different receiver noise temperatures.....	43
Figure 14: Measurement uncertainty as a function of measurand temperature for different numbers of reference temperatures used in the calibration.....	45
Figure 15: Optimization of switching sequence for a single-reference switched radiometer.....	47
Figure 16: Optimization of switching sequence for a three-reference switched radiometer.....	49

Figure 17: A comparison of measurement uncertainty as a function of measurand brightness temperature when uniform weighting and optimal weighting of calibration data are used.....	51
Figure 18: Comparison of a two-point and three-point calibration architecture.....	53
Figure 19: Diagram of a radiometer system which utilizes three tiers to achieve calibration.....	56
Figure 20: Measurement uncertainty as a function of averaging window width and duty cycle.....	61
Figure 21: Measurement uncertainty for a two-point external calibration for the calibration algorithm described in 4.2.2.....	64
Figure 22: Plot of the measurement uncertainty comparing two calibration scenarios.....	66
Figure 23: Photograph of MIR during CalEx02.....	70
Figure 24: Time series of MIR data collected during CalEx02.....	72
Figure 25: Calibrated brightness temperatures calculated using two different algorithms...	74
Figure 26: Comparisons of measured standard deviation and modeled uncertainty of the T295 and T80 data sets using three different calibration algorithms.....	76
Figure A1: Block diagram of a direct detection radiometer receiver.....	86

CHAPTER 1

INTRODUCTION

Water, unlike religion and ideology, has the power to move millions of people. Since the very birth of human civilization, people have moved to settle close to water. People move when there is too little of it; people move when there is too much of it. People move on it. People write and sing and dance and dream about it. People fight over it. And everybody, everywhere and everyday, needs it. We need water for drinking, for cooking, for washing, for food, for industry, for energy, for transport, for rituals, for fun, for life. And it is not only we humans who need it; all life is dependent upon water for its very survival.

Mikhail Gorbachev, 2000

1.1 Motivation for Improved Microwave Radiometer Measurements

The importance of water for human existence is an underlying driver for needed improvement in the techniques for analyzing radiometer systems. Water is essential to sustaining the diversity of life on earth. The importance of water in moderating the world climate is well recognized but the underlying processes are not as well understood. Much effort is being applied to improving our understanding of the water cycle and its influence on global climate. Proper measurement of the water cycle, water distribution, transportation, phase and transition is key to understanding our complex climate. Hydrological data are needed as input to global climate models. Remote sensing measurements, especially those made using microwave radiometry, are key to providing the needed data.

Absorption and emission lines due to the molecular structure of water exist in the microwave region of the electromagnetic spectrum. These resonant frequencies make microwave measurements particularly useful for the detection of water. Furthermore, the relative size of liquid water droplets and ice particles such as those found in clouds are comparable in size to microwave, millimeter, and sub-millimeter wavelengths; thus these wavelengths are particularly sensitive to the presence of water particles. Because of this response of the microwave spectrum to the presence of water, microwave radiometry is well suited to making measurements pertinent to the understanding of the water cycle. Hence, microwave radiometry is playing an increasingly important role in monitoring the global climate. Although microwave remote sensing is a well

established engineering discipline, further improvements in measurement techniques are necessary to provide the needed data for climate modeling.

Radiometer calibration is becoming more important as data are being used to extract greater geophysical information from radiometric measurements. As new applications for microwave and millimeter-wave radiometer data are being developed, improved radiometric resolution and correspondingly improved accuracy are needed. (Accuracy is a qualitative concept describing the closeness of a measurement to the true value.) Finer resolution permits enhanced discrimination of changes in physical parameters from background noise. Accuracy is important for comparing temporal and spatial measurements made from one or many sensors and for using measurements to retrieve parameters by inversion of physical models. For example, the accurate measurement of precipitable water vapor (PWV) during very dry conditions which are predominant in high latitude regions are needed to better quantify the regional radiation energy budget. Millimeter-wave radiometry shows substantial promise for making improved PWV measurements [*Racette et al.*, 2005]. The accuracy with which PWV can be measured is limited by the quality of the radiometric measurements and accuracy of the absorption models. Other examples of parameters requiring improved resolution and accuracy include the retrieval of soil moisture content, sea surface salinity, liquid and ice water path, and vector wind measurements.

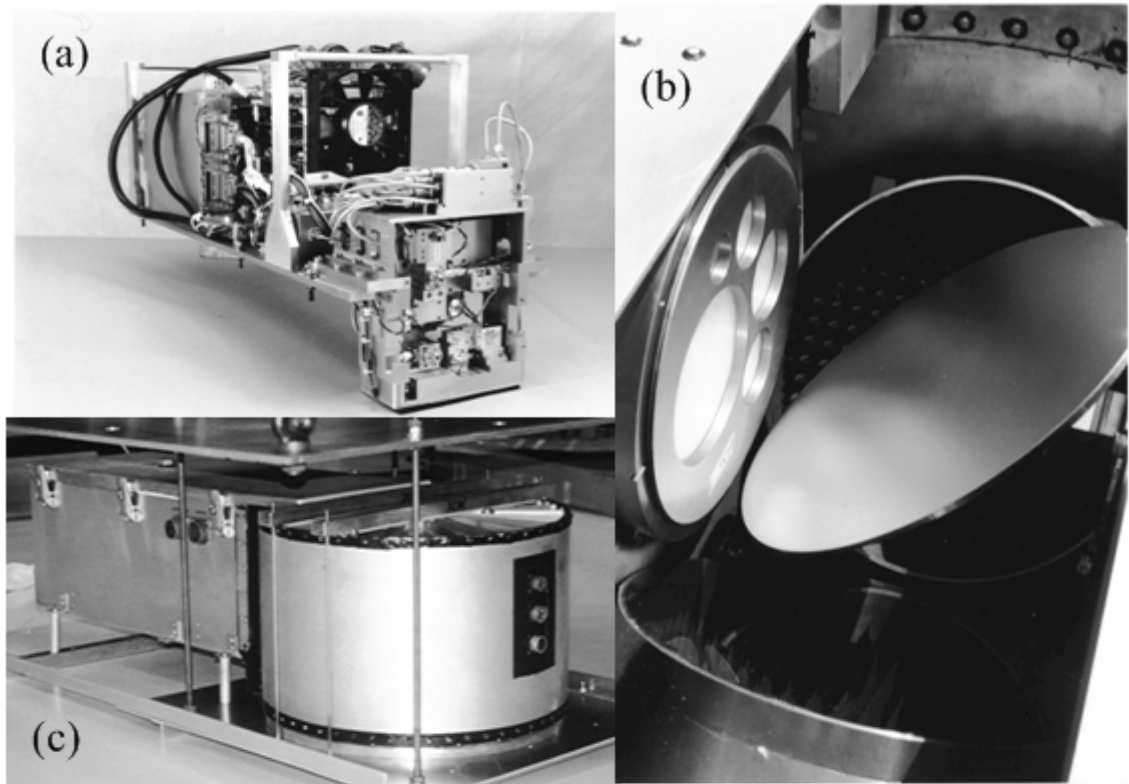
The advent of the Dicke radiometer in the 1940's spawned radio astronomy and microwave radiometry [*Dicke*, 1946; *Buderi*, 1996]. Since then many improvements in radiometric measurement techniques have been developed. Many papers are written on radiometer designs and techniques for analyzing radiometer performance. In recent years the number of operating radiometer systems and variations in radiometer designs have increased. Advances in RF technology, system control, and numerical processing have greatly expanded the envelop of radiometer capabilities. Today there exists a great number of radiometer designs and nearly as many different implementations of calibration algorithms. Wide variation in calibration designs combined with the need for improved measurements are justification for more general and comprehensive analysis tools for predicting radiometer performance than currently exists.

1.2 Examples of Radiometers

Figures 1 – 3 show examples of radiometers that have been built at the NASA Goddard Space Flight Center. Each radiometer is unique in its design and approach to calibration. The lack of analysis tools for analyzing radiometer designs and for performing system parameter trade studies presented special challenge in developing and optimizing the calibration architecture and algorithms for these radiometers.

1.2.1 Millimeter-wave Imaging Radiometer

Figure 1 shows photographs of the Millimeter-wave Imaging Radiometer (MIR). The MIR is a nine-channel cross-track scanning radiometer with frequencies at $89, 150, 183.31 \pm 1, 183.31 \pm 3, 183.31 \pm 7, 220$, and 340 GHz [Racette *et al.*, 1996]. The instrument is designed to fly aboard the NASA ER-2 high-altitude aircraft but has also been used for ground-based atmospheric measurements as well as laboratory studies [Racette and Wang, 1998; Racette *et al.*, 2005]. The three 183 GHz channels are centered about the 183 GHz water vapor absorption lines. The 89, 150, 220 and 340 GHz channels are located in atmospheric windows. The MIR design is based upon total-power detection principles. The 89 GHz and 150 GHz receivers use balanced mixers; the other channels use subharmonic mixers. The output of each mixer is amplified by a $\sim 60\text{ dB}$ gain IF amplifier. The amplified signal is filtered and then detected using a square-law tunnel diode detector. Each of the five fundamental frequencies has a lens-feedhorn antenna system with half-power beamwidths of approximately 3.5° . Figure 1a is a photograph of the electronics assembly. A gold plated mirror attached to a stepper motor is used to scan the antenna patterns 100° across the scene (see Fig. 1b). Figure 1c shows the radiometer housing. The receivers detect linear polarization, though the polarization angle rotates throughout the scan. Through the lens calibration is made during each scan cycle by sequentially looking at a hot and then cold calibration blackbody references. Figure 1d illustrates the across-track scan sequence. The mirror is scanned across the scene in approximately 2.2 s and each calibration reference is viewed for 150 ms. Latency in the scan cycle occurs as the mirror moves between the calibration references and the scene. The total scan cycle time is $\sim 3.0\text{ s}$.



(d)

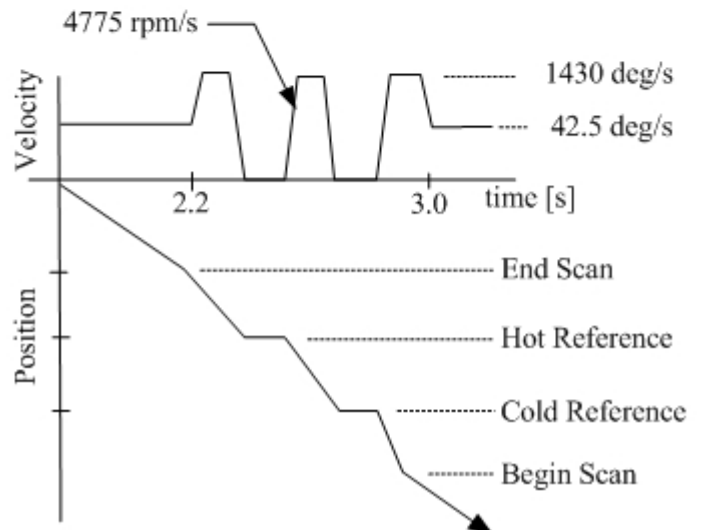
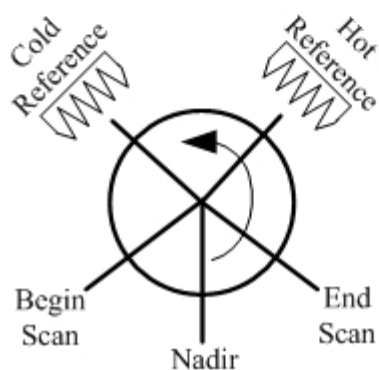


Figure 1: Millimeter-wave Imaging Radiometer. (a) Receiver electronics assembly, (b) antennae apertures, scanning mirror, and two calibration references, (c) radiometer housing. (d) Illustration of the timing for the MIR across-track scan profile. Left image shows the relative location of the calibration targets and the scene scan. Right image shows the timing sequence of the mirrors motion. (Photo's (a) and (b) are courtesy of David M. Jackson.)

The calibration references are 18-cm in diameter and consist of an array of quadrilateral pyramids with an aspect ratio of 4:1. (Originally, the MIR used calibration references with an aspect ratio of 3:1.) The references have an aluminum core and are coated with an ~0.1 cm epoxy-based microwave absorbing material. The hot reference is heated to ~330 K by thermofoil heaters. The cold reference is passively regulated by the ambient conditions. During flight the cold reference reaches a temperature near 250 K thus yielding a temperature difference between the two references of about 80 K. When operated on the ground the cold reference is usually much warmer; the temperature difference of the two references is around 20 – 30 K. Thus better calibration is obtained during in-flight. In his dissertation, *D.M. Jackson* [1999] investigated the influence of reference emissivity and temperature gradients on the calibration of MIR. In this dissertation, the MIR is used as an example to study parameter optimization in designing the calibration scheme. Analysis of the MIR calibration algorithm is performed in Chapter 4. MIR data from an experiment to study its calibration are presented in Chapter 6.

1.2.2 Department of Energy Microwave Radiometer

Figures 2a and 2b show photographs of the Department of Energy Microwave Radiometer (DoER). The DoER is a seven channel microwave radiometer designed to measure precipitable water vapor and cloud liquid water [*Racette et al.*, 1998]. The seven channels are centered about three frequencies, 22.2 GHz, 36.5 GHz, and 89.0 GHz. In Fig. 2c the channel locations are shown over plotted onto absorption spectra of atmospheric constituents: water vapor, cloud liquid water, and oxygen. The 36.5 GHz and 89 GHz channels use double-sideband mixers with intermediate frequencies of 100 – 500 MHz. A low-noise radio-frequency amplifier and single-sideband mixer provide independent sampling of both sides of the 22.2 GHz absorption line. A 5-channel multiplexer is used to separate the 3500 MHz bandwidth mixer output into five equally spaced 500 MHz passbands as shown in the inset figure of Fig 2c. Calibration is obtained by switching between four calibration references. Each receiver is switched between the scene and calibration references using three-junction (five-port) ferrite latching circulators. Two of the references are waveguide terminations encased in thermally controlled copper blocks. One block is heated to ~340 K and the other block is cooled using a Sterling cycle cooler. A noise source connected through a waveguide attenuator provide

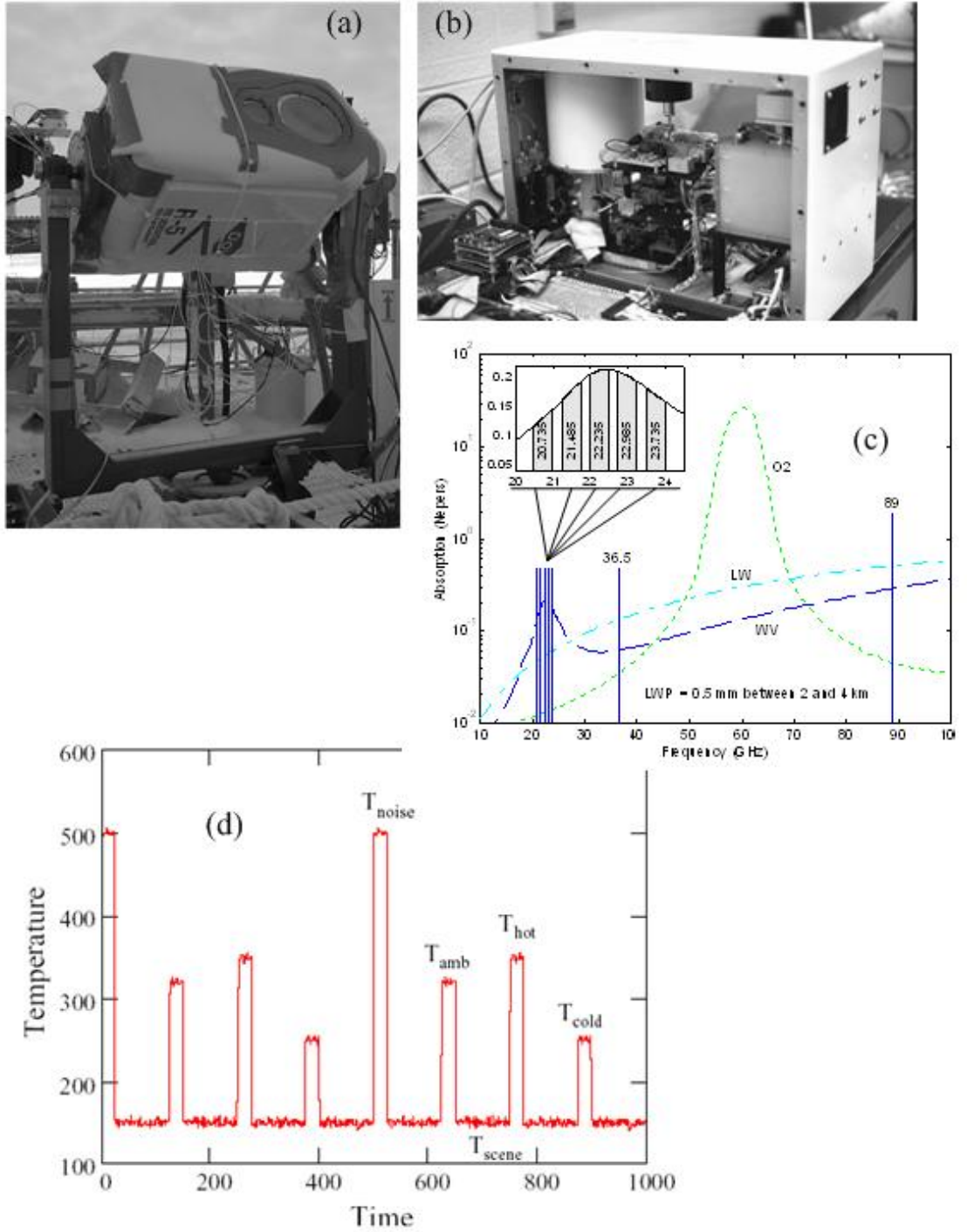


Figure 2: Department of Energy Microwave Radiometer. (a) Photograph of the DoER during a deployment in Barrow, Alaska making measurements to study techniques for retrieving low amounts of precipitable water vapor. (b) Photograph of the interior of the DoER. (c) DoER channel locations are plotted on surface to top-of-atmosphere absorption spectra of water vapor (WV), liquid water (LW), and oxygen (O₂). The passbands of the channels near the 22 GHz absorption line are shown in the inset figure. (d) Time series of the DoER sampled output. Observations of the four internal calibration references are interleaved with observations of the scene.

the other two references; with the noise source off, the attenuator appears like a waveguide termination at ambient temperature; with the noise source energized, the attenuator has an equivalent noise temperature in excess of 500 K. Figure 2d shows a time series of the radiometer's output. Observation of the noise source, ambient reference, hot reference and cold reference are interleaved with observations of the scene. Optimization of the reference temperatures and switching sequence for this multiple-calibration-reference radiometer posed particular challenge without a technique for assessing the performance of the calibration design.

1.2.3 Compact Scanning Submillimeter-wave Imaging Radiometer

Figures 3a and 3b show photographs of the Compact Scanning Submillimeter-wave Imaging Radiometer (CoSSIR). The CoSSIR, designed for installation on the ER-2, is an instrument developed to study the application of submillimeter-wave radiometry for remote sensing of cirrus clouds and humidity sounding [Racette *et al.*, 2004]. It has six receivers and a total of fifteen channels; nine of the channels are horizontally polarized at frequencies: 183.3 ± 1 , 183.3 ± 3 , 183.3 ± 6.6 , 220, 380 ± 0.8 , 380 ± 1.8 , 380 ± 3.3 , 380 ± 6.2 , and 640 GHz; the remaining six are dual-polarized at three frequencies of 487 ± 0.7 , 487 ± 1.2 , and 487 ± 3.3 GHz. The beam width of each frequency channel is $\sim 4^\circ$. The CoSSIR's frequency range is well suited for retrievals of ice water path and ice particle size. The dual polarization capability at 487 GHz has the potential of inferring the shape of ice particles. Furthermore, the multi-channel measurements around the water vapor absorption lines of 183.3 and 380 GHz provide information for retrievals of water vapor profiles. The instrument flew for the first time during Cirrus Regional Study of Tropical Anvils and Cirrus Layers - Florida Area Cirrus Experiment (CRYSTAL-FACE), and demonstrated the capability of these high frequencies to retrieve IWP and particle size, *Evans et al.* [2005].

Figure 3a shows the compactness of the receivers and electronics inside the scan head when the CoSSIR was first assembled in the laboratory. The scan head cylinder (shown in Fig. 3b) is only ~ 28 cm long and ~ 21 cm in diameter and contains all the receivers, signal conditioning electronics, data system and power conditioning circuitry. The compact design lends itself to other integration configurations such as on unmanned aerial vehicles. The scan

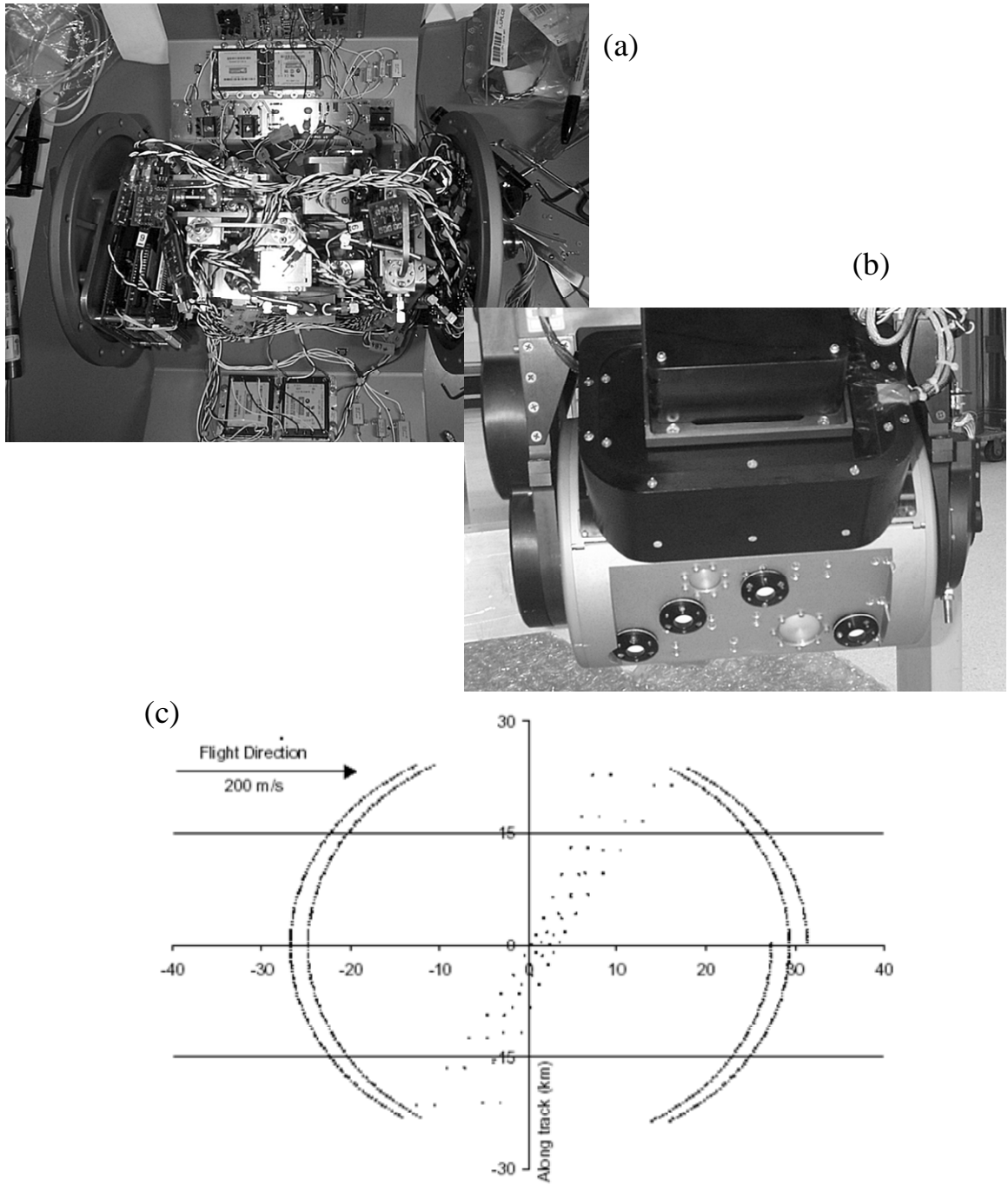


Figure 3: Department of Energy Radiometer. (a) Photograph of the interior of the CoSSIR scanhead. The scanhead contains 6 heterodyne receivers, power conditioning circuitry, and a data digitization system. (b) Photograph of the scan head mounted to the dual-axes gimbals. The six apertures can be seen on the faceplate of the scanhead. The black structure is one of two close-coupled calibration references. (c) Geometry of one of CoSSIR's programmed scan sequences. Two complete scan cycles are shown. The points represent the center of the beam positions projected onto the Earth's surface. Calibration and an across track scan are performed twice per scan cycle.

head is rotated by a two-axes gimbaled mechanism capable of generating a wide variety of scan profiles. The scan mechanism was developed for the Conical Scanning Microwave Imaging Radiometer (CoSMIR) [Piepmeier *et al.*, 2001]. In the conical scanning mode (see Fig. 3c) the azimuth axis rotates the antenna patterns at 6 rpm to generate the conical scan while at the same time the elevation axis maintains the antenna pointing at the prescribed angle of incidence. Twice during each rotation of the azimuth axis, calibration is performed by viewing two close-coupled calibration references followed by a cross track scan. The elevation axis is used to rotate the antennas to point at the calibration references and then to sweep the antenna patterns through nadir back to the prescribed incidence angle of the conical scan. The two blackbody references have in-flight temperatures of ~250 K and ~330 K. During CRYSTAL-FACE, the instrument was operated in an across-track mode. The analysis techniques presented in this paper have been a valuable aide for selecting timing parameters in the scan patterns for the CoSMIR and CoSSIR.

1.3 Research Objective and Dissertation Outline

The primary objective of this research is to develop a generalized technique by which system calibration architectures and design parameters can be studied to optimize instrument performance for a set of given requirements and constraints. A generalized technique for analyzing radiometer designs should provide the means to evaluate the following:

- Tradeoff between time observing the measurand (e.g., the quantity being measured) and time spent calibrating,
- Effects of interpolating and extrapolating the calibration,
- Influence of calibration reference temperature uncertainty,
- Influence of calibration frequency.

A metric that satisfies these criteria is the uncertainty of measurement (or measurement uncertainty). Measurement uncertainty is a parameter that quantifies the dispersion of measured values about the true value of the measurand that could reasonably be expected [ISO, 1993]. In this paper, measurement uncertainty is defined as the mean square difference between the estimated value and the mean value of the measurand. Applied to radiometry, measurement uncertainty includes the uncertainty due to the finite radiometric resolution inherent in the measurand observation and uncertainties associated with the application of calibration data.

Measurement uncertainty as a figure of merit can be applied to assess the performance of all radiometers.

The American National Standards Institute identifies two approaches for evaluating components of measurement uncertainty [ANSI, 1997 chapter 3]. Type A evaluation is based upon statistical analysis of a series of observations. Type B evaluation is based on means other than analysis of observations and usually involves the assumption of a probability distribution function for those factors affecting measurement uncertainty. There is no difference in the nature of uncertainties derived from type-A and type-B analyses; the distinction is made only to reflect the means by which the uncertainty is evaluated. This dissertation only addresses measurement uncertainty associated with radiometer designs, and thus, the discussion is limited to type-B analyses. The analysis of measurement uncertainty of actual radiometers is a topic of contemporary importance and there exists ongoing collaboration between National Aeronautics and Space Administration and the National Institute of Standards and Technology to develop standardized techniques for evaluating combined (type-A and type-B) measurement uncertainty in microwave radiometers.

In Chapter 2 a discussion of previous works relevant to radiometer system analysis is presented. These works use radiometric resolution as a figure of merit for qualifying radiometer performance. Because of its importance to the theme of this paper, the definition of radiometric resolution is examined and the assumptions underlying the classic definition for resolution are reviewed. The limitations in using radiometric resolution to evaluate calibration designs are discussed. In Chapter 3 a general model for a radiometer design is introduced that identifies three tiers within which calibration architecture can be described. A technique is presented for evaluating the measurement uncertainty by decomposing the radiometer design into a set of subsystems. Radiometric resolution is shown to be one component of the measurement uncertainty; other components arise from the estimation of the receiver response. A framework is introduced whereby the measurement uncertainty can be evaluated for a wide variety of calibration architectures using the convenient mathematics of least squares regression. In Chapter 4 the utility of measurement uncertainty as a figure of merit is demonstrated by evaluating measurement uncertainty for a variety of calibration architectures and algorithms; it is shown how measurement uncertainty can be used to optimize parameters in the calibration design of a radiometer. The development provides the means to evaluate and optimize the time

spent observing the measurand, the influence of calibration reference temperature and the effects of interpolating and extrapolating calibration data.

Measurement uncertainty as a function of calibration frequency depends on the non-stationary stochastic properties of the radiometer pre-detection circuit and receiver electronics. In Chapters 3 and 4 the utility of measurement uncertainty as a figure of merit is illustrated by assuming that the fluctuations in the radiometer response are wide-sense stationary, i.e., stationary in the first and second moments. Analysis of nonstationary stochastic processes adds a layer of complexity. With the exception of a brief discussion in Chapters 2 and 3, analyses including non-stationary fluctuations are not treated in this dissertation.

In Chapter 5 an experiment is described that was conducted with the MIR to study comparisons of model calculations with measurements. The comparisons demonstrate the efficacy of the analysis technique presented. Chapter 6 concludes the dissertation with a summary of findings.

CHAPTER 2

PREVIOUS WORK

2.1 Background

A radiometer is an instrument that measures radiant power. An imaging radiometer measures the angular distribution of power; a spectroradiometer measures the spectral distribution of power; and a polarimeter measures the polarization of the power. Correlation, bolometric, heterodyne, and direct detection are methods for detecting the radiant power. For a discussion on the principles of radiometry see *Ulaby et al.* [1981, chapter 4], *Kraus* [1966, chapter 7], and *Rohlf and Wilson* [1996, chapter 4]. Regardless of the method of detection, at the core of a radiometer is a calibrated receiver [Skou, 1989, chapter 1].

A radiometer receiver is shown in Fig. 4a. Noise power with equivalent brightness temperature T_{sys} enters the receiver and is converted to the output signal v . (It is common in microwave radiometry to assume the Raleigh-Jeans limit of the Planck function, whereby temperature is proportional to the band-limited detected power. Herein, T_{sys} is assumed proportional to the noise power at the receiver input.) The system noise temperature at the receiver input is the sum of the brightness temperature corresponding to the radiant power at the input of the radiometer antenna, T_A , and the receiver noise temperature, T_{rec} , i.e., $T_{sys} = T_{rec} + T_A$. Figure 4b shows a time series of the output v for a small change in the system noise temperature. The radiometer response defines the relationship between v and T_A ; for radiometers utilizing square-law detection, the response is linear. The radiometer response fluctuates due to inherent instabilities in the radiometer electronics. *Calibration is the process by which the radiometer response is estimated.* Through calibration an estimate of T_A can be derived from the output signal v . The scheme employed to achieve calibration is central to the design of any radiometer; there exists many techniques for achieving calibration. Numerous papers have been written over the past fifty years that have led to improvements in radiometer system performance and analysis. Extensive analysis has been performed on the Dicke radiometer and total power configurations. Contemporary radiometer designs incorporate features of Dicke-type and total-power-mode radiometers as well as external measurements to achieve calibration.

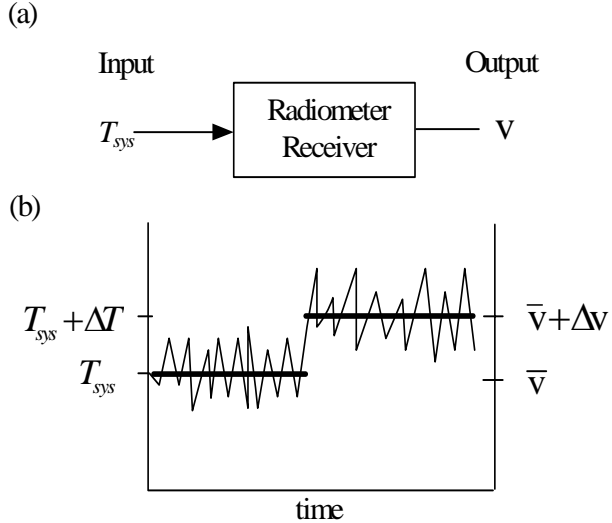


Figure 4: Basic radiometer model and principle of measurement resolution. (a) Illustration of a basic radiometer model with input brightness temperature T_{sys} and output voltage v . (b) Graph illustrating the principle of measurement resolution.

With the diversity of radiometer designs there exists a lack of consistency in the terminology used to describe calibration techniques. For this reason several terms are defined for clarification. In some radiometers the output signal of the system is the difference between signals originating from the measurand and a standard reference. This detection scheme is referred to as *reference differencing*. A *Dicke radiometer* utilizes reference differencing with a 50% duty cycle. In a *switched-reference* detection scheme, observations of the measurand are interleaved with observations of one or more references. *Reference averaging* is a technique in which multiple observations of a reference are used to improve the resolution of the reference measurement. In *total-power mode*, observations of a measurand are made sequentially without interleaved observations of a reference(s).

2.2 Review of Literature

Reference differencing radiometers, especially Dicke-type, have received extensive analysis in the literature [Goldstein, 1955; Tiuri, 1964; Wait, 1967; Bremer, 1979; Thomsen, 1984]. Wait [1967] derives a method using Fourier transforms for analyzing the resolution of reference differencing radiometers. Wait identifies a series of papers that analyze the performance of the reference differencing radiometer but yield differing results for the radiometric resolution. Wait resolves these differences by identifying the divergent assumptions,

standardizing the notation, and pointing out errors in published results. A comparison of results is given in a table that contains the radiometric resolution for a number of modulation and correlation waveforms. *Thomsen* [1984] analyzes a reference differencing radiometer with asymmetric switching including the influence of gain fluctuations; however in the limit of symmetric switching (50% duty cycle) with no gain fluctuations, his results differ by $2^{1/2}$ from those of *Kraus* [1966, chapter 7], *Ulaby et al.* [1981, chapter 4], *Wait* [1967], *Bremer* [1979] and others.

Hach [1968] presents a measurement technique that utilizes two internal temperature references for calibrating the radiometer. The receiver is periodically switched between the measurand and the two temperature references. The radiometer is calibrated using measurements from the two temperature references. The advantage of this technique over the reference differencing radiometer is that the receiver response, i.e. both gain and offset, is measured every cycle. Hach's design which divides the cycle period evenly between the measurand and the two calibration references suffers a loss of resolution compared to a Dicke-type radiometer due to a greater percentage of the duty cycle being spent observing calibration references.

The resolution of a reference-differencing radiometer may be improved by a technique presented by *Bremer* [1979]. Bremer demonstrates that significant improvement in performance can be achieved when the reference measurements are averaged over many cycles. Performance is optimized by increasing the portion of the duty cycle that is spent viewing the measurand and increasing the number of reference measurements averaged to reduce the statistical uncertainty in the estimation of the reference value. The improvement in resolution may approach that of the total power mode. Bremer applies his analysis to compare the output power spectrum of the reference averaging algorithm to that of the total-power mode. Reference averaging offers significant advantage over the traditional reference-differencing techniques. Improvements in digital processing has greatly simplified the implementation of reference averaging; reference averaging is commonly used in radiometers today.

Hersman and Poe [1981] analyze the performance of the total-power mode improving upon previous analysis by including the effects of receiver gain fluctuation and calibration algorithm. In their presentation, radiometric resolution is used as the figure of merit and is defined to be proportional to the integral of the product of the receiver post-detection transfer function and the power spectrum of the square-law detector output (in Appendix A see (A.17)

and adjacent discussion). The resulting model accounts for system noise temperature, non-uniform power spectral densities, and processing algorithm parameters such as the calibration period and integration times. *Peckham* [1989] extends their work by deriving a set of optimum weights that minimizes the variance of the difference between the weighted average of calibration and measurand samples. This approach fails to account for non-uniform noise components due to the receiver switching between sources. This shortcoming is avoided by assuming the measurand and calibration references have the same noise temperature. An upper limit on the resolution is obtained by setting the sources of emission equal to the hottest reference. In the limiting case with no gain fluctuations and uniform weighting of the reference measurements the results of *Hersman and Poe* [1981] agree with those presented by *Bremer* [1979].

The references sited above use radiometric resolution as basis for assessing radiometer system performance. By examining its definition, radiometric resolution has been found to have limited utility for evaluating the performance of radiometer designs. Alternatively, measurement uncertainty is a more appropriate figure of merit for evaluating and comparing radiometer designs when the calibration is considered. The difference between radiometric resolution and measurement uncertainty is more than semantic. Resolution is one component of the measurement uncertainty. Recognizing the distinction facilitates performance analysis for all types of radiometers. In the following section the definition of radiometric resolution is examined and limitations of applying resolution to radiometer analysis are discussed.

2.3 Radiometric Resolution Defined

Radiometric resolution is defined to be the minimum change in the input signal level that can be resolved at the output of the radiometer receiver. Figure 4b illustrates the relationship between the receiver input noise power and the output signal as a function of time. The radiometer output signal fluctuates because of the inherent stochastic properties of emission and receiver electronics. The mean output signal level, \bar{v} , is indicated on the right hand side of the figure and is given by

$$\bar{v}(T_{sys}) = E\{v(t)\} \Big|_{T_{sys}} \quad (2.1)$$

where the ensemble average includes all possible outputs, $v(t)$, that correspond to the input level T_{sys} . A change of signal (ΔT) is considered resolvable at the radiometer output if the ratio of the

power in the signal change, ΔS_0 , to signal noise power at the output, N_0 , is equal to or greater than 1 [Dicke, 1946; Kelly *et al.*, 1963; Wait, 1967], i.e.,

$$\frac{\Delta S_0}{N_0} \geq 1 . \quad (2.2)$$

The signal noise power is proportional to the variance of the output signal evaluated at the receiver input noise temperature, T_{sys} ,

$$N_0 \propto \sigma_v^2 \Big|_{T_{sys}} = E\{v(t)v(t)\} \Big|_{T_{sys}} - E^2\{v(t)\} \Big|_{T_{sys}} \quad (2.3)$$

The power in the change of signal is found by truncating the Taylor series expansion of $\bar{v}(T_{sys})$ at the second term for small ΔT , i.e.,

$$\bar{v}(T_{sys} + \Delta T) = \bar{v}(T_{sys}) + \Delta T \cdot \frac{\partial \bar{v}}{\partial T} \Big|_{T_{sys}} . \quad (2.4)$$

For a receiver with a square law detector, the relationship between \bar{v} and T_{sys} is linear; thus, all the change in signal power is contained in the second term of the expansion. The power in the change of the output signal is

$$\Delta S_0 \propto (\bar{v}(T_{sys}) - \bar{v}(T_{sys} + \Delta T))^2 = \left(\Delta T \cdot \frac{\partial \bar{v}}{\partial T} \Big|_{T_{sys}} \right)^2 . \quad (2.5)$$

Substituting (2.3) and (2.5) into (2.2), noting that the proportionality constant is the same, and solving for $(\Delta T)^2$ yields the classic formula

$$(\Delta T)^2 = \frac{\sigma_v^2}{\left(\frac{\partial \bar{v}}{\partial T} \right)^2} \Big|_{T_{sys}} . \quad (2.6)$$

The minimum detectable change in signal at the input is equal to the noise power at the output times the reciprocal of the squared response of the system evaluated at T_{sys} . Sometimes radiometric resolution is referred to as the noise equivalent temperature difference, i.e. “NEΔT”, or sensitivity. Peculiar to microwave engineering, *sensitivity* is synonymous to *resolution*. However in other engineering disciplines, *sensitivity* is more commonly used to describe the change of a system output per change in input stimulus (or its reciprocal) [ISO, 1993; IEEE, 1996, Van Putten, 1996]. The square root of the denominator in (2.6) is then the radiometer

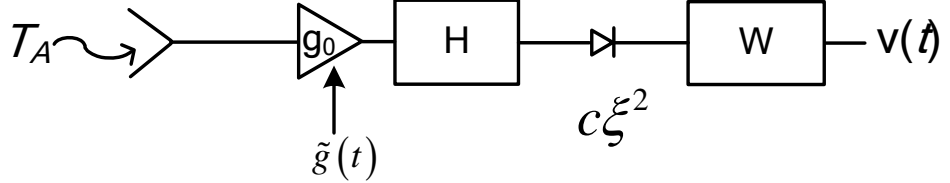


Figure 5: Block diagram of a direct detection radiometer making a total-power mode measurement. The radiometer is comprised of an antenna, amplifier, pre-detection filter, square-law detector and post-detection filter.

sensitivity. To be more consistent with the engineering community at large, *resolution*, or more specifically *radiometric resolution*, is preferred over *sensitivity* to describe (2.6).

Figure 5 shows a model of a direct detection radiometer operating in total-power mode. Noise power T_A enters the radiometer through an antenna. The radiometer receiver is comprised of an amplifier (g_0), predetection filter (H), square law detector, and a post-detection filter (W). The system noise temperature at the receiver input is $T_{sys} = T_A + T_{rec}$. The radiometer output is the voltage $v(t)$. Evaluating (2.6) for this radiometer model leads to the classic definition of radiometric resolution [Dicke, 1946; Rohlfs and Wilson, 1996, chapter 4]

$$\Delta T \equiv \frac{T_{sys}}{\sqrt{B\tau}} \quad (2.7)$$

where B is the bandwidth of the predetection filter and τ is the post-detection integration time constant. These terms are defined by Tiuri [1964] and are given in Appendix A.1. Rohlfs and Wilson [1996, chapter 4] presents a derivation of (2.7) based upon stochastic signal theory. Le Vine [1990] presents a derivation of the resolution for a correlation receiver in an interferometer and shows how the result yields (2.7) in the limiting case of zero displacement in the antenna elements. In Appendix A.1, the radiometric resolution of a direct-detection radiometer receiver with gain fluctuations is evaluated. The amplifier gain, $g(t) = g_0 + \tilde{g}(t)$, is modeled as a wide-sense-stationary random process with mean g_0 . For a receiver with gain fluctuations, (2.6) leads to

$$\Delta T \cong T_{\text{sys}} \cdot \left(\frac{1}{B\tau} + \left(\frac{\Delta G}{G} \right)^2 \right)^{1/2} \quad (2.8)$$

where

$$\left(\frac{\Delta G}{G} \right)^2 = \left(\frac{2}{W(0) \cdot g_0} \right)^2 \int df S_{\tilde{g}}(f) |W(f)|^2 ,$$

and where $S_{\tilde{g}}(f)$ is the power spectrum of the fluctuating component of $g(t)$ and $W(f)$ is the frequency response of the post-detection filter.

Essential to the derivation of (2.8) is the assumption that $g(t)$ is wide sense stationary. Some authors, [Kunzi and Magun, 1977; Hersman and Poe, 1981; Thomsen, 1984; Peckham, 1989; Wollack, 1995], use

$$S_{\tilde{g}}(f) \propto 1/f^\gamma \quad (2.9)$$

to evaluate (2.8), even though such a spectrum violates the Weiner-Khinchin theorem for $\gamma \geq 1$ [Davis et al., 1996]. One might argue that over a certain interval the gain fluctuations may be considered stationary and, hence, the Fourier relationship between the autocorrelation function and power spectrum exists. In evaluating the influence of calibration frequency on measurement uncertainty, the interval of interest is on the same time scale that the fluctuations in the receiver become nonstationary. The assumption that the stochastic properties of the receiver are stationary may not be justified when studying the interaction between calibration frequency and receiver fluctuations. The temporal factors of the calibration algorithm in the presence of nonstationary receiver fluctuations are not treated in this dissertation.

The effect of switching between calibration references on radiometric resolution of periodically calibrated radiometers has been investigated [Bremer, 1979; Hersman and Poe, 1981]. Inevitably, calibration involves observations of references of different brightness temperatures. Evaluation of the output noise power when the input signal power changes when viewing different sources is non-trivial. Difficulty arises in computing the square-law detector output and its convolution with the post-detection transfer function of the radiometer. Furthermore, (2.6) is evaluated at the system noise temperature. When a radiometer observes sources with different noise temperatures to achieve calibration, T_{sys} necessarily changes. Thus, evaluating (2.6) in the context of a calibration algorithm is inconsistent with its definition. In the literature these complexities have been avoided by assuming the temperature of the measurand

and calibration references are equal thus limiting the usefulness of radiometric resolution as a figure of merit for the performance of a radiometer.

An alternative figure of merit is measurement uncertainty. Measurement uncertainty is an established metric by which to quantitatively qualify a measurement [ANSI, 1997, chapter 0]. In optical radiation metrology, measurement uncertainty is used to characterize sensor system calibration [Wyatt *et al.*, 1998]. In microwave radiometry, the National Institute of Standards and Technology uses measurement uncertainty to quantify the errors in calibrating noise source standards [Randa, 1998]. *Racette and Lang* [2000a; 2000b; 2001; 2002a; 2002b] have presented the use of measurement uncertainty as a figure of merit to qualify the performance of radiometer designs. More recently, *Piepmeier* [2004] uses measurement uncertainty to study calibration architectures for polarimeters that use hybrid coupler-based correlators. The research presented in this dissertation builds on these prior works by presenting a generalized technique for evaluating measurement uncertainty for radiometer designs.

2.4 Summary

In this chapter publications that address radiometer design and system performance were reviewed. These previous works have used radiometric resolution as the figure of merit on which to assess radiometer performance. As discussed, radiometric resolution has limited application when considering the calibration architecture and algorithm of a radiometer. An alternative approach is to consider the measurement uncertainty. Measurement uncertainty includes the resolution of the measurand observation as well as uncertainty associated with applying the calibration data. In the next chapter a general model is introduced that describes a wide variety of calibration architectures. A method is then presented to analyze the measurement uncertainty.

CHAPTER 3

RADIOMETER DESIGN AND MEASUREMENT UNCERTAINTY

3.1 Introduction

In this chapter measurement uncertainty is introduced as a figure of merit on which to base quantitative assessment of a radiometer's design including its calibration architecture and algorithm. First, a general model is introduced that describes a wide variety of radiometer architectures. A technique is then presented to calculate the measurement uncertainty. A framework based on least squares regression is described, whereby, a wide variety of calibration designs can be evaluated through simple calculations. The chapter concludes with a discussion about the technique presented.

3.2 Radiometer Calibration Architectures

The calibration architecture of most microwave radiometers can be divided into three tiers as illustrated in Fig. 6. Measurements from one or more of the three tiers are used to calibrate the radiometer response. A data processor controls the timing of the calibration reference observation sequence as well as records pertinent data for utilizing the references. In some systems data may be processed in real time to produce estimates of the antenna brightness temperature and others rely on post-processing of the data to calculate the estimates.

First tier calibration consists of calibration references that are switched (or injected) into the receiver path after the antenna. Calibration structures that fit into this first category include temperature controlled waveguide terminations switched into the receiver path using waveguide switches and active noise sources injected using directional couplers. The first tier is most often used to compensate for fluctuations in the active components of a receiver. Though one or more internal references can be used to track fluctuations in the receiver response, the internal references do not measure fluctuations that occur in circuitry beyond the plane of the reference measurement, e.g. antenna losses. Usually the equivalent antenna brightness temperatures of the references have to be determined through either second or third tier calibration. First tier calibration is utilized when second or third tier calibrations cannot be performed sufficiently rapid to track receiver fluctuations. Descriptions of radiometers that use first tier calibration can

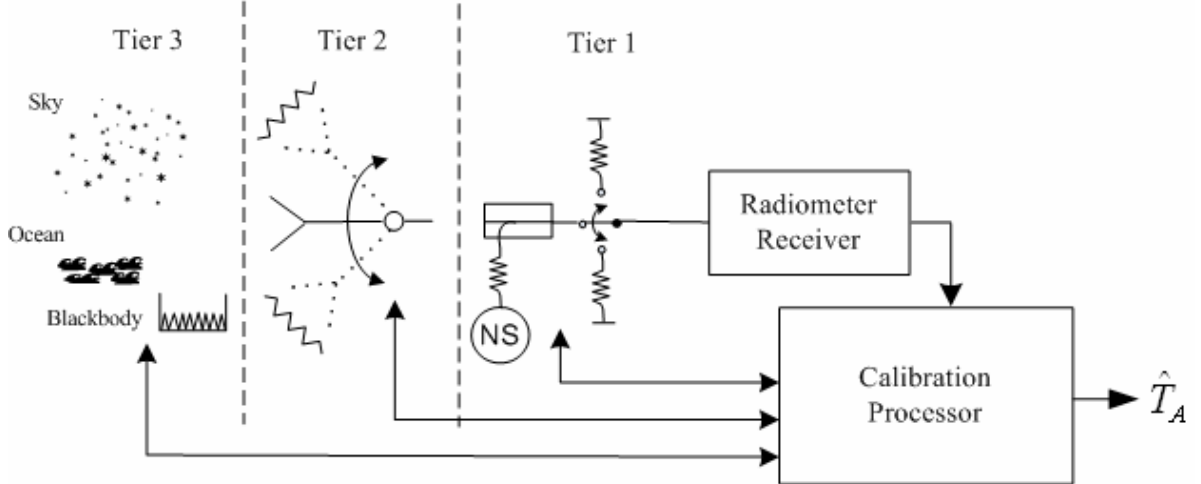


Figure 6: Generic model for radiometer calibration architecture illustrating three tiers of calibration. Tier 3 comprises calibration references external to the radiometer, e.g. cosmic background radiation, ocean surface. Calibration references that are included as part of the radiometer system and are observed through the antenna are in Tier 2. Calibration references internal to the radiometer receiver and not observed through the antenna are in Tier 1, e.g. noise source (NS) injection.

be found in [Hach, 1968; Conglong *et al.*, 1986; Ruf *et al.*, 1995; Tanner, 1998; Racette *et al.*, 1998].

The second tier comprises calibration structures that provide a means of calibrating the system response including the effects of the antenna and coupling components. Typically the antenna pattern is projected onto one or more isothermal blackbody radiators. In systems that utilize a second tier structure, characterizing system response is straightforward and can yield accurate calibration since the entire signal path including lossy antenna components is included in the calibration. Several factors limit the practicality of implementing second tier architectures. Blackbody radiators that can envelop the antenna aperture are large, massive, expensive, and prone to errors caused by thermal gradients and standing waves between the reference and antenna. Usually a mechanism is needed to switch the field of view of the antenna from the measurand to the calibration reference(s) thus complicating the design of the instrument. Such switching mechanisms are typically slow and contribute to the measurement uncertainty. The Millimeter-Wave Imaging Radiometer [Racette *et al.*, 1996], MARSS [McGrath and Hewison, 2001], and the Advanced Microwave Sounding Unit-B (AMSU-B) [Saunders *et al.*, 1995] are examples of radiometers that utilize second tier calibration. The Polarimetric Scanning Radiometer utilizes both first and second tier calibration structures in its calibration scheme

[*Corbella et al.*, 2002]. In some radiometer designs the distinction between tier 1 and tier 2 architectures is not clearly delineated. For example, in the Tropical Rain Measuring Mission Microwave Imager, a blackbody radiator and cold-space mirror are moved between the primary antenna reflector and the feedhorns [*Wentz et al.*, 2001].

Although second tier calibration provides a means of estimating the system response that includes the effects of antenna losses and coupling mechanisms, additional parameters may be necessary to correct for instrument specific effects such as cross coupling of the calibration references [*Racette et al.*, 1995]. Third tier calibration utilizes measurements external to the instrument. These measurements can then be used to estimate parameters used in the instrument calibration. External references can be blackbody radiators or environmental sources of emission with known properties. Examples of environmental references include: cosmic radiation, tip-curve calibration, and ocean surface. The third tier often provides the most accurate reference for calibration because the measurements encompass entire system effects and external references, e.g. cosmic radiation, can be as close to an absolute standard that exists. External calibration can also correct for instrument effects that are not measured in first or second tier calibrations. Nevertheless, third tier calibration usually comes with difficulties associated with making the measurement. External reference measurements usually cannot be performed with frequency adequate to track fluctuations in the receiver response. Because of the ability to accurately and precisely characterize entire system effects, third tier calibration is often used to tweak parameters in the system equation to improve calibration, e.g. antenna coupling losses, effective noise source temperature, etc... An example of the application of third tier architecture applied to calibrating a radiometer is given by *Ruf* [2000]. Ruf describes a technique whereby the properties of the ocean surface brightness temperature are used to correct for a drift in the isolation of a ferrite switch in the TOPEX/Microwave Radiometer.

The Microwave Water Vapor Radiometer (MWR) used by the Department of Energy's Atmospheric Radiation Measurement program is an example of a radiometer that operationally utilizes all three tiers to achieve calibration [*Liljegren*, 2000]. A noise source is injected into the receiver path using a directional coupler. A rotating mirror projects the antenna pattern at an internal blackbody and over a range of elevation angles across the sky. The relation between atmospheric opacity and elevation angle, i.e. tip-curve calibration [*Han and Westwater*, 2000], is used to track the effective noise source temperature and system losses.

It is usual to include parameters in the radiometer calibration to correct for non-idealities in the instrument, e.g. insertion loss, reflections, coupling. Many papers have been written on radiometer system models, parameters to include in the calibration, and techniques for estimating calibration parameters. A technique to correct for coupling between calibration references and the measurand is given by *Racette et al.* [1995]. A technique for transferring internal calibration measurements (tier 1) to an equivalent antenna brightness temperature is given by *Corbella et al.* [2002]. Insertion loss and mismatch effects on radiometric measurements are discussed in [Hach, 1968; Ulaby et al., 1981; Ruf et al., 1995; Stelzried, 1968; Miller et al., 1967]. Parameters used for calibration are specific to the system design; values of the parameters and their corresponding uncertainties are specific to the hardware used in the design implementation.

In the following section the uncertainty in the calibrated estimate of the measurand, i.e. measurement uncertainty, is derived. The measurement uncertainty is a function of the individual uncertainties of all measurements and system parameters that go into calculating an estimate of the measurand. The technique can be applied to systems utilizing calibration measurements from one or a combination of tier 1, 2 or 3 architectures.

3.3 Calculation Of Measurement Uncertainty

In this section a technique is presented for evaluating the measurement uncertainty of a radiometer design. First, the design is decomposed into a set of subsystems, one for each state of the radiometer. Each state represents a total-power-mode observation. The output signal of each subsystem is treated as a separate random process. The radiometer output is then considered as a sequence of samples obtained from the different random processes. An estimate of the measurand is calculated from samples of these random processes. The measurement uncertainty is computed from the statistics of the samples and the functional form of the estimator. The technique can be applied to all radiometers with designs that can be decomposed into a set of subsystems that represent total-power-mode observations.

3.3.1 Model Decomposition and Measurement Estimator

Figure 7a shows a model of a radiometer system that has $N+1$ measurement states. The states of the radiometer correspond to observations of the measurand, external calibration references, e.g T_{sky} shown in Fig 7a, or one of a number of calibration references. Measurement

states may also include additive noise coupled into the measurement path as indicated in the figure. The radiometer output depends on the radiometer state. At any instance in time the radiometer output corresponds to only one of its possible $N+1$ states; the timing of the state sequence is prescribed by $p(t)$ where $p \in \{A, 1, \dots, N\}$. Observations of the measurand correspond to the state $p = A$. Figure 7b illustrates a representation of the radiometer as a set of subsystems, one for each possible value of p . Each subsystem is mathematically modeled by a characteristic equation that describes the random process at its output. The random processes are treated as though each simultaneously exists. Figure 7c shows a time series of the $N+1$ processes. The output of the radiometer is a sample of only one of the processes at any given time. By decomposing the radiometer design in this way, transient effects between samples are neglected. Figure 7d shows a time series of the radiometer output for a particular state sequence.

Each subsystem is treated as a radiometer receiver operating in total-power mode. The mathematical model for the voltage output is given by (A.6) in Appendix A. The model includes inherent fluctuations of the receiver input and instability of the receiver gain. Although the radiometer state is not explicitly shown, its effect is implicit in the value of T_{sys} . For any p , the input to the receiver, $x(t, p)$, is defined to be a zero-mean wide-sense-stationary Gaussian random process with a white power spectrum given by

$$S_x(f, p) = kT_{sys}(p) = k(T_{rec} + T_p) \quad (3.1)$$

where k is Boltzmann's constant, T_{rec} is the receiver noise temperature referred to the receiver input. T_p is the equivalent antenna brightness temperature [Corbella *et al.*, 2002] referred to the receiver input for the radiometer state designated by p . For a lossless system, T_p is equal to the antenna temperature but T_p may also include noise contribution from system losses or injected noise, e.g. through a directional coupler. The output voltage, $v(t, p)$, is a function of time and radiometer state. The expected value of $v(t, p)$ is evaluated in Appendix A (see A.7 – A.10) and is a linear function of T_p ,

$$E\{v(t, p)\} = \bar{v}_p = \mu T_p + \beta \quad (3.2)$$

where μ is the receiver gain and β is the offset and are defined by (A.9) and (A.10), respectively.

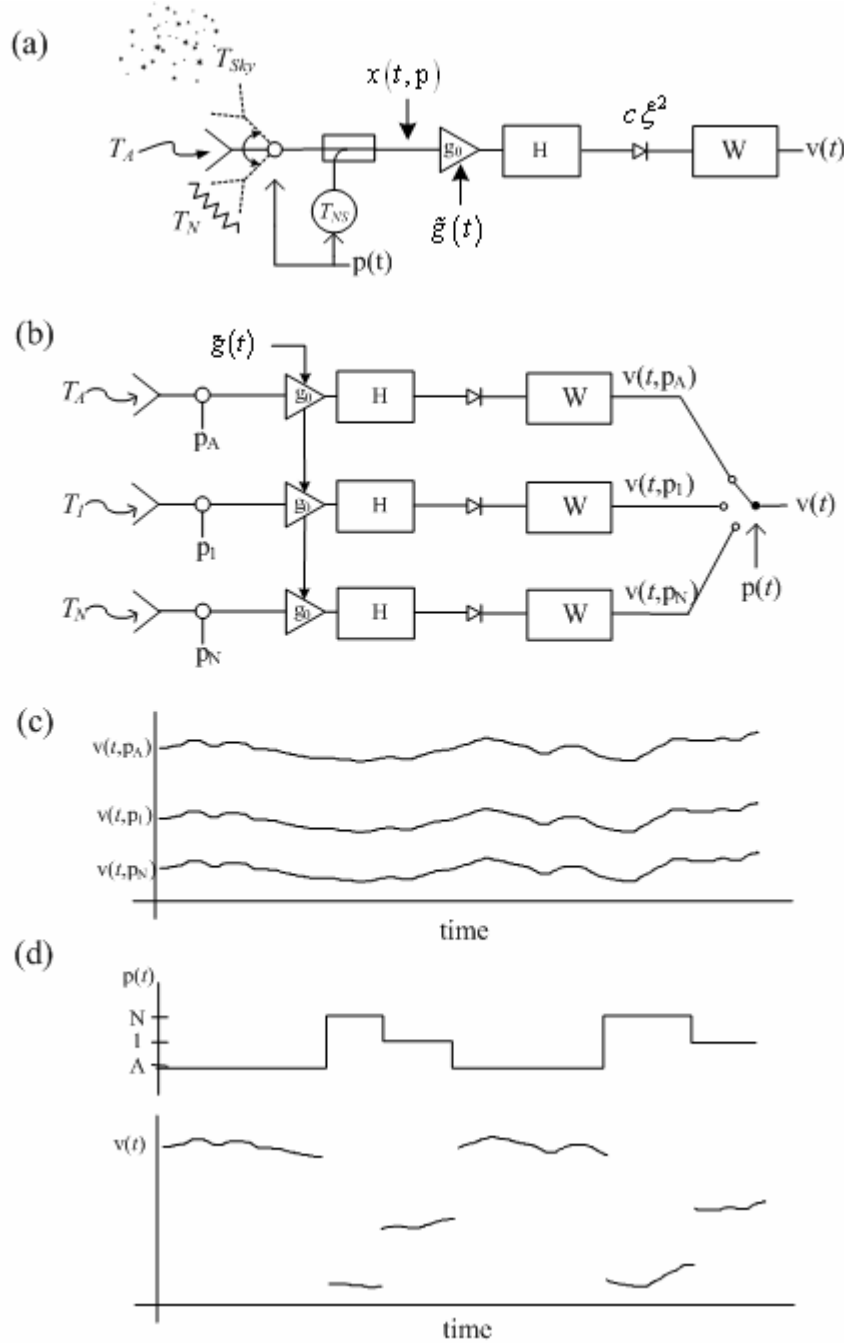


Figure 7: Decomposition of a general radiometer model. (a) A model of a radiometer with $N + 1$ measurement states. The state of the radiometer is controlled by $p(t)$. (b) The radiometer is expanded as a set of subsystems with each subsystem representing a total-power-mode measurement. (c) The signals out of the subsystems form a set of simultaneously existing random processes. (d) The radiometer output is a sequence of samples from the set of random processes.

When sampling the radiometer output, it is not possible to measure the mean value of voltage output given by (3.2) with zero uncertainty. Thus, the radiometer output is rewritten as the sum of the mean, \bar{v}_p , and a fluctuating component \tilde{v} ,

$$v(t, p) = \bar{v}_p + \tilde{v}(t, p) = \mu T_p + \beta + \tilde{v}(t, p) \quad (3.3)$$

where $\tilde{v}(t, p)$ is a zero mean random process. The variance of $\tilde{v}(t, p)$ can be found from the covariance of the output $v(t, p)$ given by (A.13) in Appendix A since $\sigma_{v_p}^2 = \sigma_{\tilde{v}_p}^2$. In anticipation of forming an estimator for the antenna brightness temperature, (3.3) is rewritten to express the brightness temperature as the sum of two random variables, i.e.,

$$T_p = mv(t, p) + b + \varepsilon(t, p) \quad (3.4)$$

where $m = \mu^{-1}$, $b = -\beta\mu^{-1} = T_{rec}$, and $\varepsilon(t, p) = -\tilde{v}(t, p)\mu^{-1}$. The slope m and offset b define the mean system response.

When making measurements with a radiometer, the brightness temperature at the radiometer input is usually not known but is estimated from a measurement of the output voltage. Equation (3.4) is used as a model to define an estimator for the input brightness temperature. At a particular instance in time the *measured* output is v_p ($p = A$ for the measurand) and the estimator for the input brightness temperature is

$$\hat{T}_p = mv_p + b. \quad (3.5)$$

The expected value of the estimator is

$$E\left\{\hat{T}_p\right\} = E\left\{mv_p + b\right\} = m\bar{v}_p + b = T_p. \quad (3.6)$$

The variance of the estimator is

$$\sigma_{T_p}^2 = E\left\{\left(\hat{T}_p - T_p\right)^2\right\} = E\left\{\varepsilon_p^2\right\} = \frac{\sigma_{v_p}^2}{\mu^2}. \quad (3.7)$$

The estimator \hat{T}_p is a random variable with mean and variance given by (3.6) and (3.7), respectively. The fluctuating component ε_p arises from the stochastic nature of the signal at the input of the receiver and instabilities within the receiver. This fluctuation is indistinguishable from fluctuations that may exist in T_p . The standard deviation of the estimator given by the square root of (3.7) is the *standard uncertainty* as defined by ANSI [1997, chapter 2] and is equal

to the radiometric resolution given by (2.6), since $\mu = \frac{\partial \bar{V}_p}{\partial T_p}$. The uncertainty as expressed by (3.7)

is based on the mean system response defined by m and b and, hence, does not include uncertainty due to imperfect calibration.

3.3.2 Estimator of the Measurand and Measurement Uncertainty

Generally, m and b in (3.5) are not known but must be estimated by calibrating the system. Therefore, the uncertainty in the estimated antenna brightness temperature should include the uncertainty in the estimates of m and b . An estimate of the measurand, i.e. the unknown antenna brightness temperature, must be obtained by using an estimate of the system response. An estimate of the measurand is derived from samples obtained from the different radiometer states. In the most general case, the estimator may be expressed as a function of random variables,

$$\hat{T}_A = f(x_1, x_2, \dots, x_K). \quad (3.8)$$

The set of random variables, x_i for $i \in \{1, \dots, K\}$, may include voltages, brightness temperatures of calibration references, physical temperatures of radiometer components, insertion losses, antenna beam efficiencies, etc..., i.e. any element in the system that contributes uncertainty to the estimator. The estimator, \hat{T}_A , differs from $\hat{\bar{T}}_A$ given by (3.5); \hat{T}_A is an estimate of the antenna brightness temperature based upon estimates of the system response, whereas, $\hat{\bar{T}}_A$ is an estimate of the antenna brightness temperature for a known system response, i.e. a perfectly calibrated system.

The uncertainty in the estimator is obtained by evaluating

$$\sigma_{\hat{T}_A}^2 = E \left\{ (\hat{T}_A - T_A)^2 \right\}, \quad (3.9)$$

where $T_A = f(\bar{x}_1, \bar{x}_2, \dots, \bar{x}_K)$ and $\bar{x}_i = E\{x_i\}$, assuming the estimator is unbiased. To evaluate (3.9), a multivariate Taylor series expansion about the mean value of each random variable is performed on (3.8). The multivariate expansion is

$$\hat{T}_A = \sum_{j=0}^{\infty} \left\{ \frac{1}{j!} \left[\sum_{i=1}^K (x_i - \bar{x}_i) \frac{\partial}{\partial x_i} \right]^j f(x_1, x_2, \dots, x_K) \right\} \Bigg|_{x_1=\bar{x}_1, x_2=\bar{x}_2, \dots, x_K=\bar{x}_K}. \quad (3.10)$$

Substituting the series expansion into (3.9) leads to the law of propagation of uncertainty given by ANSI, [1997, chapter 5]. By assuming the estimator is well approximated by a linear expansion for values of anticipated fluctuations, the series can be truncated at the second term, i.e. $j = 1$. The first term in the series expansion is T_A and cancels with T_A in (3.9). Thus,

$$\sigma_{\hat{T}_A}^2 = \sum_{k=1}^K \sum_{i=1}^K E \{ (x_k - \bar{x}_k)(x_i - \bar{x}_i) \} f_{x_k} f_{x_i} \quad (3.11)$$

where

$$f_{x_i} = \frac{\partial}{\partial x_i} f(x_1, x_2, \dots, x_K) \Big|_{x_1 = \bar{x}_1, x_2 = \bar{x}_2, \dots, x_K = \bar{x}_K}. \quad (3.12)$$

By assuming all of the random variables are independent, the uncertainty reduces to

$$\sigma_{\hat{T}_A}^2 = \sum_{i=1}^K \sigma_{x_i}^2 f_{x_i}^2 \quad (3.13)$$

where $\sigma_{x_i}^2$ is the variance of the random variable x_i . Randa [1998] provides an example application of the law of propagation of uncertainty by calculating the uncertainty in noise-temperature measurements of noise source standards. A comprehensive discussion and treatment of measurement uncertainty including the case for correlated variables is given by ANSI, [1997, chapter 4].

3.4 Least Squares Regression

Selection of calibration architectures and optimization of design parameters can be made by evaluating the measurement uncertainty. However, evaluation of measurement uncertainty requires an estimator for the measurand. As with selecting a calibration architecture, there exists a great deal of freedom when developing an estimator even though the form of the estimator is constrained by the radiometer design and its sampled states. In the following we develop an estimator based on Least Squares Regression (LSR). Though LSR can not be applied to all radiometer designs, the framework demonstrates the utility of measurement uncertainty for performing trade studies on a wide variety of radiometer designs. The advantages and limitations of using LSR are discussed in the following Section 3.4.

Consider a set of measurements that is made up of observations of calibration references and the measurand at certain times. The measurement set is $\{v_A, v_1, \dots, v_n, T_1, \dots, T_n\}$. (Note that

$\{v_p, T_p\}$ are values of the random variables $\{v_p, T_p\}$.) The set of measurements is used with (3.4) to form a set of characteristic equations,

$$\begin{aligned} T_A &= mv_A + b + \varepsilon_A \\ T_1 &= mv_1 + b + \varepsilon_1 \\ &\vdots \\ T_n &= mv_n + b + \varepsilon_n \end{aligned} \quad (3.14)$$

As in (3.4), m and b represent the mean response of the system. The value of the measurand, T_A , is not known but must be estimated from the data set. The measured voltage, v_A , is used to estimate the measurand by

$$\hat{T}_A = \hat{m}v_A + \hat{b} \quad (3.15)$$

where \hat{m} and \hat{b} are estimates of the system response. The value of ε_A in (3.14) is not known but its variance, $\sigma_{T_A}^2$, is given by (3.7); its standard deviation is equal to the radiometric resolution of the measurand observation.

Estimates of m and b are derived from the calibration measurements that comprise the remainder of the data set, i.e., $\{T_i, v_i\}$ where $i \in \{1 \dots n\}$. The calibration measurement pairs consist of the recorded output voltage, v_i , and the reference brightness temperature, T_i . Figure 8 illustrates the set of measurements. Note that there can be several measurements made at the same temperature T_i . The figure shows that n measurements are made at N different temperatures with $N < n$. The ε_i 's are not part of the data set and are not known but represent the deviation of the measurement pairs, $\{T_i, v_i\}$, from the mean system response. When T_i is the “true” antenna temperature, the variance of ε_i is given by (3.7). However, it is usual to approximate T_i through ancillary measurements and/or assumptions, e.g. by measuring the physical temperature of a calibration reference and its emissivity. In this analysis, the “true” value of T_i is assumed to be constant, however, the knowledge of T_i is treated as a random variable; thereby, the fluctuations in v_i are independent of the knowledge of the value of T_i . Subsequently, the “true” value of T_i is expressed as \bar{T}_i and uncertainty in the knowledge of \bar{T}_i is

$$\sigma_{\bar{T}_i}.$$

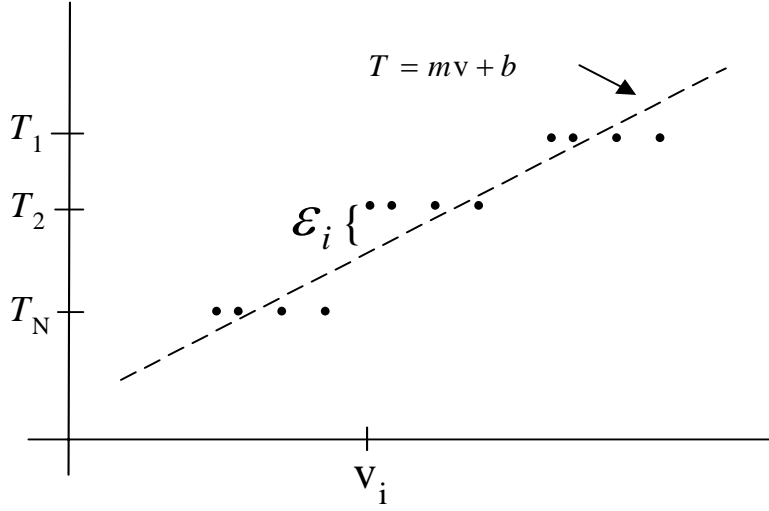


Figure 8: Graphical illustration of a calibration data set of n measurements made at N different temperatures with $n > N$. The dashed line is the response of the radiometer.

There are a number of different ways to use the data in (3.14) to derive estimates of the system response. For reasons discussed in Section 3.4, LSR has been chosen as the framework to obtain \hat{m} and \hat{b} . The estimated system response is found by minimizing the sum of the squared errors (see Appendix B.1), i.e. by minimizing E where

$$E = \sum_{i=1}^n \varepsilon_i^2 = \sum_{i=1}^n (v_i \hat{m} + \hat{b} - T_i)^2. \quad (3.16)$$

Applying LSR to the data set yields [Draper and Smith, 1998, chapter 1]

$$\hat{m} = \frac{\sum_{i=1}^n (v_i - \langle v_i \rangle_n) T_i}{\sum_{i=1}^n (v_i - \langle v_i \rangle_n)^2} \quad (3.17)$$

and

$$\hat{b} = \langle T_i \rangle_n - \hat{m} \langle v_i \rangle_n \quad (3.18)$$

where $\langle T_i \rangle_n$ and $\langle v_i \rangle_n$ are the arithmetic averages of the calibration data set given by

$$\langle T_i \rangle_n = \frac{1}{n} \sum_{i=1}^n T_i \quad (3.19)$$

and

$$\langle v_i \rangle_n = \frac{1}{n} \sum_{i=1}^n v_i. \quad (3.20)$$

Substituting (3.17) – (3.18) into (3.15) the antenna brightness temperature estimator is

$$\begin{aligned}\hat{T}_A &= \left(v_A - \langle v_i \rangle_n \right) \frac{\sum_{i=1}^n (v_i - \langle v_i \rangle_n) T_i}{\sum_{i=1}^n (v_i - \langle v_i \rangle_n)^2} + \langle T_i \rangle_n \\ &= f(v_A, v_1, \dots, v_n, T_1, \dots, T_n)\end{aligned}\quad (3.21)$$

Equations (3.17) and (3.18) are the best estimate of the slope and offset when all the measurements in (3.14) have an equal level of confidence, i.e. ε_i 's have equal variance. However, when the variance of ε_i 's are not equal (which is usually the case), a better estimate of the slope is obtained using weighted least squares regression. When the ε_i 's in (3.14) are correlated, generalized least squares regression can be used [Draper and Smith, 1998, chapter 5]. So long as ε_i 's and v_A have zero mean, \hat{m} , \hat{b} , and \hat{T}_A are unbiased estimators (see Appendix B.2). Note that the estimator given by (3.21) does not include m , b , \hat{m} , or \hat{b} but that fluctuations in the receiver response are embedded in the statistics of the sampled pairs $\{T_i, v_i\}$.

The measurement uncertainty of the estimator given by (3.21) is found by substituting (3.21) into (3.13). Here, all of the random variables that comprise the data set are assumed to be independent. This assumption implies that the covariance between samples of the receiver output (see (A.18) in Appendix A and the discussion following it) is much smaller than the variance of the samples, i.e., $C_v(\Delta t) \ll C_v(0)$ where Δt is the time interval between samples. As mentioned above, the stochastic fluctuations in the measured voltages are independent of the knowledge of the reference temperatures. In Appendix B.3 the measurement uncertainty is evaluated and found to be

$$\begin{aligned}\sigma_{\hat{T}_A}^2 &= \sigma_{T_A}^2 + \frac{\sum (\sigma_{T_i}^2 + \sigma_{\bar{T}_i}^2)}{n^2} + \\ &\quad \frac{(T_A - \langle \bar{T}_i \rangle_n)^2 \sum (\bar{T}_i - \langle \bar{T}_i \rangle_n)^2 (\sigma_{T_i}^2 + \sigma_{\bar{T}_i}^2)}{\left(\sum (\bar{T}_i - \langle \bar{T}_i \rangle_n)^2 \right)^2} + \\ &\quad \frac{2(T_A - \langle \bar{T}_i \rangle_n) \sum (\bar{T}_i - \langle \bar{T}_i \rangle_n) (\sigma_{T_i}^2 + \sigma_{\bar{T}_i}^2)}{n \cdot \sum (\bar{T}_i - \langle \bar{T}_i \rangle_n)^2}\end{aligned}\quad (3.22)$$

where the summations are performed over the $i = 1 \dots n$ measurements. In deriving (3.22), we make use of the equality of the partial derivatives, $f_{v_i}^2 = m^2 f_{T_i}^2$, and the relationships $\sigma_{T_i}^2 = m^2 \sigma_{v_i}^2$ and $\bar{T}_i = m\bar{v}_i + b$ to arrive at the simplified expression. Equation (3.22) expresses the uncertainty of the estimated brightness temperature in terms of the resolution of the measurand observation (σ_{T_A}), resolution of the reference measurements (σ_{T_i}), temperatures of the calibration references (\bar{T}_i), and uncertainty in the knowledge of the reference temperatures ($\sigma_{\bar{T}_i}$). This equation is the basis for making quantitative trade studies of the calibration algorithm for a radiometer design using an LSR estimator for the measurand. The first term on the right hand side of (3.22), $\sigma_{T_A}^2$, is the square of the radiometric resolution of the measurand. The next three terms arise from the uncertainty in the estimate of the system response and represent the effects of using imperfect calibration data. In the limit of perfect calibration, $\sigma_{T_i} \rightarrow 0$ and $\sigma_{\bar{T}_i} \rightarrow 0$, the measurement uncertainty converges to the radiometric resolution of the measurand. The formula for calculating measurement uncertainty using weighted LSR is developed in Appendix B.4 and is given by (B.32). Equations (3.22) and (B.32) are used in analyses presented in Chapter 4.

Before showing how (3.22) can be applied to study a system design, it is illustrative to consider the limiting case where $\sigma_{\bar{T}_i}^2 = 0$ and all $\sigma_{T_p}^2$'s, for $p \in \{A, 1, \dots, n\}$, are equal. Setting $\sigma_{T_i}^2 = \sigma_{T_A}^2$ and simplifying, (3.22) becomes

$$\sigma_{\hat{T}_A}^2 = \sigma_{T_A}^2 \left(1 + \frac{1}{n} + \frac{(T_A - \langle \bar{T}_i \rangle_n)^2}{\sum (\bar{T}_i - \langle \bar{T}_i \rangle_n)^2} \right). \quad (3.23)$$

Several observations can be made with regard to (3.23). The uncertainty in the calibrated response is minimum when the measurement value T_A is equal to the mean of the calibration temperatures. The uncertainty is improved by increasing the separation of the calibration temperatures; the larger separation yields a larger value in the denominator of the third term on the right hand side. The uncertainty is unbounded when all the reference measurements are made at the same reference temperature, i.e. when $\bar{T}_i = \langle \bar{T}_i \rangle_n$ for $i = 1 \dots n$. Finally, the uncertainty is improved by increasing the number of calibration measurements. In the limit for increasing n , the uncertainty in the calibrated estimate converges to the radiometric resolution. These results

are consistent with experiment design considerations for the regression of data as discussed by *Draper and Smith*, [1998, pp. 86 – 89].

Least squares regression provides a framework for calculating the measurement uncertainty by which the performance of a calibration design can be assessed. Application of the method is simple and straightforward. In Chapter 4, examples illustrate how LSR can be used to study system design and evaluate the influence of design parameters on instrument performance.

3.5 Discussion

In the preceding sections, a technique is described that uses measurement uncertainty as a figure of merit to assess the performance of a variety of radiometer designs. The technique can be applied to radiometer designs that can be decomposed into a set of total-power-mode receiver subsystems; the output of each subsystem is a random process described by a characteristic equation. The radiometer output is a sequence of samples from the different random processes. An estimator for the measurand is derived from samples of the different subsystems. Measurement uncertainty is calculated from the functional form of the estimator and the statistics of the random variables comprising the estimator.

The form that the estimator can take depends on the radiometer design and its sampled states. In Chapter 4 least squares regression is used as a convenient framework to demonstrate the utility of measurement uncertainty as a figure of merit. The LSR approach offers a number of advantages. LSR minimizes the measurement error in the least squares sense and can be applied to a wide variety of calibration designs for performing tradeoff studies of design parameters. LSR provides a simple and straightforward way of computing the measurement uncertainty in terms of parameters (e.g. standard uncertainty of the calibration measurements) convenient for interpretation; the linear algebra required to compute the measurement uncertainty is easily programmed. The influence of applying weights to the calibration measurements can be evaluated using weighted LSR. For calibration measurements characterized by Gaussian statistics, the optimum weights are inversely proportional to the standard uncertainty of the calibration measurements. When the calibration measurements are correlated, generalized LSR can be used to include the influence of their correlation.

Methods other than LSR are often used to form an estimator and many calibration implementations are not readily expressed as a set of equations in the form of (3.14) that can be solved by LSR. For example, the set of equations describing a radiometer that alternately couples

noise into the antenna measurement path and uses a set of external calibration measurements (tier-3) to estimate the value of additive noise cannot be put in the form of (3.14); such a calibration scheme is evaluated in Section 4.2. It should be noted that the functional form of the estimator in (3.21) does not include the slope and offset but does include those random variables (i.e. calibration measurements) from which the slope and offset are estimated. Regardless of the system architecture, an estimator of the measurand will take a functional form; the functional form can then be used to calculate the measurement uncertainty based on the stochastic properties of the variables that comprise the estimator.

When modeling the measurement uncertainty for a design study, one has freedom in assigning the value of uncertainty to each component that contributes uncertainty. Consider for example a design analysis in which a noise source exhibits thermal instability, the uncertainty associated with the noise source measurement can be adjusted and its influence on the measurement uncertainty understood. One can then choose to modify the calibration design or functional form of the estimator to compensate for anticipated noise source instability. Thereby, analysis of measurement uncertainty based on stochastic models of anticipated fluctuations can be a valuable aide in understanding the influence of component characteristics on system performance.

In the next chapter, the technique presented for calculating measurement uncertainty is used to assess the performance of a variety of calibration architectures and to study optimization of design parameters.

CHAPTER 4

APPLICATION OF THE THEORY

4.1 Introduction

When designing a radiometer there are several constraints applied to the design based upon sampling requirements, operating environments, and limitations due to budgetary or more simply technical difficulties. Even with these constraints there usually exist many degrees of freedom in designing the calibration scheme for the system. In Chapter 3 measurement uncertainty was introduced as a figure of merit by which to quantify the performance of a calibration scheme. In Section 3.3 a general method for calculating measurement uncertainty was presented. In Section 3.4 least squares regression (LSR) was introduced as a simple framework for calculating measurement uncertainty that could be applied to a wide variety of calibration designs.

In this chapter, measurement uncertainty is used to evaluate the performance of a variety of radiometer designs. The analysis presented assumes that the receiver response is wide-sense-stationary; drifts in the response are not considered in this analysis. In Sections 4.1 – 4.6, the LSR framework is used to evaluate the effect of calibration reference temperature, the fraction of time spent calibrating, number of calibration references, reference averaging, and weighting of the calibration data on the performance of calibration designs. Section 4.6 describes a practical application of measurement in evaluating a design that is being considered for a spaceborne instrument. In Section 4.7 the general formulation presented in Section 3.3.2 is applied to a radiometer that uses noise injection. External calibration is used to estimate the equivalent noise source temperature; the general formulation for calculating measurement uncertainty is used to quantify how parameters for the external calibration affect the uncertainty of the measurand estimate.

4.2 Cross-Track Imaging Radiometer

First consider a design based upon the Millimeter-Wave Imaging Radiometer (MIR). A brief description of the MIR was presented in Chapter 1. Photographs of the instrument are shown in Fig. 1. A detailed description of the MIR can be found in [Racette *et al.*, 1996] and a description of the salient characteristics of its calibration design follows. The MIR has five

receivers spanning 89 GHz to 340 GHz. The lack of electronic switches at these high frequencies and the short integration times required for imaging led to the decision of using total-power mode. Calibration is achieved by periodically observing two blackbody references at different temperatures. Images are generated by rotating the antenna patterns across a field of view using a flat mirror canted at 45° angle. The across-track swath width is 100° centered about nadir. At cruising altitude of ~20km the ER-2 airspeed is about 200m/s. The nominal full-width half-power beam width for each of the receivers is 3.5°. To achieve contiguous images at half altitude (~10km) the instrument must scan the field of view every 3 seconds. An illustration of its scan profile is shown in Fig. 1d. The desire to avoid gaps in the images and the need for frequent calibration to circumvent errors in calibration due to drifts in the receiver gain and offset led to the decision to include calibration observations during each scan cycle. The constraint on the scan cycle period leads to a trade off between time available to observe the scene and time available to observe the calibration references. A latency interval exists during which time the mirror must switch between the calibration references and the beginning and end of the field of view. The latency interval also includes the settling time required for the mirror motion and post-detection filters. For the MIR, the latency interval is dominated by the rotation of the scan mirror. However for a system utilizing electronic switches, the time to switch between calibration references and the measurand can be significantly shorter than the settling time of the receiver. Of course it is desirable to keep the latency interval as short as possible.

The total scan period is comprised of three components as follows

$$\tau_{tot} = \tau_s + \tau_{cal} + \tau_{lat} \quad (4.1)$$

where τ_s is the time spent observing the measurand, τ_{cal} is the time spent calibrating, and τ_{lat} is the latency interval. A relationship between the pixel integration time and calibration integration time can be derived from (4.1). Assume there are M pixels for each swath scan and that $\tau_s = M\tau_A$ where τ_A is the pixel integration time. Furthermore, assume the integration time at each calibration reference is equal to τ_i and there are N calibration references, $\tau_{cal} = N\tau_i$. Based upon the requirement for contiguous coverage the cycle period is $\tau_{tot} = 3\text{s}$. For the MIR, there are M=56 pixels, N= 2 calibration references, and $\tau_{lat} = 0.5\text{s}$. Using these values a relation between the pixel integration time and calibration reference integration time is obtained,

$$\tau_A = \frac{2.5 - 2\tau_i}{56} . \quad (4.2)$$

Relationship (4.2) for τ_A and τ_i is used in Figs. 9 – 13. Calculations for these figures use pre-detection bandwidth, $B = 1$ GHz, and the receiver noise temperature $T_{rec} = 500$ K (except where noted in Fig. 13). Regular (unweighted) least squares regression is used in the calculations. A single set of calibration measurements, i.e. $n = N$, are used; perfect knowledge of the reference temperatures is assumed, i.e. $\sigma_{\bar{T}_i} = 0$; and gain fluctuations are neglected, i.e. $\tilde{g}(t) = 0$. In the figures that follow, the uncertainty in the measurand brightness temperature estimate is calculated using (3.22). The uncertainty in the calibration measurements, σ_{T_i} , and the resolution of the measurand observation, σ_{T_A} , are calculated from (2.7) using

$$\sigma_{T_p} = (T_{rec} + T_p)(B\tau_p)^{-\frac{1}{2}} , \quad (4.3)$$

where $p \in \{A, 1, \dots, n\}$.

Figure 9 shows the standard uncertainty in the estimate, \hat{T}_A , as a function of measurand brightness temperature, T_A . Two calibration references are viewed each for $\tau_i = 200$ ms. The pixel integration time is $\tau_A = 38$ ms. Three sets of curves are shown. The dotted curve shows the uncertainty in the estimate based solely on the resolution of the pixel measurement, σ_{T_A} . The other two curves illustrate the effect of calibration reference temperature on the measurement uncertainty. Markers on the abscissa indicate the temperatures of the calibration references for two cases. One calibration reference is maintained at 330K. The other reference floats at the ambient temperature which in flight is ~ 250 K; for laboratory measurements, the temperature of the ambient target is ~ 300 K. When the calibration data is interpolated the uncertainty in the estimate is nearly equal to the resolution of the measurement. The curves show how the uncertainty in the estimate increases as the calibration data are extrapolated. The advantage of having large separation in the calibration reference temperatures is apparent. For $T_A = 100$ K the uncertainty is improved by nearly a factor of 3 with the larger separation of reference temperatures.

Figure 10 shows how the measurement uncertainty changes with calibration measurement integration time. The measurand brightness temperature is $T_A = 100$ K. As indicated, the two

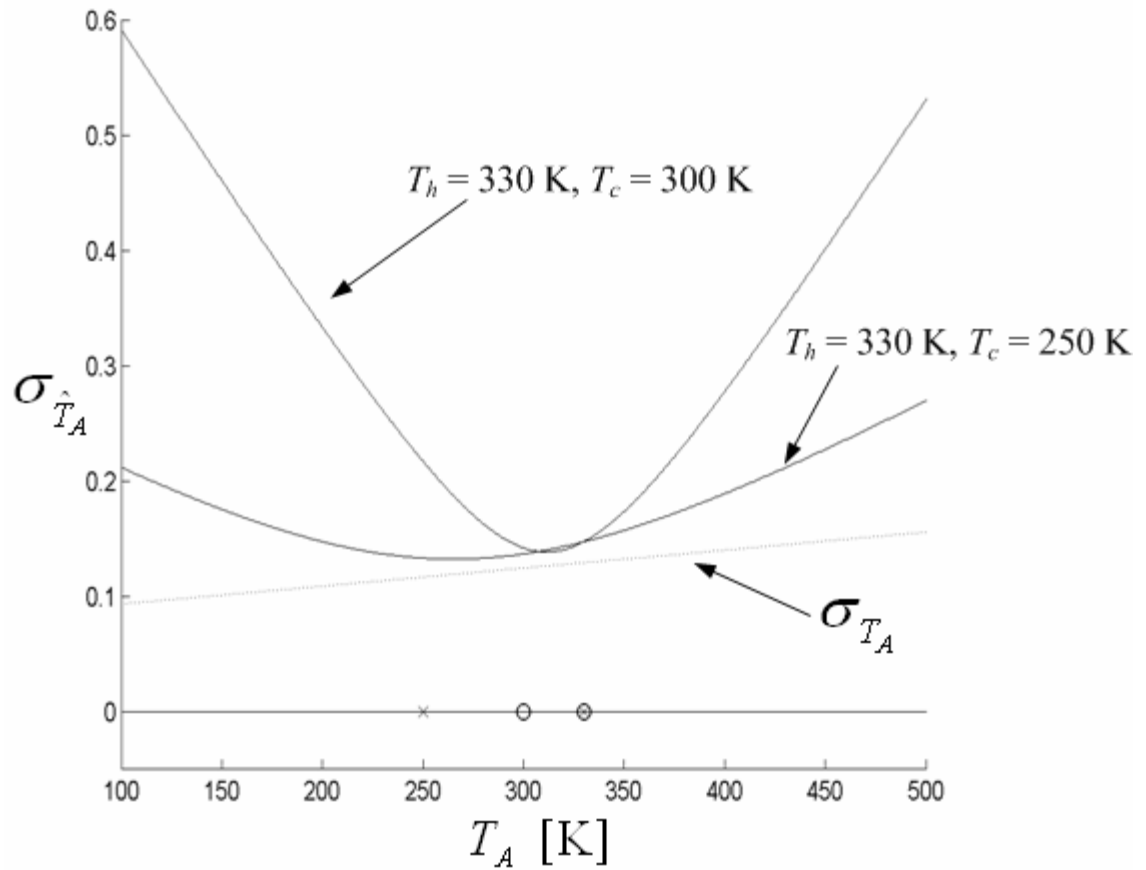


Figure 9: Measurement uncertainty versus measurand brightness temperature for two pairs of calibration target temperatures. The circles and x's on the abscissa indicate the temperatures of the calibration references. The dotted curve shows the resolution of the measurand observation.

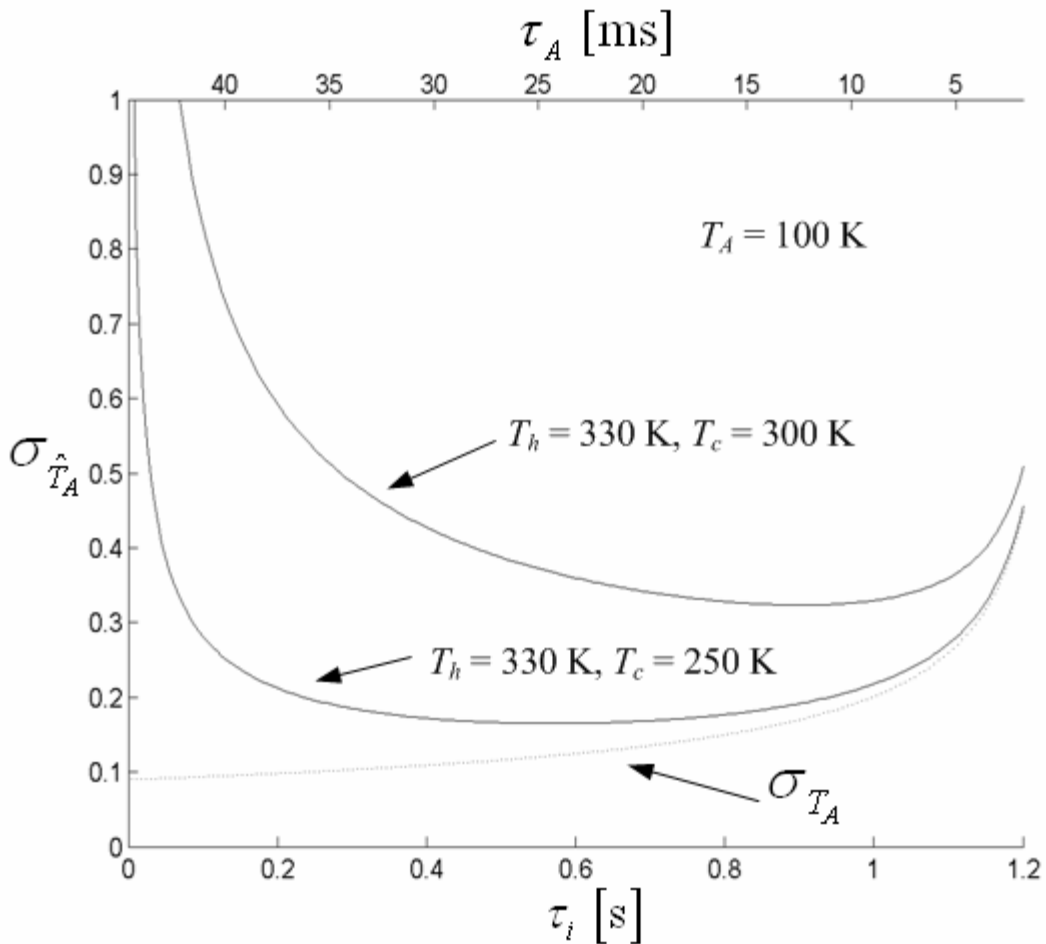


Figure 10: Measurement uncertainty as a function of time spent at each calibration reference (bottom abscissa) and time spent observing the measurand (top abscissa) for one pair of calibration target temperatures. The dotted curve shows the resolution of the measurand observation.

curves represent the same calibration reference temperatures shown in Fig. 9. Again the dotted curve shows the standard uncertainty of measurement based solely on the resolution at the measurand temperature. The top abscissa indicates the pixel integration time; the bottom abscissa indicates the calibration reference integration time. On the left side of the plot, uncertainty is dominated by uncertainty in the regression of the calibration data; not enough time is spent calibrating. On the right side, uncertainty is dominated by the resolution of the measurand observation; not enough time is spent observing the measurand. The optimum integration times correspond to the uncertainty minima. For laboratory measurements when the extrapolation of the calibration data is greater, it is advantageous to spend more time calibrating than when in flight. The curves illustrate how calibration reference temperatures affect the trade off between time spent calibrating and observing the measurand. It should be noted that in the original MIR design, the calibration target integration time was set to 150 ms. These curves indicate the optimum integration time for the MIR in flight is \sim 600 ms for a single scan. When calibration measurements are averaged over multiple scans, the optimum integration time will decrease, e.g. to \sim 340 ms for a five scan average. Reference averaging is discussed in Section 4.2. Figure 11 shows a composite of curves like those in Figs. 9 and 10. The receiver noise temperature is $T_{rec} = 500$ K. The cold reference temperature is $T_c = 250$ K, the measurand temperature is $T_A = 100$ K. The three dimensional plot illustrates the trade space between calibration target temperature, calibration integration time and measurement uncertainty.

Latency is introduced when the radiometer changes states and no meaningful radiometric data can be collected. For the MIR, the latency is dominated by the mechanical rotation of the mirror between the scene and the calibration targets. Figure 12 illustrates the affect of latency on the measurement uncertainty. The receiver, hot, cold, and measurand temperatures are 500 K, 330 K, 250 K, and 100 K, respectively. Three values of latency are shown in the figure,

$\tau_{lat} = 0$ s, $\tau_{lat} = 0.5$ s and $\tau_{lat} = 1.5$ s. The programming of the stepper motor on the MIR has been optimize to minimize the latency resulting in $\tau_{lat} = 0.5$ s. Some degradation in performance occurs because of this latency. Note that for the MIR, $\tau_i = 0.15$ s and latency has on a small effect on performance. However, if the scan profile were optimized the effect would be greater. For $\tau_{lat} = 1.5$ s, corresponding to 50% of the cycle period, the minimum uncertainty would increase from \sim 0.15 K (for no latency) to \sim 0.21 K or by \sim 40%. Clearly, it is desirable to

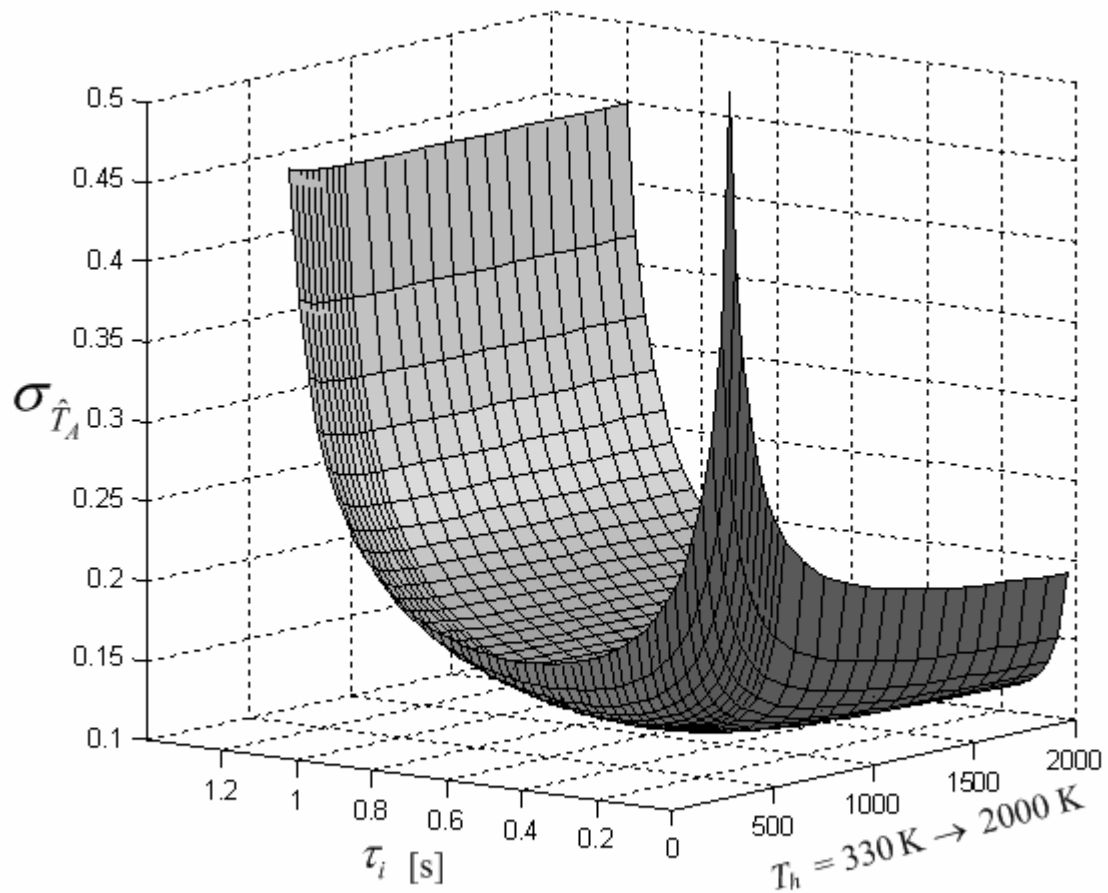


Figure 11: A composite of curves illustrating the relationship between measurement uncertainty, calibration reference integration time, and hot reference load temperature. The scene temperature is $T_A = 100$ K and the cold load temperature is $T_c = 250$ K.

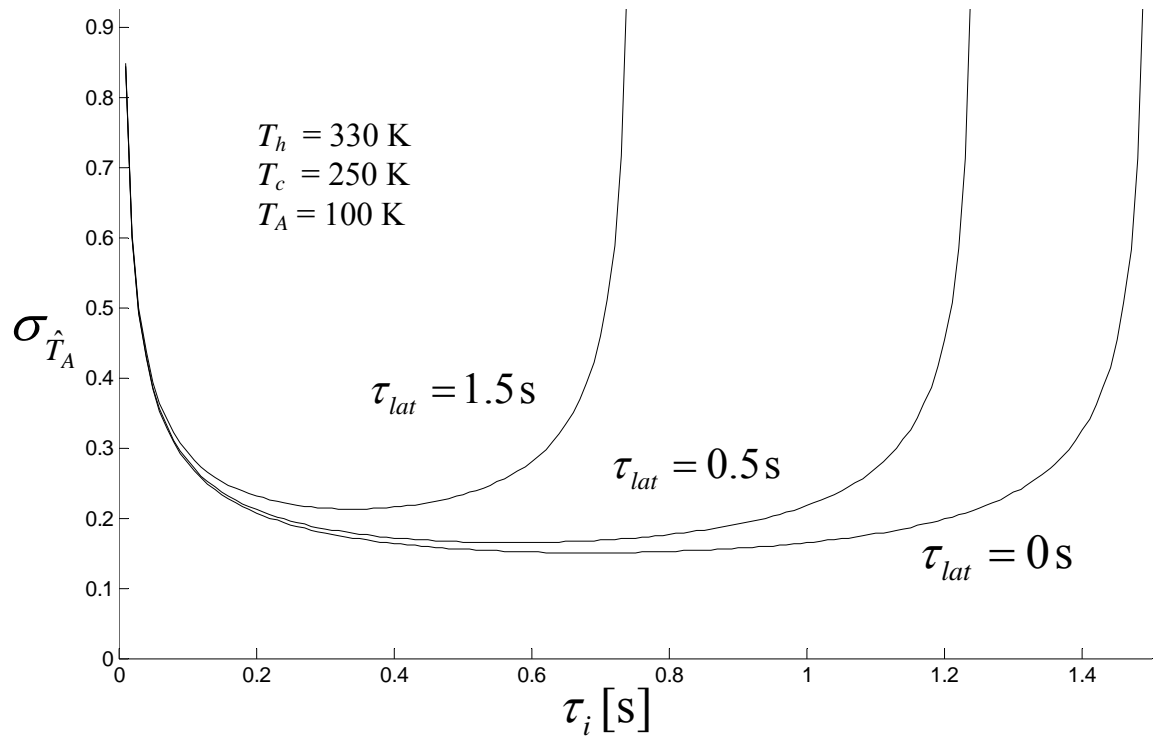


Figure 12: Measurement uncertainty as a function of time spent at each calibration reference illustrating the effect of latency.

minimize latency in designing a radiometer calibration scheme and including latency in the calculation of measurement uncertainty is a way to quantify its effect.

In Fig. 13 measurement uncertainty is again plotted as a function of calibration reference integration time. The hot, cold, and measurand temperatures are 330 K, 250 K, and 100 K, respectively. Shown is a set of four curves representing a range of T_{rec} between 0 K and 2000 K as indicated. As can be seen by the different levels of the curves, measurement uncertainty is a sensitive function of the receiver noise temperature. However, above $T_{rec} = 500$ K the uncertainty minimum is a weak function of the calibration integration time; for $T_{rec} < 500$ K the dependence is stronger. The dashed curve intersects the uncertainty minima and is calculated for a wider range of T_{rec} . Since the receiver noise temperatures of the MIR fall between 500 and 2000 K, optimization of the scan cycle for one receiver channel should apply to all five.

Figures 9 – 13 provide basis for assessing the trade off between performance and system parameters. For example, the advantages of achieving wider temperature separation for the calibration references can be weighed against the additional costs incurred and the performance gained.

4.3 Calibration Using More Than Two References

Some radiometers use measurements from more than two references to estimate the system response [Racette *et al.*, 1998; Blackwell *et al.*, 2001; Tanner and Riley, 2003]. Figure 14 shows how the estimate uncertainty changes with the number of references, i.e. N, used for calibration. Three cases are shown for N=2, N=3, and N=100. The reference temperatures are evenly distributed between $T_c = 250$ K and $T_h = 330$ K, e.g., for N = 3 the reference temperatures are $T_1 = 250$ K, $T_2 = 290$ K, and $T_3 = 330$ K. The calculations assume a fixed time interval for calibration, i.e. $\tau_{cal} = 0.4$ s; the integration times for each reference observation are equal, i.e., $\tau_i = \tau_{cal}N^{-1}$. The latency interval remains fixed, $\tau_{lat} = 0.5$ s, independent of the value of N. As in Fig. 9 the pixel integration time is $\tau_A = 38$ ms, $B = 1$ GHz, and $T_{rec} = 500$ K. The measurement uncertainty is minimum when only two references are used. A third reference results in marginal increase in the estimate uncertainty. The increase in uncertainty can be

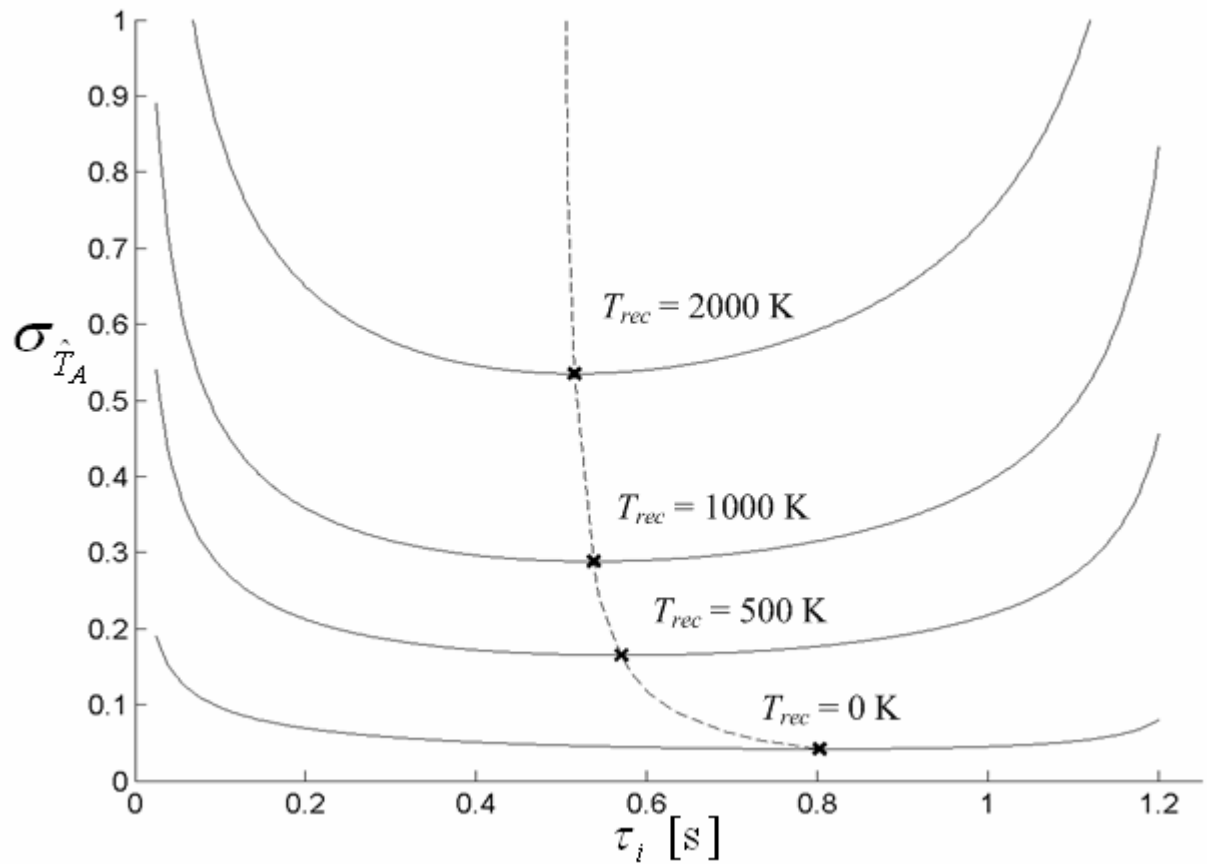


Figure 13: Measurement uncertainty as a function of calibration reference integration times for different receiver noise temperatures. The dashed curve passes through the minimum uncertainty over a range of receiver noise temperature.

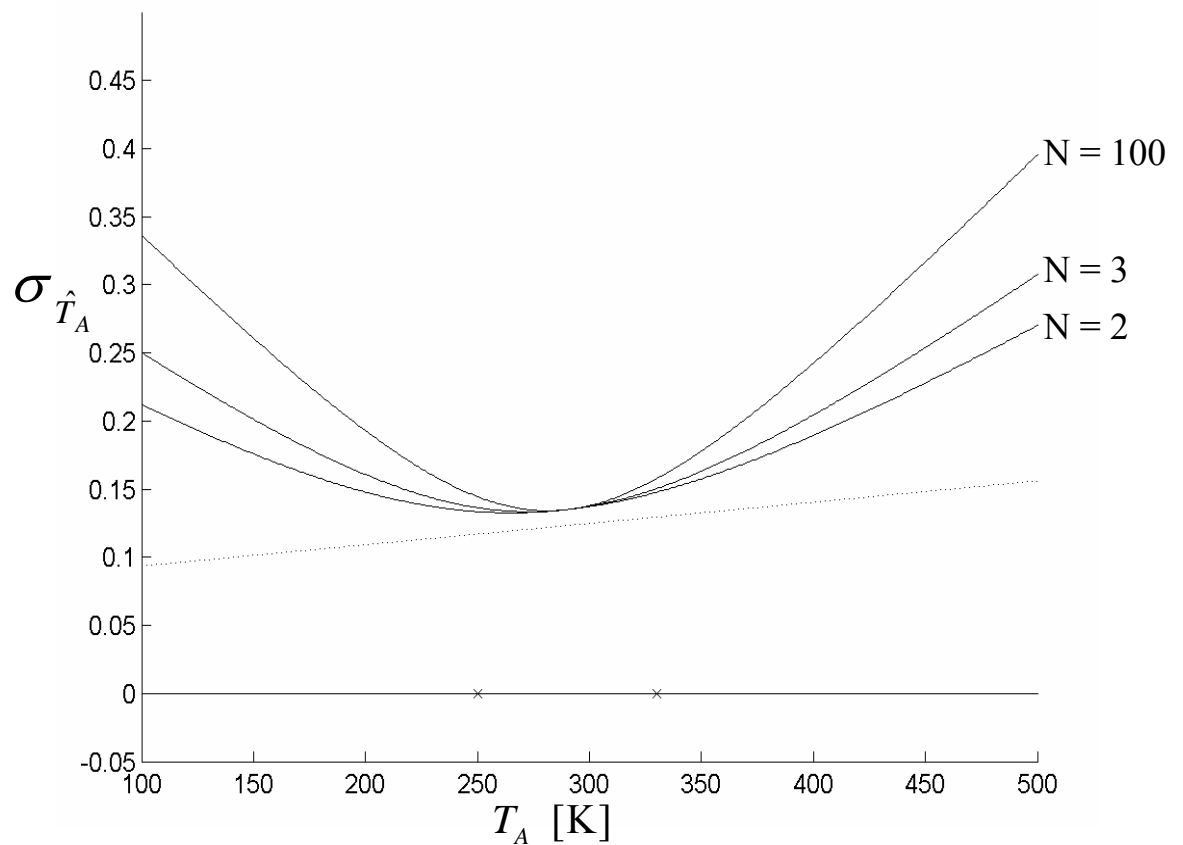


Figure 14: Measurement uncertainty as a function of measurand temperature for different numbers of reference temperatures used in the calibration. Reference temperatures are evenly distributed between 250 K and 330 K.

contrasted with the benefit of having additional degrees of freedom from which goodness of fit can be obtained by the regression. For example, additional reference measurements may be desired to monitor the linearity of the receiver response. Because the uncertainty will increase for larger latency intervals one should anticipate the uncertainty to be worse if adding additional references results in increased latency. The effect is easy to calculate given a model for the latency interval as a function of N.

4.4 Reference Averaging

In this section the effect of reference averaging on a calibration scheme is examined. Two cases are considered. In the first case a single reference and measurand observations are interleaved. The results are shown to be consistent with previously published results when the measurand and reference are at the same temperature. In the second case, reference averaging is applied to a calibration scheme which switches between three references and the measurand.

A sequence of measurements is shown in Fig. 15a where observations of the measurand and a single reference are interleaved. The measurand and reference temperatures are T_A and T_{ref} , respectively. The cycle period is $\tau = 1$ second during which time the reference is observed for τ_i seconds and the measurand is observed for $\tau_A = \tau - \tau_i$. An estimate of the calibration is obtained from M observations of the reference made over an interval $T_w = M\tau$. In order to derive an estimate of the receiver response at least two reference temperatures need to be observed. Hence, a second calibration measurement at temperature, T_2 , is assumed to occur outside the interval T_w ; the temperature T_2 is different than T_{ref} . The uncertainty of this second calibration measurement is assumed to be zero, i.e. $\sigma_{\hat{T}_2} = 0$, in order to minimize its influence on the calculation of measurement uncertainty. In this example, $B = 20$ MHz and $T_{rec} = 500$ K are assumed. The uncertainties of the measurand and reference observations are calculated using (4.3). The measurement uncertainty of a single measurand observation is calculated using (3.22) and then divided by $\sigma = (T_A + T_{rec}) \cdot (B\tau)^{-0.5}$ to obtain the uncertainty relative to the total-power-mode observation with perfect calibration.

The relative uncertainty for the measurement sequence shown in Fig. 15a is plotted in Fig. 15b. The results shown are for the balanced case where the reference and measurand are the same, i.e. $T_A = T_{ref} = 300$ K. The results do not depend on the temperature of the second

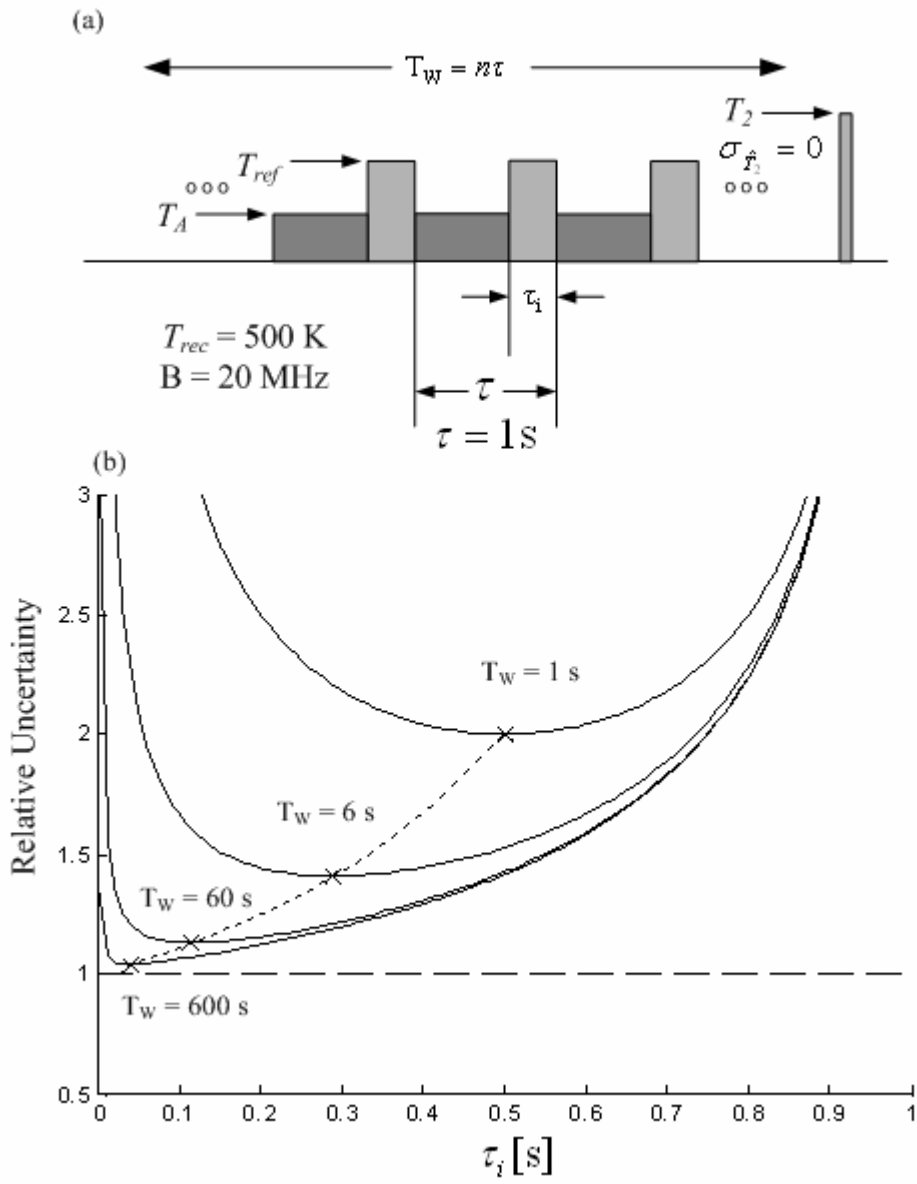


Figure 15: Optimization of switching sequence for a single-reference switched radiometer. (a) A diagram of a time series of measurements from a single-reference switched radiometer. Reference-averaging is applied to the reference measurements over an interval T_W . A second reference, T_2 , is observed with zero uncertainty outside the interval T_W . (b) The relationship between the reference-averaging window width, the reference integration time, and relative uncertainty is shown for the case when $T_{ref} = T_A = 300$ K. The dotted curve indicates the minimum as predicted by Bremer [1979].

calibration reference, T_2 . For $T_w = 1$ and $\tau_i = 0.5$ s the calculations predict that the relative uncertainty is equal to that of a Dicke radiometer with a 50% duty cycle, i.e. two times that of a total-power mode observation of the measurand. The dotted curve in Fig. 15b was calculated using equations (16) and (17) from Bremer [1979] which gives the minimum resolution for a balanced ($T_A = T_{ref}$) switched reference radiometer with asymmetric switching. The results of the LSR analysis for the balanced case are consistent with those of Bremer. However for the unbalanced case, i.e. $T_{ref} \neq T_A$, the techniques do not agree; the magnitude and sign of the difference in the techniques depend upon the values used in the calculations. Bremer's formula (see (4) in Bremer [1979]) expresses the uncertainty as the root-sum-square of the resolutions of the measurand and reference measurements and does not account for uncertainty in the estimate of the receiver response.

Figure 16a shows a representative sequence of measurements from a switched-three-reference radiometer. The three reference temperatures are $T_1 = 300$ K, $T_2 = 500$ K and $T_3 = 800$ K. The receiver noise temperature is $T_{rec} = 500$ K and the pre-detection bandwidth is 20 MHz. The time spent calibrating, $3\tau_i$, is split evenly between the three references; the cycle period is $\tau = 1$ second and the measurand is observed for $\tau_A = \tau - 3\tau_i$; latency due to switching between references is assumed negligible. The measurand brightness temperature is $T_A = 100$ K. The relative uncertainty is calculated the same way as in Fig. 15b.

Figure 16b illustrates the relationship between the calibration integration time and measurement uncertainty for different observation window lengths, T_w , over which reference measurements are used for calibration. The measurement uncertainty has been normalized by the radiometric resolution of a total-power measurement with a 1 second integration time. The curve for $T_w = 1$ s corresponds to a single set of calibration measurements, $n = N = 3$, and yields a minimum uncertainty of ~ 4.7 times that of the resolution in total-power mode. In this case the measurand is viewed only $\sim 21\%$ of the cycle period. The dashed line indicates the minimum uncertainty as a function of calibration integration time and observation window. Dramatic improvement in measurement uncertainty results by increasing the window over which multiple calibration measurements can be used. Improvement in measurement uncertainty results partly from the increased fraction of time spent observing the measurand and to a greater extent from improving the estimate of the system response. For a 10 minute window, $T_w = 600$ s, the

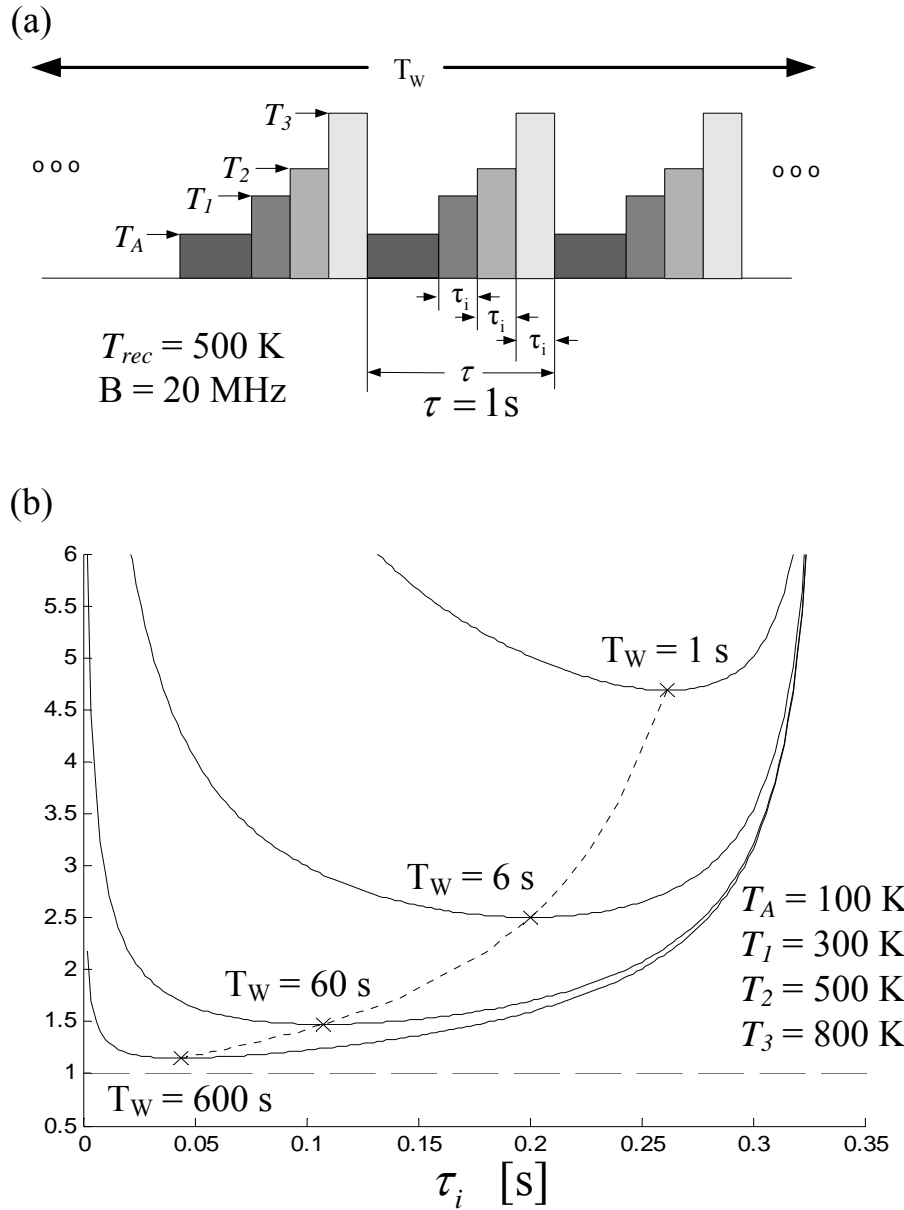


Figure 16: Optimization of switching sequence for a three-reference switched radiometer. (a) A diagram of a time series of measurements illustrating a window over which reference-averaging is applied to the calibration measurements. (b) The relationship between the reference-averaging window width, the calibration reference integration time, and relative uncertainty. The dotted curve is the minimum relative uncertainty calculated over a range of T_W .

minimum relative uncertainty is 1.16 . When considering large observation windows one should be concerned with the nonstationary fluctuations in the receiver. Calculations using a nonstationary model for the receiver fluctuations reveal that the shapes of the curves in Fig. 16b are largely unaffected, however, for long averaging intervals the curves are shifted upward yielding greater measurement uncertainty. The treatment of nonstationary fluctuations is not presented in this dissertation.

4.5 Weighted Regression of Calibration Data

Thus far all the analysis that has been presented has used (3.22) to calculate measurement uncertainty. Equation (3.22) is based on uniform weighting of the calibration data. Improvement in the performance of the calibration algorithm can be obtained by giving those calibration data that have greater uncertainty less weight in the calculation of the measurement estimate. The weighted estimator is formed by using weighted least squares regression; the estimator and weighted measurement uncertainty are presented in Appendix B.4. A comparison between uniform LSR and weighted LSR is shown in Fig. 17. A discussion of the calculations follows.

To examine the advantages of weighted LSR, a three point calibration is considered. The three reference temperatures are $T_1 = 250$ K, $T_2 = 300$ K, and $T_3 = 500$ K. The calibration reference integration time for each reference is $\tau_i = 200\text{ ms}$, and the integration time for the measurand is $\tau_A = 38\text{ ms}$. The receiver temperature is $T_{rec} = 500\text{ K}$ and the bandwidth is $B = 1$ GHz. Equation (4.3) is used to calculate the resolution of the calibration and measurand observations. The resolution of the measurand observations are 0.053 K, 0.0566 K, and 0.0707 K for T_1 , T_2 , and T_3 , respectively. The differences result from the difference in the noise temperature of the references. To better illustrate the improvement the weighted LSR can yield, uncertainty in the knowledge of the reference temperatures ($\sigma_{\bar{T}_i}$) is assumed, i.e. 0.5 K, 0.1 K, and 3.0 K for T_1 , T_2 , and T_3 , respectively. For uniform weighting (3.22) is used in the same manner as previously presented. Equation (B.33) is used to calculate the measurement uncertainty using weighted LSR; the weights in the calculation are given by (B.30). Plotted in Fig. 17 is the measurement uncertainty as a function of measurand brightness temperature for uniform and weighted LSR. For uniform weighting, the minimum uncertainty occurs between T_1 and T_2 ; even though each calibration measurement is given equal weight in the regression of the

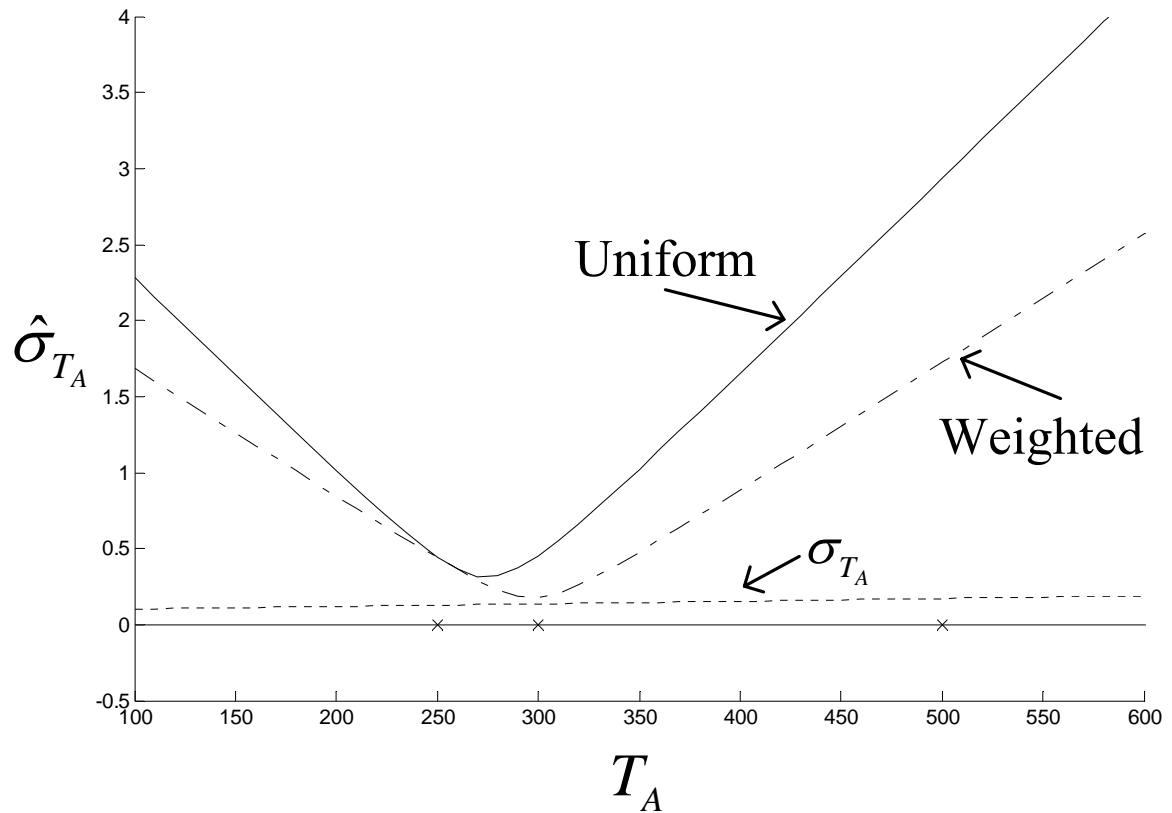


Figure 17: A comparison of measurement uncertainty as a function of measurand brightness temperature when uniform weighting and optimal weighting of calibration data are used. A three point calibration is assumed; the temperatures of the three references are labeled with an ‘x’ on the abscissa. Uncertainty in the calibration measurements includes uncertainty in the knowledge of the reference temperatures.

receiver response, the measurement uncertainty is minimum near those calibration data that have less uncertainty. Recall the estimator, (3.21), does not contain information regarding the uncertainty of the calibration measurements; but the calculation in (3.22) uses the uncertainty in the calibration measurements to estimate the measurement uncertainty. The advantage of using the uncertainty information in forming the estimator (compare (3.17) and (3.18) with (B.24) and (B.25)) is shown by the weighted LSR curve in Fig. 17; an overall improvement is observed. The measurement uncertainty near T_2 is reduced by nearly a factor of ~ 2.5 by using weighted LSR. Clearly, improvement in the estimator results from weighting the calibration measurements. However, it should be pointed out that when only two calibration data pairs are used to form the estimator, the weights have no effect on the measurement uncertainty since the two data pairs are needed to solve for two unknowns.

Applying weights to a time series of calibration data is commonly done. More weight is given to the calibration data that occur most close in time to the measurand observation. The benefit of weighted averaging of time series of calibration data can be evaluated in the context of nonstationary receiver fluctuations. Nonstationary receiver fluctuations are not treated in this dissertation.

4.6 Two-point Versus Three-point Calibration: A Case Study

In a study that was performed for a spaceborne sensor designed for cloud studies, the question came up regarding the performance of using a two point versus a three point calibration. The question stemmed from the possibility of having one calibration reference, i.e. the space view, obscured by part of the satellite bus. Following is a description of how measurement uncertainty was used to quantify the effect of eliminating the space view from the instrument design and instead using two blackbodies for calibration.

The sensor under consideration is an earth observing conical scanner. Images are formed by rotating the receivers and antennas on a platform. The science requirements for this instrument require a minimum 120° field of views (FOV's) in the fore and aft directions along the spaceflight track. The instrument concept calls for calibration to be performed by viewing calibration references during parts of the scan that fall outside the field of view; thus, a maximum of 1/3 of the scan (or 60° on each side) is available for calibration. Figure 18a shows two instrument configurations under consideration. In each configuration, a receiver mounted in

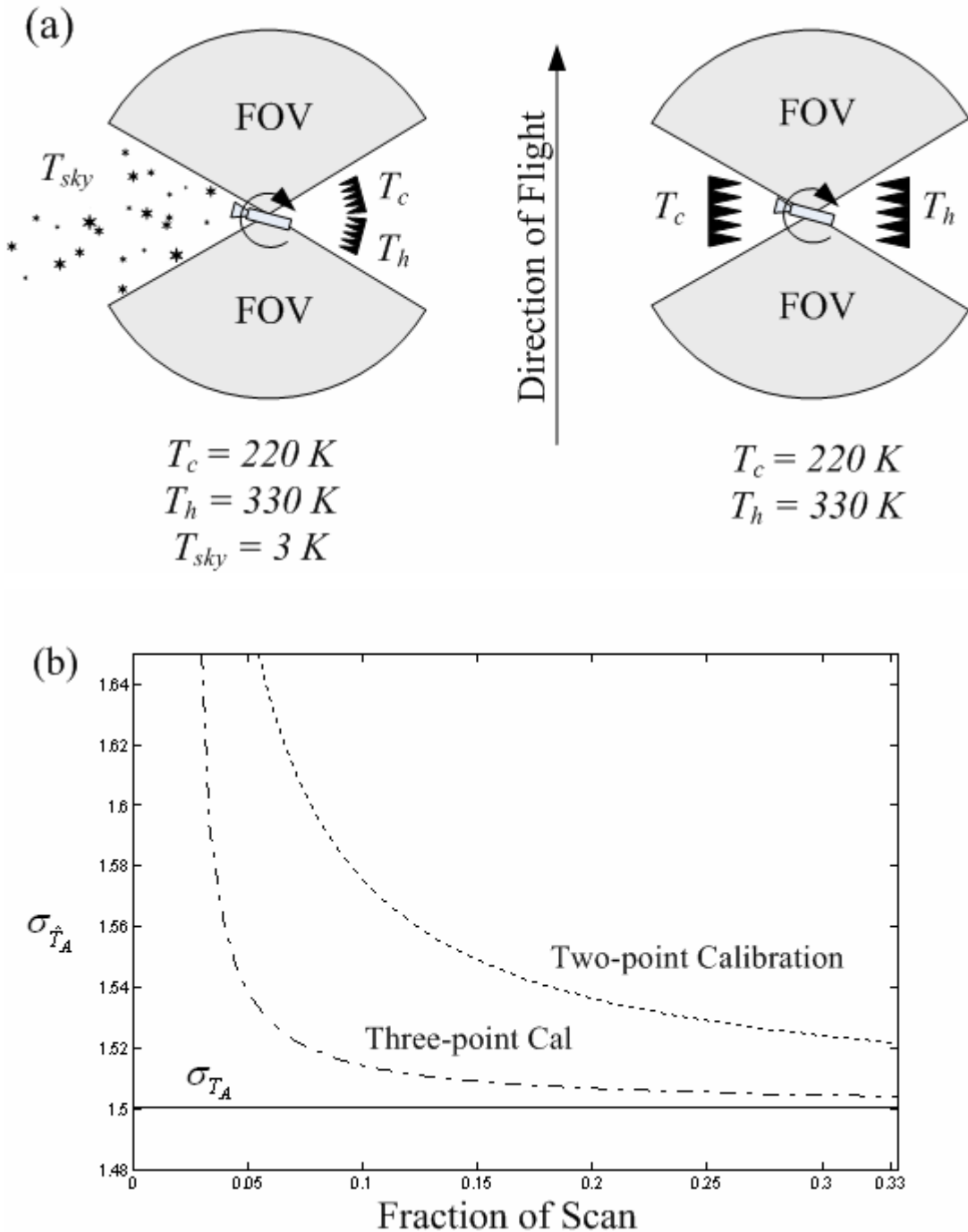


Figure 18: Comparison of a two-point and three-point calibration architecture. (a) Two configurations considered for the calibration of a conical-scanning spaceborne sensor. Science requires a minimum 120° field of view (FOV) in the foreword and aft directions of the flight track. On the left hand side, a three-point calibration is shown which includes observation of the cold sky. On the right hand side, a two point calibration is shown. (b) A plot showing the comparison of measurement uncertainty as a function of the fraction of scan allocated to calibration for the two configurations. For reference, the solid line shows the resolution of the measurand. See text for discussion of parameters used in the calculations.

the center rotates at \sim 30 rpm and the integration time per pixel is 2.75 ms; the rotation rate and pixel integration time are based upon contiguous coverage for the required spatial resolution and selected orbit. On the left hand side is the configuration for the three-point calibration. On one side of the scan are two blackbody references; one blackbody is heated to 330 K and the other body is passively cooled to 220 K. On the other side of the scan the instrument design accommodates a cold-sky view to space. Because the space view might be obscured by the satellite bus, a two-point calibration is also considered as shown in Fig. 18a on the right hand side. A fraction of the scan cycle is lost to latency as the beam patterns move on and off the calibration references; latency is assumed to be \sim 2.2% of the scan and the same for both configurations. A comparison of these two configurations is made for a measurand temperature of 150 K (the nominal value of cold TB's anticipated for the frequencies considered); a bandwidth $B = 1.6$ GHz and $T_{rec} = 3000$ K where used with (3.22) for the calculations; uncertainty in the knowledge of the reference temperatures ($\sigma_{\bar{T}_i}$) was assumed zero. Results of the comparisons are shown in Fig. 18b where the measurement uncertainty is plotted as a function of the fraction of scan allocated to calibration. The fraction 0.33 corresponds to 120° of the scan (60° per side) allocated to calibration and includes the latency. Clearly, the three point calibration offers an advantage since it yields the lowest measurement uncertainty, although not by much. At a fraction of 0.33, the two-point calibration is only \sim 1.3% higher than the three point calibration. One might be surprised that extrapolating the two-point calibration would yield results close to that of the three-point calibration. However, the increased integration time due to the two targets subtending a larger fraction of the scan helps reduce the effect of extrapolation of the data thus yielding performance comparable to the three point calibration.

Studies like this one have practical application in designing radiometers by quantifying the performance that can be achieved using different calibration architectures. In this study, the effect of eliminating the space view has been quantified; and should the final satellite configuration require the elimination of the space view, the effect on the instrument's measurements has been quantified. Furthermore, analyses like this can be used to establish requirements for the thermal control of the blackbody references.

4.7 Noise Source Injection and Tier 3 Calibration

In this section a radiometer is analyzed that utilizes calibration references from all three tiers. The radiometer uses a noise source (tier 1) to inject noise into the measurement path. The antenna switches between observing the measurand (the scene) and observing an internal blackbody (tier 2). External calibration measurements (tier 3) are then used to derive and estimate the value of the additive noise temperature. Noise injection during observation of the measurand prevents application of the LSR as was used in Section 4.1. Therefore, the general form of calculating measurement uncertainty that is presented in Section 3.3 is used for the analysis. In Section 4.2.1, an internal calibration algorithm is analyzed and optimized for a given set of parameters. In Section 4.2.2, measurement uncertainty is used to study approaches for external calibration.

4.7.1 Internal Calibration

Figure 19a shows a block diagram of the radiometer being considered. Internal calibration (tier 1 and tier 2) of the radiometer is achieved by using a noise source to add noise to observations of the measurand and an internal blackbody reference. The receiver bandwidth is $B = 1\text{GHz}$ and the receiver noise temperature is $T_{rec} = 500\text{K}$. The loss in the antenna and switching mechanism are modeled using a single loss term, $L_1 = 0.5\text{ dB}$; the effective temperature of the loss is $T_{L_1} = 290\text{ K}$. Through the antenna, observations are made of the blackbody which is at temperature $T_r = 300\text{ K}$. The noise source is switched on and off during observations of the measurand and the blackbody reference, thus, yielding four distinct total-power measurement states. The radiometer is decomposed into a set of four subsystems, one for each state, and each subsystem is characterized by one of the following equations:

$$\text{measurand} \quad v_A = (T_A L_1 + (1 - L_1) T_{L_1} + T_{rec}) \mu \quad (4.4a)$$

$$\text{measurand plus noise} \quad v_{A_n} = (T_A L_1 + (1 - L_1) T_{L_1} + T_n + T_{rec}) \mu \quad (4.4b)$$

$$\text{reference} \quad v_r = (T_r L_1 + (1 - L_1) T_{L_1} + T_{rec}) \mu \quad (4.4c)$$

$$\text{reference plus noise} \quad v_{r_n} = (T_A L_1 + (1 - L_1) T_{L_1} + T_n + T_{rec}) \mu \quad (4.4d)$$

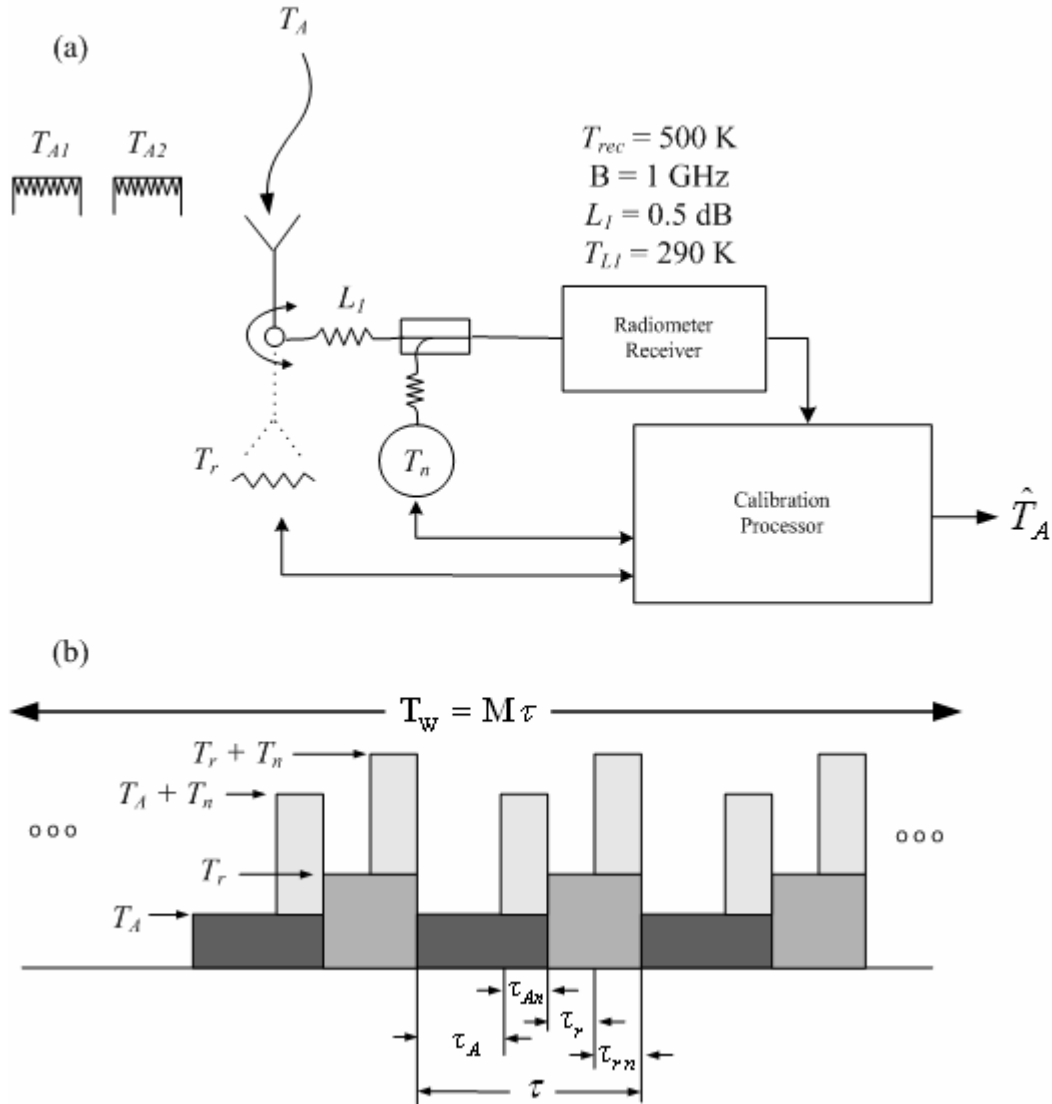


Figure 19: Diagram of a radiometer system which utilizes three tiers to achieve calibration. (a) The radiometer model includes additive noise source injection, front-end loss and through-the-antenna calibration. (b) Timing diagram of the internal calibration sequence. A complete cycle consists of observations of the measurand (T_A), measurand plus noise ($T_A + T_n$), blackbody reference (T_r), and blackbody reference plus noise ($T_r + T_n$).

where μ is the receiver gain, T_n is the additive noise temperature, and the subscripts on the voltages indicate the radiometer state. The additive noise during the observation of the measurand prevents expressing the set of characteristic equations in the form of (3.14). Thus, the LSR estimator given by (3.21) and the estimator uncertainty given by (3.22) can not be applied to this design. Nevertheless, there are a variety of other ways to form an estimator from the set of equations. In the following, one approach for obtaining an internal calibration estimator is considered. The estimator is formed by using (4.4c) and (4.4d) to solve for T_{rec} and μ from which the result for T_{rec} is then substituted into (4.4a) and (4.4b). An estimate of T_A is then obtained by solving (4.4a) and (4.4b) for μ and T_A , thus yielding,

$$\hat{T}_A = \frac{v_A v_{rn} T_n - v_r v_{An} T_n - v_{rn} v_A T_r L_1 + v_{rn} v_{An} T_r L_1 + v_r v_A T_r L_1 - v_r v_a T_r L_1 - v_r v_{An} T_r L_1}{(v_A - v_{An})(v_r - v_{rn})L_1}. \quad (4.5)$$

The estimator does not include μ , T_{rec} , or T_{L_1} ; these parameters have been removed from the estimator through the calibration process. (Note that the contribution of $(1 - L_1)T_{L_1}$ appears as an increase in the receiver noise temperature.) It is convenient to define the equivalent noise source temperature, $T_{np} = T_n L_1^{-1}$. By doing so, the calibration of T_n and L_1 is combined into a single value. Upon substituting $T_n = L_1 T_{np}$ into (4.5),

$$\begin{aligned} \hat{T}_A &= \frac{v_A v_{rn} T_{np} - v_r v_{An} T_{np} - v_{rn} v_A T_r + v_{rn} v_{An} T_r + v_r v_A T_r - v_r v_a T_r - v_r v_{An} T_r}{(v_A - v_{An})(v_r - v_{rn})} \\ &= f_{T_A}^i(v_A, v_{An}, v_r, v_{rn}, T_r, T_{np}) \end{aligned} \quad (4.6)$$

where the internal calibration estimator is expressed as a function, $f_{T_A}^i$, with six variables.

A timing diagram of the measurement cycle is shown in Fig. 19b. The total cycle period is divided between the four states and the time to complete one cycle is τ . Latency is assumed negligible and so the total cycle period is the sum of the integration times of the four measurement states, i.e. $\tau = \tau_A + \tau_{An} + \tau_r + \tau_{rn}$. The fraction of time that the noise source injects noise is d_n . The fraction of the cycle period allocated to observing the measurand and measurand plus noise is d_A . The following set of equations gives the integration times for each of the four states:

$$\tau_A = \tau d_A d_n \quad (4.7a)$$

$$\tau_{A_n} = \tau d_A (1 - d_n) \quad (4.7b)$$

$$\tau_r = \tau (1 - d_A) d_n \quad (4.7c)$$

$$\tau_{r_n} = \tau (1 - d_A) (1 - d_n). \quad (4.7d)$$

For the calculations presented below, $d_n = 0.5$ and $\tau = 1\text{ s}$. Reference averaging is applied to the blackbody and blackbody plus noise observations. Over an interval of $T_w = M\tau$, M samples of v_r and v_{rn} are averaged; the average of the voltage measurements are $\langle v_r \rangle_M$ and $\langle v_{rn} \rangle_M$, respectively. These averages are used in place of v_r and v_{rn} in (4.6). By averaging, the fluctuation in the voltage measurements are reduced by $M^{-0.5}$. The improvement on the measurement estimate is examined in Fig. 20a and is discussed below.

The measurement uncertainty of the internal calibration estimator, $f_{T_A}^i$, is calculated by inserting (4.6) into (3.13). Matlab® and its Symbolic Math Toolbox are used for the calculation. The program for deriving the analytical form for the measurement uncertainty is given in Appendix C. The partial derivatives are calculated with respect to each parameter in (4.6). The uncertainties in the voltages due to stochastic fluctuations of the noise signals are calculated using

$$\sigma_{v_A} = \mu (T_A L_1 + (1 - L_1) T_{L_1} + T_{rec}) (B \tau_A)^{-0.5} \quad (4.8a)$$

$$\sigma_{v_{An}} = \mu (T_A L_1 + (1 - L_1) T_{L_1} + T_n + T_{rec}) (B \tau_{An})^{-0.5} \quad (4.8b)$$

$$\sigma_{v_r} = \mu (T_r L_1 + (1 - L_1) T_{L_1} + T_{rec}) (B \tau_r)^{-0.5} \quad (4.8c)$$

$$\sigma_{v_{rn}} = \mu (T_r L_1 + (1 - L_1) T_{L_1} + T_n + T_{rec}) (B \tau_{rn})^{-0.5}. \quad (4.8d)$$

It should be noted that the system gain, μ , cancels out of the expression for uncertainty and thus it's value is arbitrary. The uncertainty in the knowledge of T_r and T_{np} are assumed to be $\sigma_{\bar{T}_r} = 0.2\text{ K}$ and $\sigma_{\bar{T}_{np}} = 1\text{ K}$, respectively. (In Section 4.2.2, external calibration is used to estimate T_{np} and the uncertainty in the estimate (\hat{T}_{np}) and its influence on \hat{T}_A is examined.)

Table 1: Description of the parameters and symbols used in the analysis of noise injection radiometer with external calibration (analysis presented in Section 4.2).

Parameter	Comment
T_A	Measurand.
\hat{T}_A	Estimator of the measurand.
$\sigma_{\hat{T}_A}$	Uncertainty in estimator, calculated using (3.13).
B	Receiver pre-detection bandwidth, $B = 1$ GHz.
μ	System gain, $\mu = 1$ Volts/Kelvin
T_{rec}	Receiver noise temperature, $T_{rec} = 500$ K.
v_A	Measurand voltage.
σ_{v_A}	Uncertainty in v_A . See (4.8a).
v_{An}	Measurand + noise voltage.
$\sigma_{v_{An}}$	Uncertainty in v_{An} . See (4.8b).
v_r	Blackbody reference voltage.
σ_{v_r}	Uncertainty in v_r . See (4.8c).
v_{rn}	Measurand + noise voltage. See (4.8d).
$\sigma_{v_{rn}}$	Uncertainty in v_{rn} .
$\langle v_r \rangle_M$	Averaged blackbody reference voltage.
$\sigma_{v_r} M^{-0.5}$	Uncertainty in averaged blackbody reference voltage.
$\langle v_{rn} \rangle_M$	Averaged measurand + noise voltage.
$\sigma_{v_{rn}} M^{-0.5}$	Uncertainty in averaged blackbody + noise reference voltage.
M	Number of cycles used for reference averaging. Total averaging period is $T_W = M\tau$. $M = 30$ except in Fig. 20.
T_n	Noise source temperature. $T_n = 500$ K.

Table 1: Continued.

Parameter	Comment
T_{n_p}	Equivalent noise source temperature, $T_{n_p} = T_n L_1^{-1}$. In Fig. 20,
$\sigma_{\bar{T}_{n_p}}$	$\sigma_{\bar{T}_{n_p}} = 1 \text{ K}$, otherwise, for external calibration $\sigma_{\bar{T}_{n_p}}$ is calculated.
T_r	Blackbody reference temperature. $T_r = 300 \text{ K}$,
$\sigma_{\bar{T}_r}$	$\sigma_{\bar{T}_r} = 0.2 \text{ K}$
L_1	Front end losses, $L_1 = 0.5 \text{ dB}$.
T_{L_1}	Front end loss temperature, $T_{L_1} = 290 \text{ K}$.
τ	Total cycle period. $\tau = \tau_A + \tau_{An} + \tau_r + \tau_{rn} = 1 \text{ s}$
d_n	Fraction of total cycle with noise injection. Throughout study $d_n = 0.5$.
d_A	Fraction of time observing measurand or measurand + noise. $d_A = 0.8$ except in Fig. 20.
τ_A	Measurand integration time. See (4.7a).
τ_{An}	Noise + meaurand integration time. See (4.7b).
τ_r	Reference integration time. See (4.7c).
τ_{rn}	Noise + reference integration time. See (4.7d).
T_{A1}	External reference temperature. $T_{A1} = 330 \text{ K}$.
$\sigma_{\bar{T}_{A1}}$	Uncertainty in knowledge of T_{A1} , $\sigma_{\bar{T}_{A1}} = 0.2 \text{ K}$.
T_{A2}	External reference temperature.
$\sigma_{\bar{T}_{A2}}$	Uncertainty in knowledge of T_{A2} , $\sigma_{\bar{T}_{A2}} = 0.2 \text{ K}$ except in Fig. 22(a)

Figure 20a shows a composite of curves that illustrate the relationship of the duty cycle, d_A , the averaging window, T_w , and the measurement uncertainty, $\sigma_{\hat{T}_A}$. A summary of the values used in the calculations is given in Table 1. The uncertainty rapidly decreases with reference averaging (increasing T_w) but flattens for values of $T_w > 20$ s. As more reference measurements are averaged, the optimal duty cycle changes. Two curves from Fig. 20a are shown in Fig. 20b where the uncertainty is plotted as a function of duty cycle for $T_w = 1$ s and $T_w = 30$ s. The dashed line shows how the minimum uncertainty varies with the duty cycle as a function of T_w . Based on these calculations, the internal calibration algorithm is chosen to have $d_A = 0.8$ and $T_w = 30$ s. These values are used in the next section which investigates the effect of external calibration parameters on the measurement estimate.

4.7.2 External Calibration

In this section, external calibration measurements are used to obtain an estimate for T_{np} ; the estimate is then used as part of the estimator for T_A given by (4.6). A development is shown that can be applied for an arbitrary number of calibration measurements; a case where two measurements are used is then examined in more detail. The effect of the external calibration reference temperature is first considered. Then the effect of uncertainty in the knowledge of the calibration reference temperatures on measurement uncertainty is examined.

Recall from the previous section that by defining $T_{np} = T_n L_1^{-1}$ the parameters T_n and L_1 are combined, whereby, using external calibration measurements their combined effect is calibrated by the single estimator, \hat{T}_{np} . A number K of external (tier 3) calibration measurements are used to estimate the equivalent noise diode temperature, \hat{T}_{np} . The estimate of T_{np} is obtained by minimizing the mean square error of measurements, i.e. by solving

$$0 = \frac{\partial}{\partial T_{np}} \sum_{k=1}^K \left(T_{Ak} - f_{T_A}^i(v_{Ak}, v_{Ak,n}, v_{rk}, v_{rk,n}, T_r, T_{np}) \right)^2 \quad (4.9)$$

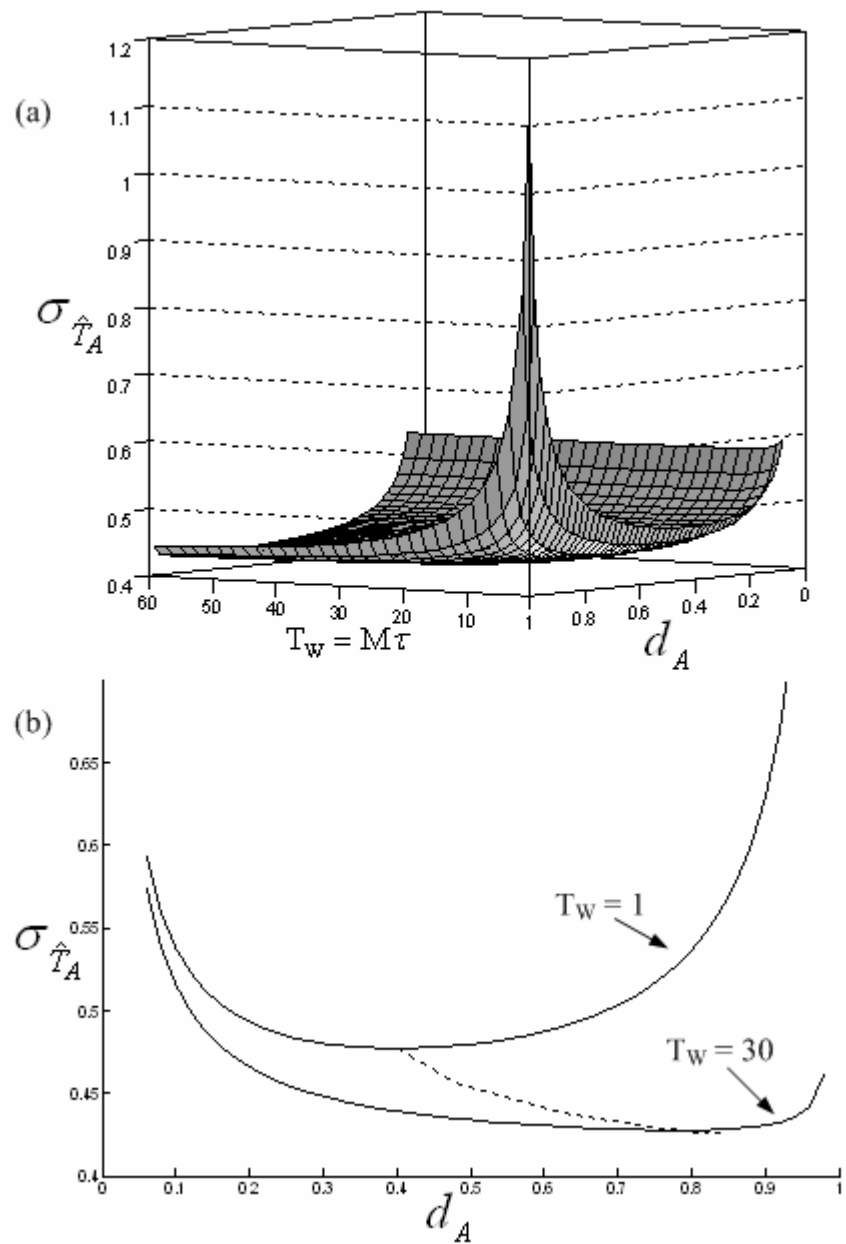


Figure 20: Measurement uncertainty as a function of averaging window width and duty cycle. (a) Composite of curves showing how measurement uncertainty varies as a function of the fraction of time spent observing the measurand (d_A) and the number of reference observations averaged (N). (b) Detail showing measurement uncertainty for two curves, $N = 1$ and $N = 30$. The dashed line is the minimum uncertainty calculated from the family of curves shown in (a).

where T_{Ak} is the brightness temperature of the k^{th} external calibration reference temperature, and $f_{T_A}^i(v_{Ak}, v_{Ak\,n}, v_{rk}, v_{rk\,n}, T_r, T_{np})$ is the internal calibration estimator for \hat{T}_{Ak} given by (4.6); the voltage measurements $v_{Ak}, v_{Ak\,n}, v_{rk},$ and $v_{rk\,n}$ correspond to the observations of the external references. The statistics of the voltages $v_{rk},$ and $v_{rk\,n}$ depend on the duration of the calibration observations and so they are maintained as distinct variables in the equations. Note that since (4.6) is a linear function of T_{np} and all other parameters are known, a single calibration measurement could be used to estimate its value. Nevertheless, in the following two external calibration measurements are used to estimate its value. Solving (4.9), for $K = 2,$ the noise source estimator becomes

$$\hat{T}_{np} = f_{T_{np}}^e(v_{A1}, v_{A2\,n}, v_{r1}, v_{r2\,n}, v_{A1}, v_{A2\,n}, v_{r1}, v_{r2\,n}, T_r, T_{A1}, T_{A2}). \quad (4.10)$$

The uncertainty in \hat{T}_{np} can be found by substituting (4.10) into (3.13). The measurand estimator then becomes

$$\begin{aligned} \hat{T}_A &= f_{T_A}^i(v_A, v_{An}, v_r, v_{rn}, T_r, \hat{T}_{np}) \\ &= f_{T_A}^e(v_A, v_{An}, v_r, v_{rn}, v_{A1}, v_{A1\,n}, v_{r1}, v_{r1\,n}, v_{A1}, v_{A2\,n}, v_{r1}, v_{r2\,n}, T_r, T_{A1}, T_{A2}) \end{aligned} \quad (4.11)$$

The measurement uncertainty associated with $f_{T_A}^e$ is calculated by inserting (4.11) into (3.13); the calculation of the uncertainty includes the uncertainty associated with each variable in (4.11). Again, Matlab® and its Symbolic Math Toolbox are used to obtain an analytical form of the solution; the calculation could also be performed numerically. The symbolic expressions for (4.10) and (4.11) are very lengthy and are not included herein. However, the Matlab® code to generate (4.6), (4.10), (4.11) and their respective uncertainties is given in Appendix C.

The uncertainties for \hat{T}_{np} and \hat{T}_A including the two-point external calibration are shown in Fig. 21 as a function of the external reference temperatures. The measurand temperature is assumed to be $T_A = 100\text{ K};$ other values used in for the calculations are summarized in Table 1. One external reference temperature is held constant, $T_{A1} = 330\text{ K}$ while the other is allowed to vary. The bottom abscissa shows the temperature of the second calibration reference, $T_{A2};$ the top abscissa shows the difference, $T_{A2} - T_{A1}.$ Contributing factors to the uncertainty in the knowledge of the external reference apparent brightness temperature include: uncertainty in the

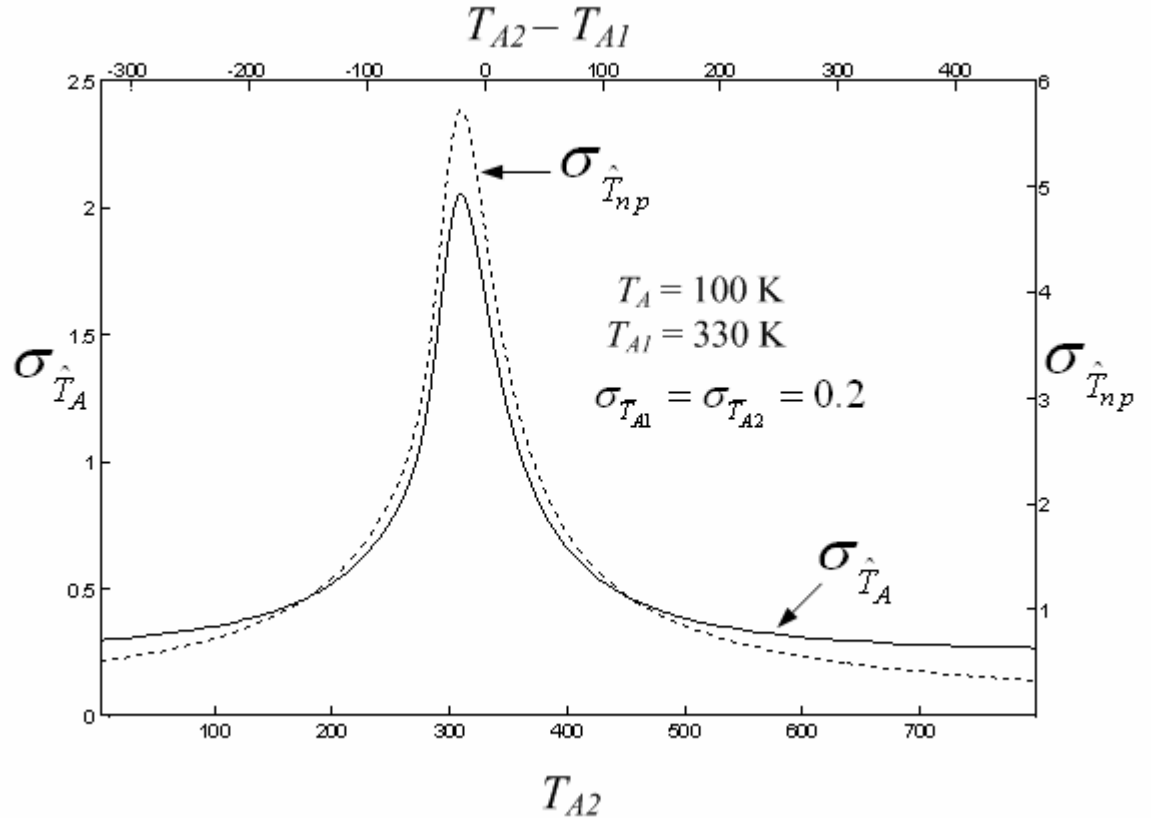


Figure 21: Measurement uncertainty for a two-point external calibration for the calibration algorithm described in 4.2.2. Shown are the uncertainties in the estimates of T_A (solid) and T_{n_p} (dashed). One calibration reference, T_{A1} is held constant at 330 K. The measurement uncertainty is shown as a function of the second calibration reference temperature T_{A2} . The bottom abscissa shows T_{A2} and the top abscissa shows the difference in calibration reference temperatures. The measurand temperature is $T_A = 100$. The uncertainty in the knowledge of each calibration reference temperature is $\sigma_{\bar{T}_{A1}} = \sigma_{\bar{T}_{A2}} = 0.2$.

reference temperatures would need to be separated by more than 100 K, i.e. $|T_{A2} - T_{A1}| > 100 \text{ K}$. The uncertainty increases as $|T_{A2} - T_{A1}|$ becomes smaller than 100 K as a result of extrapolating the calibration data to estimate T_{n_p} . If the radiometer did not use the internal blackbody ($T_r = 300 \text{ K}$) for calibration, the uncertainty in \hat{T}_{n_p} would be unbounded for $T_{A2} = T_{A1}$. The use of the internal blackbody essentially makes the estimate of T_{n_p} based on a three point calibration; hence, the peak of the uncertainty occurs for $T_r < T_{A1} < T_{A2}$ with $T_{A2} \approx 310 \text{ K}$.

Often times when a cold (or hot) calibration reference is used the uncertainty in the knowledge of its brightness temperature can be greater than when using a target that is closer to ambient temperature. The amplitude of the standing wave between the radiometer and blackbody can have greater amplitude due to the larger contrast in target temperature and emission from the radiometer antenna; also errors due to temperature gradients and to temperature sensor measurements can be greater. If the sky is used as a calibration reference, uncertainty due to atmospheric contributions and antenna side lobes can vary depending upon the level of effort applied to improving the measurement model. For these reasons, it is of interest to characterize the measurement uncertainty as a function of the uncertainty in the knowledge of an external calibration reference.

In Fig. 22a, $\sigma_{\hat{T}_A}$ is shown as a function of the uncertainty in the knowledge of the calibration reference brightness temperature ($\sigma_{\bar{T}_{A2}}$) for $T_{A2} = 290 \text{ K}$ and $T_{A2} = 80 \text{ K}$; these values correspond roughly to a room temperature reference and a blackbody immersed in liquid nitrogen. Again, $T_{A1} = 330 \text{ K}$, $\sigma_{\bar{T}_{A1}} = 0.2 \text{ K}$, and $T_A = 100 \text{ K}$ are used in the calculations. The same parametric values for the radiometer are used that were used in Fig. 21 and are given in Table 1. For $T_{A2} = 80 \text{ K}$ and $\sigma_{\bar{T}_{A2}} = 2 \text{ K}$, the uncertainty in the measurand estimate is $\sigma_{\hat{T}_A} = 1.8 \text{ K}$; to achieve the same level of calibration performance from using a reference at $T_{A2} = 290 \text{ K}$, the uncertainty in T_{A2} would have to be $\sigma_{\bar{T}_{A2}} \leq 0.5 \text{ K}$. For perfect knowledge of T_{A2} ($\sigma_{\bar{T}_{A2}} = 0$), the uncertainty in \hat{T}_A can not be better than $\sigma_{\hat{T}_A} \approx 1.5 \text{ K}$ whereas much better performance can be achieved using the colder reference provided its uncertainty can be reduced below 1.5 K. In Fig. 22b the uncertainty as a function of T_A is plotted for $\sigma_{\bar{T}_{A2}} = 1.0 \text{ K}$ for the

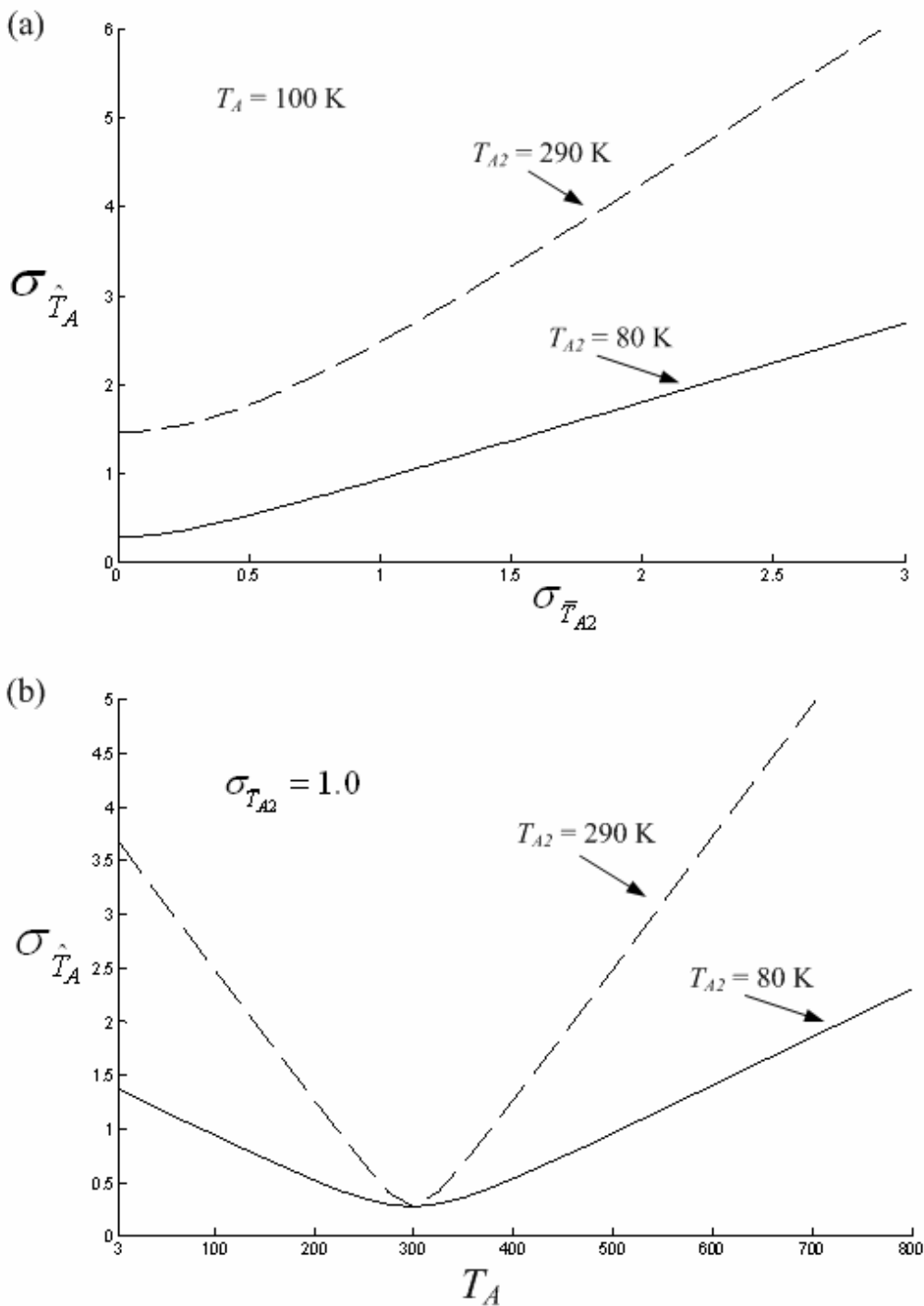


Figure 22: Plot of the measurement uncertainty comparing two calibration scenarios. (a) shows how measurement uncertainty varies as a function of the uncertainty in knowledge of the calibration reference temperature for $T_A = 100$. (b) Shows how the measurement uncertainty varies as a function of T_A .

two cases, $T_{A2} = 290\text{ K}$ and $T_{A2} = 80\text{ K}$. The effect of the extrapolation of the calibration is readily apparent for the case $T_{A2} = 290\text{ K}$. The uncertainty of both curves is minimum at $T_A \approx 300\text{ K}$, the minimum corresponds to the observation of the internal blackbody.

4.8 Summary

In this chapter, measurement uncertainty has been used to quantify the performance of various calibration schemes. The LSR framework developed in Section 3.3 was used to study the effect of calibration reference temperature, fraction of time allocated to calibration, number of calibration references, as well as reference averaging and the application of weights to calibration measurements. The measurement uncertainty for a radiometer that uses noise source injection and external (tier-3) references for calibration was also evaluated; the effect of the external calibration temperatures as well as uncertainty in their knowledge on the estimate of the equivalent noise source temperature was also evaluated. The analysis presented all relied on the assumption that the fluctuations in the receiver were stationary and negligible. In Chapter 5 comparisons of model calculations are made with data collected during a calibration experiment.

CHAPTER 5

COMPARISONS WITH MEASUREMENTS

5.1 Introduction

In Chapter 3 a model based on treating samples of the radiometer output as random variables was developed for predicting the performance of a variety of calibration architectures and algorithms. In Chapter 4 the measurement uncertainty for a variety of calibration architectures and algorithms was evaluated. In this chapter, model predictions are compared with data collected during a calibration experiment that was conducted to study the influence of calibration algorithms on measurement uncertainty. Three different calibration algorithms are applied to the data and the results are compared to model calculations.

5.2 The MIR 2002 Calibration Experiment

During September 2002 the MIR Calibration Experiment (CalEx02) was conducted. The purpose of the experiment was to validate predictions of radiometer calibration performance that have been presented in Chapter 4 and predictions based on models of nonstationary receiver fluctuations (not shown in this dissertation). The experiment was conducted over two days. The MIR with its two internal blackbodies was used to observe a third stable temperature reference for extended periods of time. A custom designed cryogenically cooled blackbody reference (CryoTarget) was used as the third stable temperature reference. Figure 23a shows a photograph of the MIR during CalEx02 while it was positioned over the CryoTarget collecting data. Figure 23b shows a photograph of the CryoTarget and the blackbody inside. Figure 23c shows a cross-section of the CryoTarget design. A tank used to hold liquid nitrogen (LN2) envelops the blackbody, thereby, enabling the observation of the cooled reference without LN2 in the measurement path. The CryoTarget temperature is measured by five temperature sensors that are embedded inside the blackbody.

The MIR scan profile was modified to observe its two internal blackbody references and the CryoTarget for $\tau_p = 0.2\text{ s}$ each. Including latency, the complete scan cycle time was 1.16 s. The CryoTarget temperature sensors were sampled once every $\sim 6\text{ s}$; the five sensors were averaged to yield a single temperature time series. In post-processing of the data the calibration

voltage and temperature data and the radiometer CryoTarget voltage (C_v) and temperature (C_T) data were all resampled to be on the same 1.16-s time scale.

Two sets of measurements were collected. During the first set of measurements (denoted as T295) the CryoTarget was at ambient-laboratory temperature and observations were made over \sim 23 hour time period; during the second measurement set (denoted as T80) the CryoTarget was cooled using LN2 and observations were made over \sim 6 hour time period. After the experiment problems with the data were discovered. All seven radiometer channels exhibited moderate to severe degradation in data quality; five of the seven channels of data were unusable. Examination of the data led to the conclusion that the problem stemmed from the data digitization electronics. (To this date, these problems with the MIR have not been resolved.) The 89 GHz and 340 GHz channels appeared least affected by the problem. For the most part, the data were uncorrupted throughout the experiment although the short-term variance of the data (calculated from time series less than 10 seconds duration) was much higher than usual. Because of the excess noise produced by the digital electronics, estimates of the apparent receiver noise temperature were made by looking at the short-term variance of the data. Estimates for T_{rec} are: 1800 K and 12000 K for the 89 GHz and 340 GHz channels, respectively; these values are \sim 3 – 4 times higher than normal for these channels. The 89 GHz channel has a 1 GHz bandwidth pre-detection filter; the 340 GHz doesn't have a pre-detection filter but the pre-detection bandwidth is limited by the IF amplifier which has \sim 5 GHz bandwidth. These bandwidths, receiver noise temperatures, and integration times ($\tau_p = 0.2\text{s}$) are used in the model calculations in the comparisons that follow.

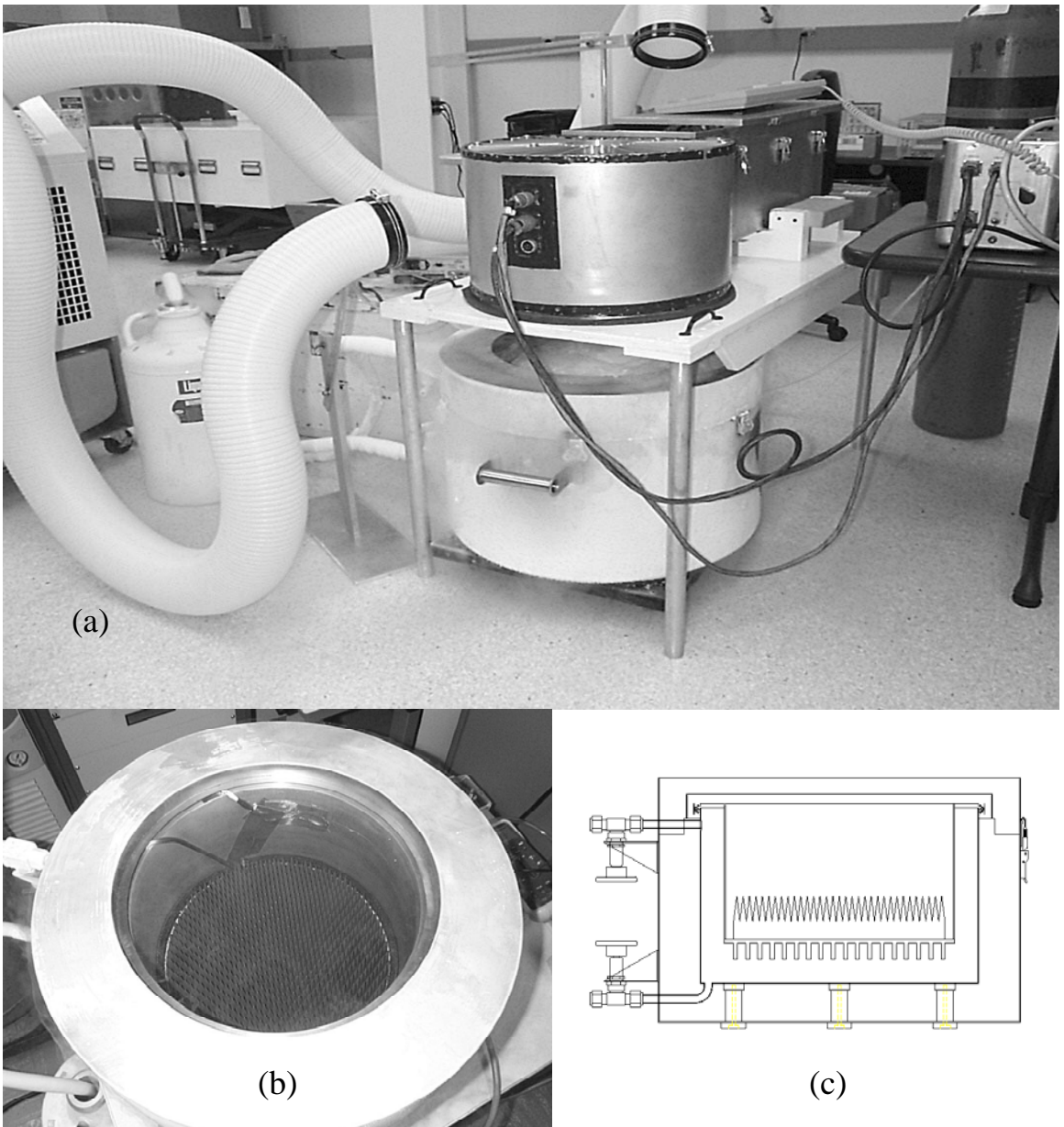


Figure 23: Photograph of MIR during CalEx02. (a) The MIR is positioned over the cryogenic calibration reference (CryoTarget) while it was cooled by liquid nitrogen. Air-conditioning tubes blow cool air over the instrument to keep it thermally stable. (b) Photograph showing the interior of the CryoTarget. (c) Drawing showing the cross-section of the CryoTarget design. Liquid nitrogen fills the tank enveloping the blackbody.

The data used in the subsequent analyses are shown in Fig. 24. Figures 24a,b,c show data from the T295 experiment. A six-hour period is shown. Figure 24a shows the radiometer data from the 89 GHz hot and cold measurements plotted in digital count value; Fig. 24b shows the 340 GHz calibration data. Fig. 24c show the 89 GHz and 340 GHz radiometer data from the CryoTarget observations; the averages of the time series have been subtracted from these data. Plots of the temperature data from the three references are not shown. During the T295 run the mean and standard deviation of the hot and cold calibration temperatures are $T_h = 325.20 \pm 0.009$ K and $T_c = 292.44 \pm 0.069$ K, respectively. The cold reference temperature has a higher standard deviation because it does not have active thermal control. The low standard deviations demonstrate that the internal references were very stable over the six hour period. The mean and standard deviation of the CryoTarget for this period is $C_T = 295.85 \pm 0.061$ K; the temperature exhibited a peak-to-peak variation of 0.212 K and has a nearly linear warming trend over the 6 hour period. Figures 24d,e,f show data from the ~6 hour T80 measurement set. The hot and cold radiometer measurements from the 89 GHz and 340 GHz radiometers are shown in Figs. 24d and 24e, respectively. Figure 24f shows the 89 GHz and 340 GHz radiometer data from the CryoTarget observations, again with the means subtracted. For the T80 dataset, the mean and standard deviation of the hot and cold calibration reference temperatures are $T_h = 325.59$ K ± 0.014 K and $T_c = 293.69 \pm 0.10$ K, respectively. The mean and standard deviation of the CryoTarget temperature over the six-hour period is $C_T = 79.02 \pm 0.043$ K. The CryoTarget temperature increases to a peak during the first hour and then monotonically decreases for the rest of the period and has a maximum peak-to-peak variation of 0.15 K over the ~6 hour period.

In the following calculations, the goal is to assess the contribution of the calibration algorithm to the noise in the measurement estimate. To this end, biases that may exist in the calibration are not considered in the analysis. The approach is to apply a calibration algorithm to the data to estimate the temperature of the CryoTarget; the standard deviation of the estimated temperature time series ($\hat{\sigma}_{\hat{T}_A}$) is then used as a measure of the uncertainty including the contribution of the calibration algorithm. To minimize the contribution of the CyroTarget

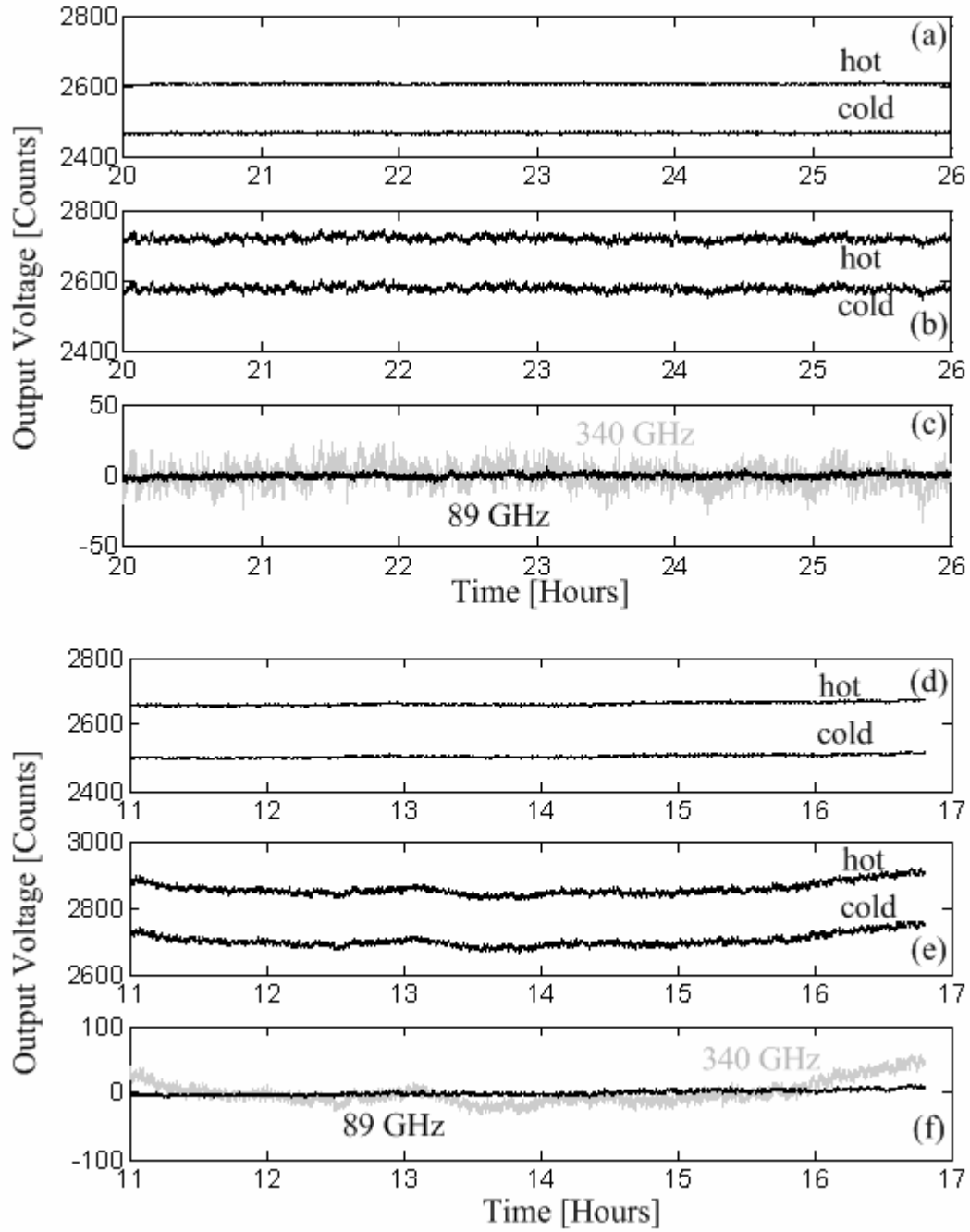


Figure 24: Time series of MIR data collected during CalEx02. (a) – (c) Measurements made viewing the CryoTarget at ~ 295 K, (d) – (f) measurements made viewing the CryoTarget at ~ 80 K, (a,d) 89 GHz hot and cold count values, (b,e) 340 GHz hot and cold count values, (c,f) 89 GHz and 340 GHz target counts with means removed. The 340 GHz data appear more noisy.

temperature fluctuations from the calculation of the standard deviation, the temperature fluctuations were removed from the radiometer data using the formula

$$C_v^c(t) = C_v(t) - (C_T(t) - \langle C_T \rangle) \langle m \rangle^{-1} \quad (5.1)$$

where $C_v^c(t)$ is the corrected radiometer voltage, $\langle C_T \rangle$ is the mean temperature of the CryoTarget and $\langle m \rangle$ is the mean system slope calculated over the measurement set period. Although quite small, the temperature fluctuations were removed from both the T295 and T80 data sets.

5.3 Three Calibration Algorithms

Three different calibration algorithms were applied to the T295 and T80 data sets. The first algorithm is considered an “instantaneous” calibration algorithm and is denoted (1u). A single hot and cold radiometer calibration measurement and temperature pair were used to calculate the radiometer slope and offset; the slope and offset are then applied to calculating the CryoTarget temperature estimate for the same time. (Recall the data are on a common 1.16-s time grid.) The calculations are repeated for the entire time series. For the second and third algorithms, the unweighted LMS algorithm (see (3.21)) was applied to the calibration data over ~5 s and ~30 s intervals; these two algorithms are denoted u5 and u30. For u30, 15 calibration data points ahead, 14 calibration data points behind, plus the one at the time of the measurement are used to form the estimate.

Figure 25 shows the time series of the CryoTarget temperature estimates made using the 30u and 1u algorithms. The standard deviations of the time series are shown on the plots. Figure 32a shows the results for T295 data set for the 89 GHz using the 30u and 1u algorithms. The standard deviation for the 1u and 30u algorithms are $\hat{\sigma}_{\hat{T}_A}(1u) = 0.209 \text{ K}$ and $\hat{\sigma}_{\hat{T}_A}(30u) = 0.209 \text{ K}$; no difference is observed between the performance of the two algorithms.

Figure 25b shows the results for the T80 set for the 89 GHz; the standard deviation for the 1u and 30u algorithms are $\hat{\sigma}_{\hat{T}_A}(1u) = 1.502 \text{ K}$ and $\hat{\sigma}_{\hat{T}_A}(30u) = 0.373 \text{ K}$. In this case, improvement of the 30u algorithm over the 1u algorithm is readily seen in the time series and the corresponding standard deviation values. Figures 25c and 25d show the results for the 340 GHz.

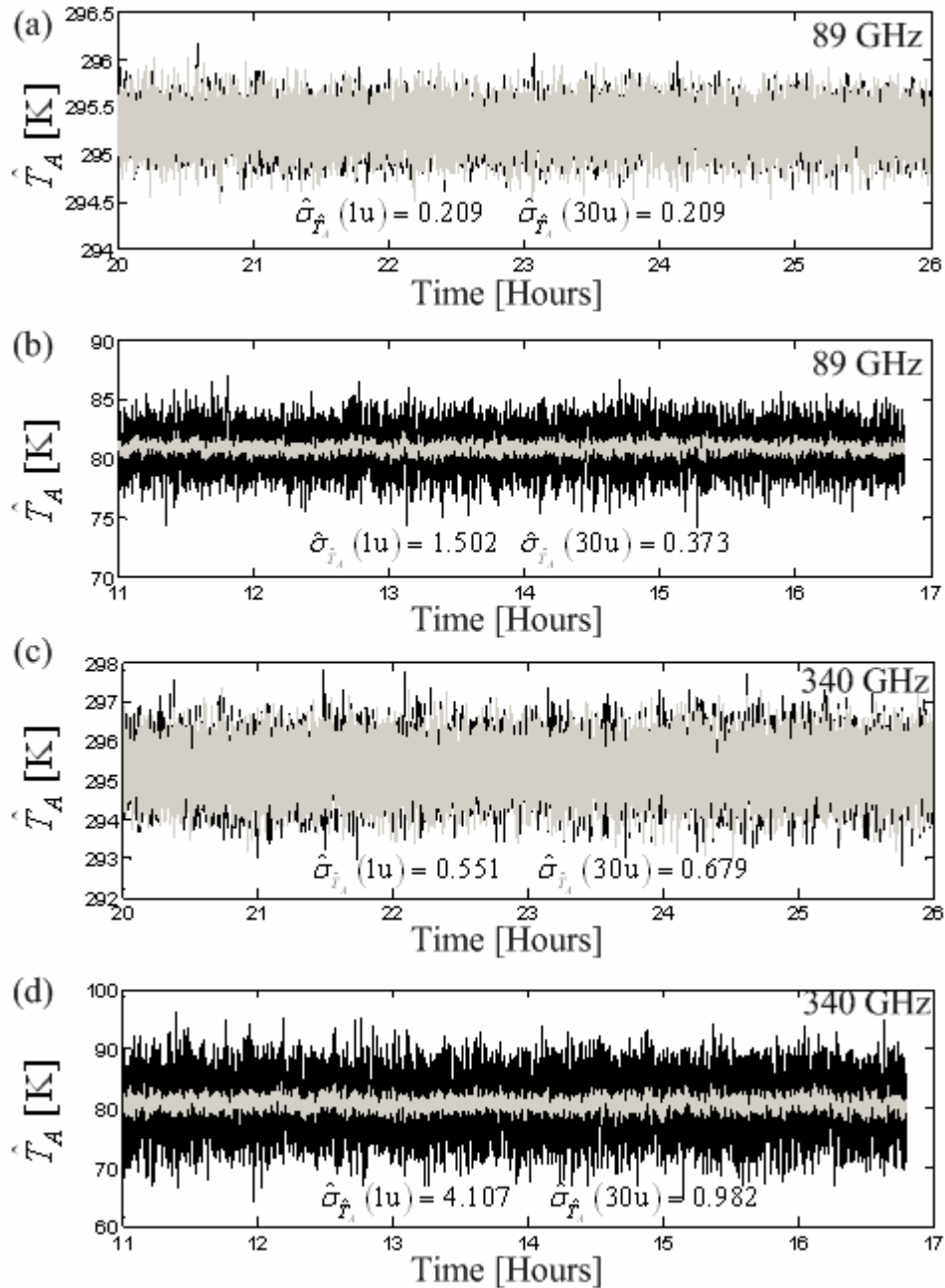


Figure 25: Calibrated brightness temperatures calculated using two different algorithms. Black lines indicate the results using the instantaneous calibration algorithm (1u); grey lines are the results using the 30 second averaging algorithm (30u). The standard deviations of the data runs are indicated on the plots. (a) 89 GHz for the T295 data set, (b) 89 GHz for the T80 data set, (c) 340 GHz for the T295 data set, (d) 340 GHz for the T80 data set.

The improvement in the 30u algorithm is evident in the T80 set shown in Fig. 25d; the standard deviations of the CryoTarget temperature estimates are $\hat{\sigma}_{\hat{T}_A}(1u) = 4.107 \text{ K}$ and $\hat{\sigma}_{\hat{T}_A}(30u) = 0.982 \text{ K}$. Using the 30u algorithm yields ~4 times lower standard deviation than the 1u algorithm.

The standard deviations of the CryoTarget estimates calculated using the 1u, 5u, and 30u algorithms are plotted along with model calculations in Fig. 26. Model calculations were performed to predict the performance of the three algorithms over a range of measurand temperatures using the above stated parameters for the 89 GHz and 340 GHz receivers. The measurement uncertainty was calculated using (3.22). (In (3.22), the uncertainty in the knowledge of the calibration reference temperature, \bar{T}_p , is assumed zero, i.e. $\sigma_{\bar{T}_p} = 0$.) Figures 26a and 26b show the results for the 89 GHz and 340 GHz, respectively; each plot has six data points corresponding to the three algorithms and the two CryoTarget temperatures. The model calculations for the 1u and 5u algorithms match the data very well. The standard deviations of the data obtained using the 30u algorithm are somewhat higher than the model calculations. The higher standard deviations are attributed to nonstationary fluctuations in the receiver response; the model calculations do not include the effects of nonstationary fluctuations in the receiver.

It is useful to compare Fig. 26 with Fig. 9. Fig. 9 was calculated using different algorithms and parameters, however, both figures illustrate how calibration errors are amplified by extrapolating the calibration data. It is this amplification of calibration errors through extrapolation of calibration data that provides the means to assess the influence of small calibration errors attributed to differences in calibration algorithms. Though the experiment was designed primarily to study modeling techniques for nonstationary receiver fluctuations, analysis of the nonstationary fluctuations and comparisons with model calculations are not presented in this dissertation.

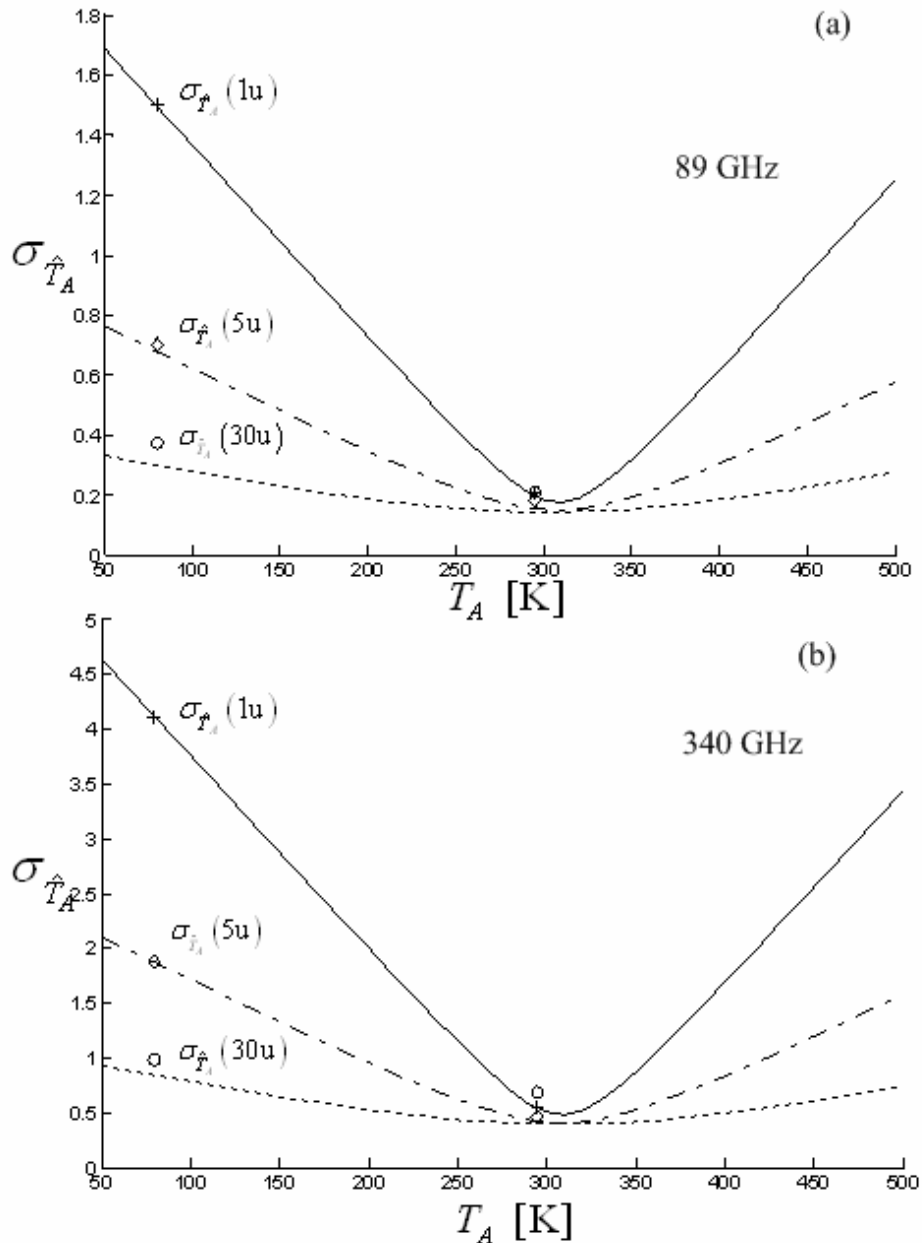


Figure 26: Comparisons of measured standard deviation and modeled uncertainty of the T295 and T80 data sets using three different calibration algorithms. (a) Results for the 89 GHz channel, (b) results for the 340 GHz channel.

5.4 Summary

An experiment was conducted to test some of the model predictions of measurement uncertainty through comparisons with data. Radiometric observations were made of three stable references for extended periods of time. The data collected during the experiment were of general poor quality. Examination of the unprocessed data revealed excess noise characteristic of problems with the data digitization electronics. The 89 GHz and 340 GHz radiometric channels appeared least affected by the problem although each channel exhibited significant excess noise. These data were used in a comparative analysis with model calculations.

Three calibration algorithms were applied to the data and a time series of estimates of the third stable reference were obtained from which calculations of the standard deviation of the time series were made. The amplification of calibration errors through the extrapolation of calibration data was clearly demonstrated in the data analysis shown in Fig. 25. There was generally good agreement between the standard deviation of the data and calculation of measurement uncertainty shown in Fig. 26. Model calculations predict well the amplification of calibration errors through the extrapolation of calibration data. However, differences exist between the model and data for the 30u algorithm. These differences can be attributed to nonstationary fluctuations that were not taken into account in the model calculations. Errors in estimating the receiver noise temperatures, errors in the receiver bandwidth and integration times, and poorly characterized excess noise caused by the digitization electronics are other factors contributing to the model calculation errors.

Comparisons of model calculations with data demonstrate the effectiveness of the technique presented in this dissertation to model the performance of radiometer calibration designs through the calculation of measurement uncertainty.

CHAPTER 6

CONCLUSION

The invention of the Dicke radiometer spawned radio astronomy. The ingenious circuit permitted the detection of very weak signals with an otherwise noisy receiver. Radio astronomy eventually led to the application of radiometry for studying the Earth's environment. Historically, radiometers have been designed to discriminate small changes in emission. Hence, radiometric resolution was established as a figure of merit to assess the performance of radiometer designs. Today radiometry has evolved into a key metrology for operational observations applied to weather forecasting and for monitoring climate. These applications have imposed more stringent requirements on the sensors' calibration. Over the past 30 years, there has been a growing diversity in radiometer designs to accommodate the need for improved accuracy. In this dissertation, radiometric resolution is shown to be an inadequate figure of merit to assess the performance of radiometer designs including their calibration scheme. Alternatively, measurement uncertainty is demonstrated to be a figure of merit generally applicable to evaluating radiometer designs.

In Chapter 2 a review of the literature showed that radiometric resolution is an established figure of merit by which to characterize the performance of a radiometer design. Radiometric resolution is an important parameter to consider when designing a radiometer, however, difficulties arise when using resolution to evaluate the performance of a calibration design. To demonstrate this point, the definition of radiometric resolution was examined. It was shown that radiometric resolution is defined and evaluated for the *mean system response* at a single system temperature (T_{sys}). Calibration inevitably involves changing the system temperature to obtain an estimate of the system response; uncertainty in the estimate of the system response is unavoidable. Thus, the theoretical basis for using radiometric resolution to characterize the performance of a calibration design is questionable since calibration unavoidably entails the switching of the input signal between multiple sources to obtain an imperfect estimate of the system response. Measurement uncertainty is a more appropriate figure of merit for assessing the performance of a radiometer and its calibration. Measurement uncertainty includes the radiometric resolution of the measurand observation as well as the uncertainty associated with utilizing imperfect calibration data. In this research measurement

uncertainty is defined as the mean square difference between the estimated value and the true value of the measurand.

In Chapter 3 a generalized technique is presented for calculating the measurement uncertainty of a radiometer. A general radiometer calibration model is introduced that describes a wide variety of calibration architectures. Most radiometers contain calibration features from one or more of the three tiers identified by the model. Regardless from which tier an observation is made, the observed signal can be modeled by a random process; all signals observed are treated as originating from simultaneously existing random processes. The radiometer output is thus comprised as a sequence of samples obtained from a set of different random processes. The statistics of the calibration reference and measurand samples are derived from the properties of the underlying random processes. The statistics are then used with the functional form of the calibration algorithm to compute the measurement uncertainty. The generalized technique presented can be applied to all radiometer designs that can be decomposed into a set of subsystems that represent total-power-mode observations. A simple framework for modeling the calibration algorithm which can be applied to a wide variety of calibration designs is presented whereby the radiometer is decomposed into a set of subsystems with characteristic equations that can be solved using least squares regression (LSR).

In Chapter 4 the utility of measurement uncertainty as a figure of merit is demonstrated by evaluating the performance of a variety of calibration schemes. The LSR framework is used to study the influence of calibration reference temperatures, number of calibration references, integration time of the calibration references and the measurand, reference averaging, and weighting of the calibration measurements. The technique presented has been applied to evaluating calibration designs using two and more calibration references and to systems utilizing reference averaging. The effect of interpolating and extrapolating calibration data on measurement uncertainty is shown. The optimum fraction of time spent observing the measurand is shown to depend on the calibration reference temperatures. The measurement uncertainty of a radiometer that uses external calibration measurements (tier 3) to estimate the value of an injected noise is evaluated using the generalized technique. The effect of the external calibration reference temperatures and uncertainty in the knowledge of the reference temperature values on measurement uncertainty is also examined.

In Chapter 5, an experiment is described which was conducted to evaluate the modeling technique for measurement uncertainty presented in this dissertation. Although the data set collected had problems, some of the data were of adequate quality to process and compare with model calculations. The data were processed using three different calibration algorithms and the standard deviations of the resultant brightness temperature time series were calculated. The data clearly demonstrate the amplification of calibration errors through the extrapolation of calibration data. The standard deviations were compared with model calculations of the measurement uncertainty using the same algorithms and parameters that describe the measurement set up. Overall, the model calculations agreed well with the data.

In this research measurement uncertainty has been introduced as a figure of merit to evaluate radiometer designs. As with most figures of merit, one must use discretion in their application for judging performance; other factors may also be important. For some measurements, resolution of the measurand observation may be paramount; or alternatively, maintaining the ability to monitor system linearity by means of a multi-point calibration may take precedence. Regardless, measurement uncertainty is a quantitative measure that can be used for assessing the performance of radiometer designs.

REFERENCES

- ANSI, *American National Standard for Calibration – U.S. Guide to the expression of uncertainty in measurement*, ANSI/NCSL Z540-2-1997, NCSL International, Boulder, CO, 1997.
- Blackwell, W.J., J.W. Barrett, F.W. Chen, R.V. Leslie, P.W. Rosenkranz, M.J. Schwartz, and D. H. Staelin, NPOESS Aircraft Sounder Testbed-Microwave (NAST-M): instrument description and initial flight results, *IEEE Trans. Geosci. Rem. Sensing*, 39(11), 2001, pp. 2444-2453.
- Bremer, J., Improvement of Scanning Radiometer Performance by Digital Reference Averaging, *IEEE IM*, 28(1), 1979, pp. 46 – 54.
- Buderi, R., *The invention that changed the world: how a small group of radar pioneers won the Second World War and launched a technological revolution*, Simon & Schuster, New York, NY, 1996.
- Conglong, Z., J.B. Snider, D.C. Hogg, Computer Demodulation Technique for a Dual-Channel Microwave Radiometer, *Advances in Atmospheric Sciences*, 3(2), 1986, pp. 189-198.
- Corbella, I., A.J. Gasiewski, M. Klein, V. Leuski, A.J. Francavilla, and J.R. Piepmeier, On-board accurate calibration of dual-channel radiometers using internal and external references, *IEEE Trans. on Microwave Theory and Techniques*, 50(7), 2002, pp.1816 – 1820.
- Davis, A., A. Marshak, W. Wiscombe, and R. Cahalan, Scale Invariance of Liquid Water Distribution in Marine Stratocumulus, Part 1: Spectral Properties and Stationary Issues, *J. of Atmos. Sci.*, 53(11), 1996, pp. 1538 – 1558.
- Dicke, R.H., The measurement of thermal radiation at microwave frequencies, *Rev. Sci. Instr.*, 17, 1946, pp. 268 - 279.
- Draper, N. R., H. Smith, *Applied Regression Analysis, Third Edition*, John Wiley and Sons, Inc., New York, 1998.
- Evans, K.F., J.R. Wang, P. Racette, G.M. Heymsfield, and L. Lihua, Ice Cloud Retrievals and Analysis with the Compact Scanning Submillimeter Imaging Radiometer and the Cloud Radar System during CRYSTAL-FACE, *J. Geophys. Res.* , 2005, in press.
- Goldstein, S.J. Jr., “A comparison of Two Radiometer Circuits,” Proc. IRE 43, 1955, pp. 1663 – 1666.
- Gorbachev, M., Out of Water, The Distant Alarm Comes Closer, *Civilization*, Oct-Nov 2000, pp. 82 – 84.
- Hach, J.P., A very Sensitive Airborne Microwave Radiometer Using Two Reference Temperatures, *IEEE Trans. on Microwave Theory and Techniques*, 16(9), 1968, pp. 629 – 636.

- Han, Y., E. R. Westwater, Analysis and improvement of tipping calibration for ground-based microwave radiometers, *IEEE Trans. Geosci. Rem. Sensing*, 38(3), 2000, pp. 1260-1276.
- Hersman, M.S., G.A. Poe, Sensitivity of the Total Power Radiometer with Periodic Absolute Calibration, *IEEE Trans. on Microwave Theory and Techniques*, 29(1), 1981, pp. 32 – 40.
- Huang, N. E., Z. Shen, S. R. Long, M. C. Wu, H. S. Hsing, Q. Zheng, N-C. Yen, C. C. Tung, and H. H. Liu, The empirical mode decomposition and the Hilbert Spectrum for nonlinear and non-stationary time series analysis, *Proceedings of the Royal Society*, 454, 1998, pp. 903-995.
- Huang, N.E., Z. Shen, S.R. Long, A New View of Nonlinear Water Waves: The Hilbert Spectrum, *Annu. Rev. Fluid Mech.*, 31, 1999, pp. 417 – 457.
- IEEE, *The IEEE Standard Dictionary of Electrical and Electronic Terms*, IEEE Standard 100, 1996.
- ISO, *International Vocabulary of Basic and General Terms in Metrology. Second Edition*, International Organization for Standardization, Switzerland, 1993.
- Jackson, D.M., *Calibration of Millimeter-Wave Radiometers with Application to Clear-Air Remote Sensing of the Atmosphere*, Doctoral dissertation submitted to the Georgia Institute of Technology, July 1999.
- Johnson, S.L., B.H. Smith, D.A. Calder, Noise spectrum Characteristics of Low-noise Micrwave Tubes and Solid-State Devices, *Proc. IEEE*, 54(2), 1966, pp. 258 – 266.
- Kelly, E.J., D.H. Lyons, and W.L. Root, The Sensitivity of Radiometric Measurements, *J. Soc. Indust. Appl. Math.*, 11(2), June 1963, pp. 235 – 257.
- Kraus, J.D., *Radio Astronomy*, Cygnus Quasar Books, Powell, OH, 1966.
- Kunzi, K., A. Magun, Statistical gain fluctuations of microwave amplifiers measured with a Dicke-radiometer, *Math Phys.*, 22, 1977, pp. 404-411.
- Le Vine, D.M., The sensitivity of synthetic aperture radiometers for remote sensing applications from space, *Radio Sci.*, 25(4), 1990, pp. 441-453.
- Liljegren, J. C., Automatic Self-Calibration of ARM Microwave Radiometers, in *Microwave Radiometry and Remote Sensing of the Earth's Surface and Atmosphere*, pp. 433-441, edited by P. Pampaloni and S. Paloscia, VSP Press, 2000.
- McGrath, A., T. Hewison, Measuring the accuracy of MARSS - An airborne microwave radiometer, *J. Atmos. Oceanic Techn.*, 18(12), 2001, pp. 2003-2012.
- Miller, C.K.S., W.C. Daywitt, and M.G. Arthur, Noise standards, measurements, and receiver noise definitions, *Proc. of the IEEE*, 55(6), 865 – 877, 1967.

Peckham, G.E., An Optimum calibration procedure for radiometers, *Int. J. Remote Sensing*, 10(1), 1989, pp.227-236.

Piepmeier, J.R., Calibration of Passive Microwave Polarimeters that Use Hybrid Coupler-Based Correlators, *IEEE Trans. on Geoscience and Remote Sensing*, Vol. 42, No. 2, Feb. 2004.

Piepmeier, J.R., P. Racette, W. Manning, J.R. Wang, The airborne Conical Scanning Millimeter-wave Imaging Radiometer (CoSMIR), *Proc. International Geoscience And Remote Sensing Symposium'02*, IEEE-GRSS, June 2002.

Racette, P., J. R. Wang, P. Evans, R. Saunders, A. Gasiewski, and D. Jackson, A calibration experiment using millimeter-wave imaging radiometer at the UK meteorological office calibration facility, *Proc. International Geoscience And Remote Sensing Symposium'98*, IEEE-GRSS, Florence, Italy, July 1995.

Racette, P., R. F. Adler, J. R. Wang, A. J. Gasiweski, D. M. Jackson, and D. S. Zacharias, An airborne millimeter-wave imaging radiometer for cloud, precipitation, and atmospheric water vapor studies, *J. Atmos. Oceanic Techn.*, 13(3), 1996, pp. 610 – 619.

Racette, P. and J. R. Wang, Passive millimeter- and sub-millimeter-wave imaging for atmospheric research, *Proc. of the International Society for Optical Engineering 12th Annual Symposium*, Orlando, FL, April 1998.

Racette, P., M. Triesky, and D.C. Jones, A multi-channel microwave radiometer uses reference averaging for calibration: precision approaches that of a total power radiometer, *Proc. International Geoscience And Remote Sensing Symposium '98*, IEEE-GRSS, Seattle, WA July, 1998.

Racette, P. and R. Lang, Consideration of Uncertainties in the Estimated Calibration Response of Radiometer Systems, *Progress in Electromagnetics Research Symposium*, (PIERS), Boston, MA., July 2000a.

Racette, P. and R. Lang, Evaluation of Radiometer System Performance By Considering Uncertainties in the Estimated Calibration Response, *MicroCal 2000*, College Park, MD., October, 2000b.

Racette, P. and R. Lang, Radiometer System Analysis and Non-Stationary Processes, *Proc. MicroRad 2001*, Boulder, CO., Nov. 2001

Racette, P. and R. Lang, Comparative analysis of radiometer systems using non-stationary processes, *Proc. International Geoscience And Remote Sensing Symposium 2002*, Toronto, Canada, July 2002a.

Racette, P. and R. Lang, Experimental Investigations of Non-Stationary Properties In Radiometer Receivers Using Measurements of Multiple Calibration References, MicroCal 2002, Barcellona Spain, Nov. 2002b.

Racette, P., J.R. Wang, K.F. Evans, B. Monosmith, Z. Zhang, CoSSIR: A New Instrument For Exploring the Utility of Submillimeterwave Radiometry For Earth Observation, *Proc. MicroRad 2004*, Rome, Italy, Feb 2004.

Racette, P., E. Westwater, Y. Han, A. Gasiewski, M. Klein, D. Cimini, D. Jones, W. Manning, E. Kim, J.R. Wang, V. Leuski, P. Kiedron, Measurement of Low Amounts of Precipitable Water Vapor Using Ground-Based Millimeterwave Radiometry, *J. Atmos. Oceanic Techn.*, 2005 in press.

Randa, J., Uncertainties in NIST Noise Measurements, NIST Technical Note 1502, March 1998.

Rohlfs, K., T.L. Wilson, *Tools of Radio Astronomy*, Springer-Verlag, New York, NY, 1996.

Ruf, C.S., Detection of calibration drifts in spaceborne microwave radiometers using a vicarious cold reference, *IEEE Trans. Geosci. Rem. Sensing*, 38(1), 44 – 52, 2000.

Ruf, C. S., S.J. Keihm, and M.A. Janssen, TOPEX/Poseidon Microwave Radiometer (TMR): I. Instrument Description and Antenna Temperature Calibration, *IEEE Trans. Geosci. Rem. Sensing*, 33(1), 125 – 137, 1995.

Saunders, R.W., T.J. Hewison, S.J. Stringer, and N.C. Atkinson, The Radiometric Characterization of AMSU-B, *IEEE Trans. on Microwave Theory and Techniques*, 43(4), 1995, pp. 760 – 771.

Skou, N. *Microwave Radiometer Systems: Design and Analysis*, Artech House, Norwood, MA, 1989.

Stelzried, C.T., Microwave thermal noise standards, *IEEE Trans. on Microwave Theory and Techniques*, 16(9), 646 – 655, 1968.

Tanner, A., and A. Lance Riley, Design and performance high-stability water vapor radiometer, *Radio Sci.*, 38(3), 2003.

Thomsen, F. On the Resolution of Dicke-Type Radiometers, *IEEE Trans. on Microwave Theory and Techniques*, 32(2), 1984, 145 – 150.

Tiuri, M.E., Radio Astronomy Receivers, *IEEE Trans. on Mil. Electro.*, 8, 1964, pp. 264-272.

Ulaby, F.T., R.K. Moore, and A.K. Fung, *Microwave Remote Sensing: Active and Passive, Vol 1, Microwave Remote Sensing Fundamentals and Radiometry*, Addison Wesley Publishing Company, Reading, MA, 1981.

Van Putten, A.F.P., *Electronic Measurement Systems, Theory and Practice*, pp. 110 – 152, Institute of Physics Publishing, Philadelphia, PA, 1996.

Wait, D.F., The Sensitivity of the Dicke Radiometer, *J. of Research of the National Bureau of Standards*, 71(2), 1967, pp. 127 – 152.

Wentz, F. J., P. Ashcroft, and C. Gentemann, Post-Launch Calibration of the TRMM Microwave Imager, *IEEE Trans. Geosci. Rem. Sensing*, 39(2), 415 – 422, 2001.

Wollack, E.J., High Electron-Mobility-Transistor Gain Stability and Its Design Implications for Wide Band Millimeter-wave Receivers, *Rev. Sci. Instrum.*, 66(8), August 1995, pp. 4305 – 4312.

Wyatt, C.L., V. Privalsky, R. Datla, *Recommended Practice; Symbols, Terms, Units and Uncertainty Analysis for Radiometric Sensor Calibration*, NIST Handbook 152, US Department of Commerce Technology Administration, 1998.

APPENDIX A

RADIOMETRIC RESOLUTION

A.1 Derivation of Resolution for a Radiometer Receiver With Gain Fluctuations

In this appendix the radiometric resolution is evaluated for a direct detection radiometer with gain fluctuations operating in total-power mode. The derivation most closely follows that presented by *Rohlf and Wilson* [1996, chapter 4] but differs in that it includes the effects of gain fluctuations.

A model for such a direct detection radiometer is shown in Fig. A1. The receiver is comprised of an amplifier, pre-detection filter (H), an ideal square-law detector, and post-detection filter (W). The input signal to the radiometer receiver, $x(t)$, is assumed to be Johnson noise represented by a zero-mean Gaussian random process with a power spectral density given by

$$S_x(f) = kT_{\text{sys}} \quad (\text{A.1})$$

where k is Boltzman's constant and T_{sys} is the system noise temperature. The system noise temperature is equal to the sum of the receiver noise temperature (T_{rec}) and the apparent antenna temperature (T_p) at the radiometer input, i.e. $T_{\text{sys}} = T_{\text{rec}} + T_p$. The impulse responses of the causal pre-detection and post-detection filters are $h(t)$ and $w(t)$, respectively. The frequency responses of the filters are given by the Fourier transform pairs,

$$W(f) = \int_{-\infty}^{\infty} w(t)e^{-i\omega t} dt \quad H(f) = \int_{-\infty}^{\infty} h(t)e^{-i\omega t} dt \quad (\text{A.2})$$

where $\omega = 2\pi f$. The bandwidth of the pre-detection filter is assumed to be much larger than the

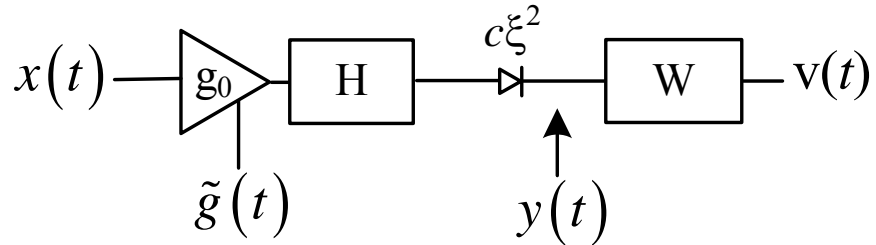


Figure A1: Block diagram of a direct detection radiometer receiver.

bandwidth of the post-detection filter. The amplifier gain is expressed as the sum of the mean and a fluctuating component, i.e.,

$$g(t) = g_0 + \tilde{g}(t) \quad (\text{A.3})$$

where g_0 is the mean value of $g(t)$ and $\tilde{g}(t)$ is the fluctuating component. The fluctuating component is modeled as a zero-mean Gaussian random process. By assuming $\tilde{g}(t)$ is wide-sense-stationary, the Fourier transform relationship between its autocorrelation function and power spectrum exists, such that

$$E\{\tilde{g}(t_1)\tilde{g}^*(t_2)\} \equiv R_{\tilde{g}}(\Delta t) = \int_{-\infty}^{\infty} S_{\tilde{g}}(f) e^{i\omega\Delta t} df \quad (\text{A.4})$$

where $\Delta t = t_2 - t_1$, * denotes the complex conjugate, and $R_{\tilde{g}}(\Delta t)$ and $S_{\tilde{g}}(f)$ are the autocorrelation and power spectrum of $\tilde{g}(t)$, respectively. In the proceeding analysis, it is assumed that $g(t)$ and $x(t)$ are independent and that the fluctuation in $\tilde{g}(t)$ is much slower than the impulse response of $h(t)$. The fluctuation can exist on the same time scale as the impulse response of the post-detection filter.

The receiver input passes through an amplifier, filter, and an ideal square-law detector. The output of the square law detector is denoted $y(t)$; and $v(t)$ is the voltage output of the post-detection filter. By assuming the gain fluctuations are slow, the output of the amplifier can be expressed as the instantaneous product $x(t)g(t)$. The output of the square law detector is

$$y(t) = c(x(t)g(t) \otimes h(t))^2 \quad (\text{A.5})$$

where \otimes is the convolution operator, c is the gain of the square-law detector (usually expressed in units of Volts per Watts). The output of the post-detection filter is

$$\begin{aligned} v(t) &= y(t) \otimes w(t) \\ &= c \cdot \int_{-\infty}^{\infty} dt''' w(t''') \int_{-\infty}^{\infty} dt' h(t') \int_{-\infty}^{\infty} dt'' h(t'') x(t-t'-t'') g(t-t'-t''') x(t-t''-t''') g(t-t''-t''') \end{aligned} \quad (\text{A.6})$$

By making use of the Fourier relationships and the above stated assumptions (i.e., $x(t)$ is zero-mean Gaussian and $\tilde{g}(t)$ and $w(t)$ are slow with respect to $h(t)$) the expected value of the output is found to be

$$E\{v(t)\} = \bar{v}_p = ckW(0)T_{sys} \cdot \left(\int df |H(f)|^2 \right) \cdot (g_0^2 + R_{\tilde{g}}(0)) . \quad (\text{A.7})$$

The ensemble average includes all possible output voltages that correspond to system noise temperature. Equation (A.7) shows the linear relationship between the input brightness temperature to the output voltage. This linear relationship arises from the square-law detection of the input signal. Equation (A.7) can be rewritten to explicitly show the linear relationship,

$$\bar{v}_p = \mu T_p + \beta \quad (\text{A.8})$$

where

$$\mu = ckW(0) \left(\int df |H(f)|^2 \right) \cdot (g_0^2 + R_{\tilde{g}}(0)) \quad (\text{A.9})$$

and

$$\beta = \mu T_{rec} . \quad (\text{A.10})$$

The resolution is found by evaluating

$$(\Delta T)^2 = \frac{\sigma_v^2}{\left(\frac{\partial \bar{v}}{\partial T} \right)^2} \Big|_{T_{sys}} . \quad (\text{A.11})$$

(See Chapter 2, (2.6) and accompanying discussion.) First consider the denominator; differentiating (A.7) with respect to T_{sys} one finds

$$\left. \left(\frac{\partial}{\partial T} E\{v(t)\} \right)^2 \right|_{T=T_{sys}} = \mu^2 . \quad (\text{A.12})$$

where μ is given by (A.9).

Evaluation of the numerator is more involved since it requires finding the variance of the output which in turn involves evaluating the fourth moment statistics of $g(t)$ and $x(t)$. The variance is found from the zero-lag covariance function of the receiver output. The covariance function is given by

$$E\{v(t_1)v^*(t_2)\} = C_v(\Delta t) = \int_{-\infty}^{\infty} S_y(f) |W(f)|^2 e^{-i\omega\Delta t} df - E^2\{v(t)\} \Big|_{T=T_{sys}} \quad (\text{A.13})$$

where $S_y(f)$ is the power spectrum at the output of the square law detector and is found from the Fourier transform of the autocorrelation function

$$R_y(\Delta t) = E\{y(t_1)y^*(t_2)\} . \quad (\text{A.14})$$

Evaluating (A.14) requires calculating the forth moment expected averages of $x(t)$ and $g(t)$. In this calculation the relationship,

$$E\{x(t_1)x(t_2)x(t_3)x(t_4)\} = R_{x_{12}}R_{x_{34}} + R_{x_{13}}R_{x_{24}} + R_{x_{14}}R_{x_{23}} \quad (\text{A.15})$$

for zero-mean Gaussian random processes is used where $R_{x_{ij}} = E\{x(t_i)x(t_j)\}$. To evaluate (A.14), substitute the corresponding Fourier transforms for $R_x(\bullet)$ and $R_{\tilde{g}}(\bullet)$, apply the Fourier exponents to transform the filter impulse responses to the frequency domain, utilize the assumption that the bandwidth of $H(f)$ is much larger than the bandwidth of $S_{\tilde{g}}(f)$, and term by term use the remaining integrals to transform the power spectrum of the gain fluctuations back into the time domain. After grouping like terms,

$$\begin{aligned} R_y(\Delta t) &= c^2 R_H^2(0) \cdot \left[g_0^4 + 2g_0^2 R_{\tilde{g}}(0) + R_{\tilde{g}}^2(0) + 2R_{\tilde{g}}^2(\Delta t) + 4g_0^2 R_{\tilde{g}}(\Delta t) \right] + \\ &\quad 2c^2 R_H^2(\Delta t) \cdot \left[g_0^4 + 2g_0^2 R_{\tilde{g}}(0) + R_{\tilde{g}}^2(0) + 2R_{\tilde{g}}^2(\Delta t) + 4g_0^2 R_{\tilde{g}}(\Delta t) \right] \end{aligned} \quad (\text{A.16})$$

where

$$R_H(\Delta t) = \int_{-\infty}^{\infty} S_x(f) |H(f)|^2 e^{i\omega\Delta t} df.$$

By subtracting the DC component from (A.16), (A.13) may be expressed as

$$C_v(\Delta t) = \int_{-\infty}^{\infty} S_r(f) |W(f)|^2 e^{i\omega\Delta t} df \quad (\text{A.17})$$

where

$$\begin{aligned} S_r(f) &= 2c^2 R_H^2(0) (S_{\tilde{g}} \otimes S_{\tilde{g}}) + 4c^2 R_H^2(0) g_0^2 S_{\tilde{g}} + \\ &\quad (2c^2 g_0^4 + 6c^2 R_{\tilde{g}}^2(0) + 12c^2 g_0^2 R_{\tilde{g}}(0)) \cdot S_H \otimes S_H \end{aligned}$$

and S_H is the Fourier transform of R_H . The variance of the output is found by evaluating (A.17) with $\Delta t = 0$. It is noteworthy to observe that the variance obtained from (A.17) is the starting point for analysis presented in *Hersman and Poe, [1981]*.

Substituting (A.1) into (A.17) and making use of the bandwidth assumption between the pre-detection and post-detection filters yields

$$C_v(\Delta t) = \left[(g_0^4 + 3R_{\tilde{g}}^2(0) + 6g_0^2 R_{\tilde{g}}(0)) 2c^2 k^2 T_{sys}^2 \int_{-\infty}^{\infty} df' |H(f')|^4 \right] \int_{-\infty}^{\infty} df |W(f)|^2 e^{i\omega \Delta t} . \quad (A.18)$$

$$+ 4c^2 g_0^2 k^2 T_{sys}^2 \left[\int_{-\infty}^{\infty} df' |H(f')|^2 \right]^2 \int_{-\infty}^{\infty} df'' |W(f'')|^2 S_{\tilde{g}}(f'') e^{i\omega \Delta t}$$

The first term on the right hand side of (A.18) is the covariance due to the band-limited noise at the receiver input; this term gives rise to the classic formula

$$\Delta T \cong \frac{T_{sys}}{\sqrt{B\tau}} . \quad (A.19)$$

Its correlation interval is governed by the bandwidth of the post-detection filter. Receiver gain fluctuations give rise to the second term on the right hand side. For gain fluctuations that are slow with respect to Δt and small in magnitude compared to g_0 , the covariance function of the receiver output can be expressed as

$$C_v(\Delta t) = 2g_0^4 c^2 k^2 T_{sys}^2 \int_{-\infty}^{\infty} df' |H(f')|^4 R_w(\Delta t) . \quad (A.20)$$

$$+ 4c^2 g_0^2 k^2 T_{sys}^2 \left[\int_{-\infty}^{\infty} df' |H(f')|^2 \right]^2 W^2(0) R_{\tilde{g}}(\Delta t)$$

where

$$R_w(\Delta t) = \int_{-\infty}^{\infty} df |W(f)|^2 e^{i\omega \Delta t} . \quad (A.21)$$

The covariance function given by (A.20) is a linear combination of R_w and $R_{\tilde{g}}$ scaled by g_0^4 and g_0^2 , respectively. The contribution of $R_{\tilde{g}}$ is usually negligible for computing the output variance since receiver gain fluctuations are typically small over the integration interval defined by $W(f)$. The contribution of R_w to the covariance between sequential samples, e.g. calibration observations, is usually very small since R_w tends to decay rapidly on time scales longer than the sampling interval. Gain fluctuations become more predominant for the covariance between samples as the time interval increases. Although we have assumed stationarity, one must keep in mind that gain fluctuations are inherently non-stationary; $R_{\tilde{g}}(\Delta t)$ may not adequately represent the gain fluctuations since it is an autocorrelation function of a wide-sense-stationary process. The covariance function given by (A.18) is valid for time intervals over which the fluctuations

can be considered stationary. It should be noted that the covariance given by (A.18) changes slightly when the time interval encompasses observations at two different system temperatures, i.e. $T_{sys}^2 \rightarrow T1 \cdot T2$ where $T1$ and $T2$ are the system temperatures at the two times.

The radiometric resolution is obtained by substituting (A.12) and the variance obtained from (A.18) into (A.11). The following definitions are adopted from *Tiuri*, [1964]. The pre-detection bandwidth is

$$B = \frac{\left(\int_{-\infty}^{\infty} |H(f)|^2 df \right)^2}{\int_{-\infty}^{\infty} |H(f)|^4 df} \quad (\text{A.22})$$

and the post-detection integration time constant is

$$\tau = \frac{W^2(0)}{2 \int_{-\infty}^{\infty} |W(f)|^2 df}. \quad (\text{A.23})$$

After making the substitutions

$$\left(\frac{\Delta T}{T_{sys}} \right)^2 = \frac{2 \int_{-\infty}^{\infty} (S_{\tilde{g}} \otimes S_{\tilde{g}} + 2g_0^2 S_{\tilde{g}}) |W(f)|^2 df}{(g_0^2 + R_{\tilde{g}}(0))^2 W^2(0)} + \left(\frac{g_0^4 + 3R_{\tilde{g}}^2(0) + 6g_0^2 R_{\tilde{g}}(0)}{(g_0^2 + R_{\tilde{g}}(0))^2} \right) \frac{1}{B\tau}. \quad (\text{A.24})$$

By making the assumption that the mean gain is much larger than the gain fluctuations, i.e. $g_0^2 \gg R_{\tilde{g}}(0)$, (A.24) can be further simplified to obtain

$$\Delta T \cong T_{sys} \cdot \left(\frac{1}{B\tau} + \left(\frac{\Delta G}{G} \right)^2 \right)^{1/2} \quad (\text{A.25})$$

where

$$\left(\frac{\Delta G}{G} \right)^2 = \left(\frac{2}{W(0) \cdot g_0} \right)^2 \int df S_{\tilde{g}}(f) |W(f)|^2. \quad (\text{A.26})$$

A.2 Comparison with Other Developments

In Appendix A.1 the radiometric resolution for a receiver was developed using a wide-sense stationary stochastic model for the gain fluctuations. The derivation differs from others

presented in the literature where the gain is treated as a random variable. The following summarizes the development presented by *Ulaby et al.* [1981, pp. 367-368], *Rohlf and Wilson* [1996, pp. 64-66], and *Kraus* [Chapter 7-1e, 1966]. The results are then compared to the results obtained in Appendix A.1.

The measured signal at the receiver output voltage is proportional to the system noise temperature, T_{sys} , i.e.

$$v \propto GT_{\text{sys}} \quad (\text{A.27})$$

where G is the overall system gain. A change in the system gain (ΔG) will produce a change in the voltage output (Δv) according to

$$v + \Delta v = (G + \Delta G)T_{\text{sys}}. \quad (\text{A.28})$$

A change of the antenna brightness temperature (ΔT) will also produce a change in the output voltage according to

$$v + \Delta v = G(T_{\text{sys}} + \Delta T). \quad (\text{A.29})$$

The change Δv due to a change in the antenna brightness temperature is indistinguishable from changes in the system gain. Equating (A.28) and (A.29) yields the relationship

$$\Delta T = \frac{\Delta G}{G} T_{\text{sys}}. \quad (\text{A.30})$$

Since the uncertainty due to gain fluctuations and the uncertainty due to the stochastic nature of the signal at the radiometer input are caused by unrelated mechanisms, the uncertainties are considered statistically independent. Therefore, the total uncertainty is expressed by the root sum square of the individual uncertainties given by (A.30) and (A.19). That is

$$\Delta T = T_{\text{sys}} \left(\frac{1}{B\tau} + \left(\frac{\Delta G}{G} \right)^2 \right)^{1/2}. \quad (\text{A.31})$$

Equation (A.31) is useful for studying the effects of receiver fluctuations on the resolution of the measurement. For example, Rohlf and Wilson assume that the gain fluctuation varies linearly with receiver integration time, i.e.

$$\left(\frac{\Delta G}{G} \right)^2 = \gamma_0 + \gamma_1 \tau. \quad (\text{A.32})$$

The integration time, τ_m , which corresponds to the best resolution is found by substituting (A.32) into (A.31) and differentiating (A.31) with respect to τ and setting the result equal to zero. Solving for τ yields

$$\tau_m = \frac{1}{\sqrt{B\gamma_1}}. \quad (\text{A.33})$$

The radiometric resolution continues to improve by increasing the integration time up to τ_m above which time the resolution is degraded.

The shortcoming of the presented analysis leading to (A.31) is that it provides little insight into the underlying processes and necessary assumptions that lead to the result. This shortcoming is somewhat alleviated in the following analysis. To do this, we first assume that the voltage gain is a Gaussian random variable and substitute $S_{\tilde{g}}(f) = \sigma_{\tilde{g}}^2 \delta(f)$ into (A.24) where $\delta(f)$ is the Dirac delta function.

$$\left(\frac{\Delta T}{T_{\text{sys}}}\right)^2 = \frac{4g_0^2\sigma_g^2 + 2\sigma_g^4}{(g_0^2 + \sigma_g^2)^2} + \frac{3\sigma_g^4 + 6g_0^2\sigma_g^2 + g_0^4}{(g_0^2 + \sigma_g^2)^2} \frac{1}{B\tau}. \quad (\text{A.34})$$

Equation (A.34) may be converted into the more familiar form of (A.25) by transforming the random variable of the voltage gain into a random variable of the power gain. By defining the power gain G as

$$G = g^2, \quad (\text{A.35})$$

G is a random variable with mean

$$G_0 = E\{G\} = E\{g^2\} = g_0^2 + \sigma_g^2 \quad (\text{A.36})$$

and variance

$$(\Delta G)^2 = E\{(G - G_0)^2\} = 2\sigma_g^4 + 4g_0^2\sigma_g^2. \quad (\text{A.37})$$

Recognizing that

$$(\Delta G)^2 + G_0^2 = 3\sigma_g^4 + 6g_0^2\sigma_g^2 + g_0^4 \quad (\text{A.38})$$

and substituting (A.36) and (A.37) into (A.34) yields

$$\left(\frac{\Delta T}{T_{\text{sys}}}\right)^2 = \left(\frac{\Delta G}{G_0}\right)^2 + \left(1 + \left(\frac{\Delta G}{G_0}\right)^2\right) \frac{1}{B\tau}. \quad (\text{A.39})$$

By assuming $G_0 \gg \Delta G$, (A.39) is well approximated by

$$\left(\frac{\Delta T}{T_{\text{sys}}} \right)^2 = \left(\frac{\Delta G}{G_0} \right)^2 + \frac{1}{B\tau} \quad (\text{A.40})$$

which is the same form as (A.25). We see that (A.25) is equivalently based upon the assumption that the power gain is a random variable with mean gain G_0 much larger than its standard deviation ΔG which is proportional to the integral of $S_{\tilde{g}}(f)$ weighted by the frequency response of the post-detection filter.

APPENDIX B

REGRESSION OF CALIBRATION DATA

B.1 Regression of Data for estimating m and b

A set of n measurements consisting of pairs of voltages and temperatures $\{v_1, v_2, \dots, v_n, T_1, T_2, \dots, T_n\}$ represents a calibration set from which the system response, i.e. the slope m and offset b , can be estimated. Equation (3.4) is used to express the calibration data in terms of a set of n equations,

$$\begin{aligned} T_1 &= mv_1 + b + \varepsilon_1 \\ T_2 &= mv_2 + b + \varepsilon_2 \\ &\vdots \\ T_n &= mv_n + b + \varepsilon_n \end{aligned} \tag{B.1}$$

where $\{\varepsilon_1, \varepsilon_2, \dots, \varepsilon_n\}$ are zero-mean random variables representing deviations (or errors) of the measurement pairs from the mean system response, m and b . The values of the ε_i 's are not known and are not part of the data set but their second moment statistic, σ_{T_i} , represents deviation of the voltage (scaled by m) from its mean value and may include (as shown in B.4) uncertainty in the knowledge of T_i . For the present analysis these error terms are assumed to be independent. Least squares regression is used to find estimates of the slope and offset, \hat{m} and \hat{b} . The estimates are obtained by minimizing the sum of the squared error. That is, find \hat{m} and \hat{b} such that E,

$$E = \sum_{i=1}^n \varepsilon_i^2 = \sum_{i=1}^n (v_i \hat{m} + \hat{b} - T_i)^2, \tag{B.2}$$

is minimized. Estimates of \hat{m} and \hat{b} are found by solving

$$\begin{aligned} \frac{\partial E}{\partial \hat{m}} &= \sum_{i=1}^n 2v_i (v_i \hat{m} + \hat{b} - T_i) = 0 \\ \frac{\partial E}{\partial \hat{b}} &= \sum_{i=1}^n 2(v_i \hat{m} + \hat{b} - T_i) = 0 \end{aligned} \tag{B.3}$$

Solving (B.3) yields

$$\begin{aligned}\hat{m} &= \frac{\sum T_i v_i - \frac{1}{n} \sum v_i \sum T_j}{\sum v_i^2 - \frac{1}{n} (\sum v_i)^2} = \frac{\sum (v_i - \langle v \rangle_n) T_i}{\sum (v_i - \langle v \rangle_n)^2} \\ \hat{b} &= \frac{1}{n} \sum T_i - \frac{\hat{m}}{n} \sum v_i = \langle T_i \rangle_n - \hat{m} \langle v_i \rangle_n\end{aligned}\quad (\text{B.4})$$

where the summations are from 1 to n and $\langle T_i \rangle_n$ and $\langle v_i \rangle_n$ are arithmetic means of the calibration set. Note that

$$\sum v_i^2 - \frac{1}{n} (\sum v_i)^2 = \sum (v_i - \langle v_i \rangle_n)^2 \quad (\text{B.5})$$

is used to simplify the expression for \hat{m} . The estimate of T_A from a measurement v_A based upon the calibration set is

$$\hat{T}_A = \hat{m} v_A + \hat{b}. \quad (\text{B.6})$$

B.2 Unbiased Estimators

To show \hat{m} and \hat{b} are unbiased estimates of m and b , substitute

$$T_i = m v_i + b + \varepsilon_i \quad (\text{B.7})$$

into (B.4) which yields

$$\hat{m} = m + \frac{\sum (v_i - \langle v \rangle_n) \varepsilon_i}{\sum (v_i - \langle v \rangle_n)^2} \quad (\text{B.8})$$

where (B.5) is used to simplify the expression. Taking the expected value of (B.8) yields

$$E\{\hat{m}\} = m + \frac{\sum (v_i - \langle v_i \rangle_n) E\{\varepsilon_i\}}{\sum (v_i - \langle v_i \rangle_n)^2}. \quad (\text{B.9})$$

Since $E\{\varepsilon_i\} = 0$, \hat{m} is unbiased. It is straightforward to show that \hat{b} is also an unbiased estimator. It follows since \hat{m} and \hat{b} are unbiased estimators, the estimate \hat{T}_A obtained from the measurement v_A , i.e. $\hat{T}_A = \hat{m} v_A + \hat{b}$, is also unbiased. If $E\{\varepsilon_i\} \neq 0$, then \hat{m} , \hat{b} , and \hat{T}_A could be biased.

B.3 Uncertainty in \hat{T}_A

In this section, the measurement uncertainty is calculated for the LSR estimator given by (B.6). The uncertainty in \hat{T}_A is found by evaluating the expected value of the square of the difference between the estimated value and actual value, i.e.

$$\sigma_{\hat{T}_A}^2 = E \left\{ \left(\hat{T}_A - T_A \right)^2 \right\}. \quad (\text{B.10})$$

First a Taylor series expansion of the estimator, \hat{T}_A , about the mean of its random variables is performed. Then the series expansion of \hat{T}_A is substituted into (B.10) and the expected value is evaluated. In this presentation, all the random variables are assumed independent; uncertainty in the measurand voltage is σ_{v_A} , uncertainty in the calibration voltage measurements is σ_{v_i} , and uncertainty in the knowledge of the true reference temperatures, \bar{T}_i , is $\sigma_{\bar{T}_i}$.

The LSR estimator for the antenna brightness temperature is given by (B.6). The estimator can be rewritten as

$$\begin{aligned} \hat{T}_A &= \left(v_A - \langle v_i \rangle_n \right) \hat{m} + \langle T_i \rangle_n \\ &= \left(v_A - \langle v_i \rangle_n \right) \frac{\sum (v_i - \langle v_i \rangle_n) \bar{T}_i}{\sum (v_i - \langle v_i \rangle_n)^2} + \langle T_i \rangle_n. \end{aligned} \quad (\text{B.11})$$

where (B.4) has been substituted into (B.6). The estimator can be expressed as function of random variables, x_i 's, such as

$$\hat{T}_A = f(x_1, x_2, \dots, x_K) \quad (\text{B.12})$$

where $x_i \in \{v_A, v_1, \dots, v_n, T_1, \dots, T_n\}$. The multivariate Taylor series expansion of \hat{T}_A about the mean of the random variables is

$$\hat{T}_A = \sum_{j=0}^{\infty} \left\{ \frac{1}{j!} \left[\sum_{i=1}^K (x_i - \bar{x}_i) \frac{\partial}{\partial x_i} \right]^j f(x_1, x_2, \dots, x_K) \right\}_{x_1=\bar{x}_1, x_2=\bar{x}_2, \dots, x_K=\bar{x}_K} \quad (\text{B.13})$$

where $\bar{x}_i = E\{x_i\}$. The series expansion is well approximated by the truncation after the second term ($j=1$), thus yielding

$$\hat{T}_A = f(\bar{x}_1, \bar{x}_2, \dots, \bar{x}_K) + \sum_{k=1}^n (x_k - \bar{x}_k) f_{x_k} \quad (\text{B.14})$$

where

$$f_{x_i} = \frac{\partial}{\partial x_i} f(x_1, x_2, \dots, x_K) \Big|_{x_1=\bar{x}_1, x_2=\bar{x}_2, \dots, x_K=\bar{x}_K}. \quad (\text{B.15})$$

Substituting (B.14) into (B.10) and observing that the first term on the right hand side in (B.14) is equal to T_A , the measurement uncertainty is

$$\sigma_{T_A}^2 = \sum_{j=1}^K \sum_{k=1}^K E\{(x_k - \bar{x}_k)(x_j - \bar{x}_j)\} f_{x_j} f_{x_k}. \quad (\text{B.16})$$

By assuming that the random variables x_i 's are independent, $E\{(x_k - \bar{x}_k)(x_j - \bar{x}_j)\} = 0$ for $j \neq k$. Thus,

$$\begin{aligned} \sigma_{T_A}^2 &= \sum_{j=1}^K \sigma_{x_j}^2 f_{x_j}^2 \\ &= \sigma_{v_A}^2 f_{v_A}^2 + \sum_{i=1}^n \sigma_{v_i}^2 f_{v_i}^2 + \sum_{i=1}^n \sigma_{T_i}^2 f_{T_i}^2 \end{aligned} \quad (\text{B.17})$$

where $\sigma_{x_j}^2 = E\{(x_j - \bar{x}_j)^2\}$. Next evaluate the partial derivatives and substitute the relationship $\bar{v}_i = (\bar{T}_i - b)m^{-1}$. Noting that $m^2 \sigma_{v_A}^2 = \sigma_{T_A}^2$, $\sigma_{T_i}^2 = m^2 \sigma_{v_i}^2$ and $f_{v_i}^2 = m^2 f_{T_i}^2$, the uncertainty can be expressed as

$$\sigma_{T_A}^2 = \sigma_{T_A}^2 + \sum_{i=1}^n f_{T_i}^2 (\sigma_{T_i}^2 + \sigma_{\bar{T}_i}^2) \quad (\text{B.18})$$

where

$$f_{T_i} = (T_A - \langle \bar{T}_i \rangle_n) \frac{\bar{T}_i - \langle \bar{T}_i \rangle_n}{\sum_{i=1}^n (\bar{T}_i - \langle \bar{T}_i \rangle_n)} + \frac{1}{n} \quad (\text{B.19})$$

Substituting (B.19) into (B.18) yields

$$\begin{aligned}\sigma_{\hat{T}_A}^2 = & \sigma_{T_A}^2 + \frac{\sum(\sigma_{T_i}^2 + \sigma_{\bar{T}_i}^2)}{n^2} + \\ & \frac{(T_A - \langle \bar{T}_i \rangle_n)^2 \sum(\bar{T}_i - \langle \bar{T}_i \rangle_n)^2 (\sigma_{T_i}^2 + \sigma_{\bar{T}_i}^2)}{\left(\sum(\bar{T}_i - \langle \bar{T}_i \rangle_n)^2 \right)^2} + . \\ & \frac{2(T_A - \langle \bar{T}_i \rangle_n) \sum(\bar{T}_i - \langle \bar{T}_i \rangle_n)(\sigma_{T_i}^2 + \sigma_{\bar{T}_i}^2)}{n \cdot \sum(\bar{T}_i - \langle \bar{T}_i \rangle_n)^2}\end{aligned}\quad (\text{B.20})$$

B.4 Weighted Least Squares Regression

In Appendix B.1, estimates of the slope and offset were found from a set of n calibration measurements and the uncertainty in each measurement was allowed to be different. However in forming the slope and offset estimates, each calibration measurement was given equal weight. It is reasonable to assume that those measurements with greater uncertainty should be given less weight. In the following, estimates of the slope and offset are obtained from a set of calibration measurements where the measurements are weighted according to their level of uncertainty. The total measurement uncertainty is given for the case when weighted calibration measurements are used. Finally, optimal weights are found for the case where the measurements are treated as Gaussian random variables.

The calibration set is expressed as a set of equations given arbitrary weights,

$$\begin{aligned}w_1 T_1 &= w_1 m v_1 + w_1 b + w_1 \varepsilon_1 \\ w_2 T_2 &= w_2 m v_2 + w_2 b + w_2 \varepsilon_2 \\ &\vdots \\ w_n T_n &= w_n m v_n + w_n b + w_n \varepsilon_n\end{aligned}\quad (\text{B.21})$$

As in B.1, estimates of m and b are derived by minimizing the sum of the squared error. The weighted sum of squared errors is

$$E = \sum_{i=1}^n w_i^2 (v_i \hat{m} + \hat{b} - T_i)^2. \quad (\text{B.22})$$

Differentiating E with respect to \hat{m} and \hat{b} yields

$$\begin{aligned}\frac{\partial V}{\partial \hat{m}} &= \sum_{i=1}^n w_i^2 2v_i (v_i \hat{m} + \hat{b} - T_i) = 0 \\ \frac{\partial V}{\partial \hat{b}} &= \sum_{i=1}^n w_i^2 2(v_i \hat{m} + \hat{b} - T_i) = 0\end{aligned}\tag{B.23}$$

from which \hat{m} and \hat{b} are found. Solving (B.23) for \hat{m} and \hat{b} yields

$$\hat{m} = \frac{\sum (v_i - \langle v_i \rangle_n^w) w_i^2 T_i}{\sum w_i^2 (v_i - \langle v_i \rangle_n^w)^2} \tag{B.24}$$

$$\hat{b} = \langle T_i \rangle_n^w - \hat{m} \langle v_i \rangle_n^w \tag{B.25}$$

and where $\langle v_i \rangle_n^w$ and $\langle T_i \rangle_n^w$ are defined as

$$\begin{aligned}\langle v_i \rangle_n^w &= \frac{\sum w_i^2 v_i}{\sum w_i^2} \\ \langle T_i \rangle_n^w &= \frac{\sum w_i^2 T_i}{\sum w_i^2}\end{aligned}\tag{B.26}$$

Using (B.24) and (B.25) the antenna brightness temperature estimator is

$$\hat{T}_A = \left(v_A - \langle v_i \rangle_n^w \right) \frac{\sum_{i=1}^n (v_i - \langle v_i \rangle_n^w) T_i}{\sum_{i=1}^n (v_i - \langle v_i \rangle_n^w)^2} + \langle T_i \rangle_n^w. \tag{B.27}$$

To find the weights that minimize the MSE given by (B.22) the method of maximum likelihood is used. Assuming the set $\{\varepsilon_i\}$'s are zero-mean Gaussian random variables with variance given by $\sigma_{\tilde{T}_i}^2 = \sigma_{T_i}^2 + \sigma_{\varepsilon_i}^2$, the MSE is minimized by maximizing the likelihood function.

The likelihood function is given by

$$L(m, b) = \prod_{i=1}^n f(T_i | v_i) = \prod_{i=1}^n \frac{\exp\left(\frac{-1}{2\sigma_{\tilde{T}_i}^2} (T_i - mv_i - b)^2\right)}{\sqrt{2\pi} \sigma_{\tilde{T}_i}}. \tag{B.28}$$

The maximum likelihood estimates of m and b are the values \hat{m} and \hat{b} that maximize $L(m, b)$.

The estimates are obtained by differentiating the logarithm of $L(\hat{m}, \hat{b})$ with respect to \hat{m} and \hat{b} , and setting the derivative equal zero. Thus, \hat{m} and \hat{b} are found by solving the pair of equations,

$$\begin{aligned}\frac{\partial L}{\partial \hat{m}} &= \sum_{i=1}^n \frac{v_i}{\sigma_{T_i}^2} (v_i \hat{m} + \hat{b} - T_i) = 0 \\ \frac{\partial L}{\partial \hat{b}} &= \sum_{i=1}^n \frac{1}{\sigma_{T_i}^2} (v_i \hat{m} + \hat{b} - T_i) = 0.\end{aligned}. \quad (\text{B.29})$$

Comparing equations (B.29) and (B.23) the weights that correspond to a maximum in the likelihood function are

$$w_i \propto \frac{1}{\sigma_{T_i}}. \quad (\text{B.30})$$

The weights given by (B.30) yield optimum estimates of \hat{m} and \hat{b} when ε_i 's are zero-mean Gaussian random variables. For the case where the uncertainty in each calibration measurement is the same, each measurement is given equal weight. It is convenient but not necessary to normalize the weights according to

$$\sum w_i^2 = 1 \quad (\text{B.31})$$

by which the proportionality constant in (B.29) becomes

$$\sigma = \sqrt{\sum \sigma_{T_i}^2}. \quad (\text{B.32})$$

Evaluating the uncertainty in \hat{T}_A when weighted least square regression is used as was done to arrive at (B.20) in Appendix B.3 yields

$$\begin{aligned}\sigma_{\hat{T}_A}^2 &= \sigma_{T_A}^2 + \frac{\sum w_i^4 (\sigma_{T_i}^2 + \sigma_{\bar{T}_i}^2)}{\left(\sum w_i^2\right)^2} + \left(T_A - \langle \bar{T}_i \rangle_n^w\right)^2 \frac{\sum \left(T_i - \langle \bar{T}_i \rangle_n^w\right)^2 w_i^4 (\sigma_{T_i}^2 + \sigma_{\bar{T}_i}^2)}{\left(\sum w_i^2 \left(T_i - \langle \bar{T}_i \rangle_n^w\right)^2\right)^2} + \\ &\quad 2 \left(T_A - \langle \bar{T}_i \rangle_n^w\right) \frac{\sum \left(T_i - \langle \bar{T}_i \rangle_n^w\right) w_i^4 (\sigma_{T_i}^2 + \sigma_{\bar{T}_i}^2)}{\sum w_j^2 \sum w_i^2 \left(T_i - \langle \bar{T}_i \rangle_n^w\right)^2}.\end{aligned}. \quad (\text{B.33})$$

APPENDIX C

CODE TO CALCULATE SYMBOLIC SOLUTIONS

The following code is written to run using Matlab[®] with its Symbolic Math Toolbox. The symbolic equations generated by this program are used by other Matlab routines to generate Figs. 21 - 22.

```
%rad_uncert4_extcal.m
%
%This program generates the equations used to simulate the performance of a radiometer which uses
%noise source injection, an internal blackbody, and a two-point external
%calibration as described in Chapter 4.7.2. The internal calibration
%estimator uses Vr and Vr_n to solve for Trec and then uses Va and Va_n to
%solve for Ta. The error in the estimate is then calculated. Next the
%equations for the external calibration are defined and an estimate of the
%equivalent noise source temperature is calculated followed by the
%calculation of the error in the estimate.
%
%%%%%SYMBOLS USED IN THE SYMBOLIC COMPUTATION
clear
%Internal calibration variables
syms sTa sTr %scene temperature, reference temperature
syms sVa sVa_n sVr sVr_n %output voltage: scene, scene + ND1, ref, ref+ND1
syms sTn %Noise diode temperature
syms sL1 sTL1 %Losses 1-3, physical temperatures of losses 1-3
syms sG sTrec %Gain, Receiver noise, zero offset
syms su_L1 su_Tn su_Tr su_TL1 %uncertainty in the knowledge
syms sTnp su_Tnp %apparent noise source temperature
syms sdV_Ta_ap sdV_Ta_n_ap sdV_Tr_ap sdV_Tr_n_ap %NEDT of internal voltages when observing Ta

%Variables used for the external calibration equations
syms sTa1 sTa2 sTa3 %External calibration temperatures
syms sVa1 sVa_n1 sVr1 sVr_n1 %External calibration voltages, Reference 1
syms sVa2 sVa_n2 sVr2 sVr_n2 %External calibration voltages, Reference 2
syms su_Ta1 su_Ta2 %uncertainty in knowledge of external temperatures
syms sdV_Ta_ap1 sdV_Ta_n_ap1 sdV_Tr_ap1 sdV_Tr_n_ap1 %NEDT of internal voltages when observing Ta1
syms sdV_Ta_ap2 sdV_Ta_n_ap2 sdV_Tr_ap2 sdV_Tr_n_ap2 %NEDT of internal voltages when observing Ta2

%%%%%INTERNAL CALIBRATION EQUATIONS
%Output voltage equations, Output voltage equation set to = 0
%Scene alone
intV.Va = ( sTa*sL1 + (1-sL1)*sTL1 + sTrec )*sG;
intV.Va0 = -sVa + intV.Va;
%scen+noise
intV.Va_n = intV.Va + sTn*sG;
intV.Va_n0 = -sVa_n + intV.Va_n;
%reference
intV.Vr = ( sTr*sL1 + (1-sL1)*sTL1 + sTrec )*sG;
intV.Vr0 = -sVr + intV.Vr;
%ref + noise
intV.Vr_n = intV.Vr + sTn*sG;
intV.Vr_n0 = -sVr_n + intV.Vr_n;
```

```

%%%%%DERIVE INTERNAL CALIBRATION ESTIMATOR
%Use Vr and Vr_n measurements to derive estimate of Trec.
%Substitute Trec into Va and Va_n, and use Va and Va_n to estimate Ta and
%G. Substitute result for Trec back into Va and Va_n equations.

intCal_Trec = solve(intV.Vr0,intV.Vr_n0,'sG','sTrec');
intV.Va0Trec = subs(intV.Va0,'sTrec',intCal_Trec.sTrec);
intV.Va_n0Trec = subs(intV.Va_n0,'sTrec',intCal_Trec.sTrec);

%Solve Va0 and Va_n to obtain estimator for Ta
intCal = solve(intV.Va0Trec,intV.Va_n0Trec,'sTa','sG');
Est.Ta = intCal.sTa;
Est.Ta= simple(Est.Ta); %Simplify expression
sTnn =sTnp*sL1; %Substitute expression for Tnp
Est.Ta = subs(Est.Ta,'sTn', sTnn) %This is the internal calibration estimator

%%%%%CALCULATE THE ERROR IN THE ESTIMATOR
%Calculate derivitives w.r.t. all random variables
diff_Va = simple(diff(Est.Ta, sVa));
diff_Va_n = simple(diff(Est.Ta,sVa_n));
diff_Vr = simple(diff(Est.Ta, sVr));
diff_Vr_n = simple(diff(Est.Ta, sVr_n));
diff_Tr = simple(diff(Est.Ta, sTr));
diff_Tnp = simple(diff(Est.Ta, sTnp));

%Calculate the sum square of all error terms
Err_Est.Ta = (diff_Va.^2)*(sdV_Ta_ap.^2) + (diff_Va_n.^2)*(sdV_Ta_n_ap.^2) + ...
             (diff_Vr.^2)*(sdV_Tr_ap.^2) + (diff_Vr_n.^2)*(sdV_Tr_n_ap.^2) + ...
             (diff_Tr.^2)*(su_Tr.^2) + (diff_Tnp.^2)*(su_Tnp.^2);

%Substitute in the mean parameters of TBs for the voltages
Err_Est.Ta = subs(Err_Est.Ta,{'sVa', 'sVa_n', 'sVr', 'sVr_n'}, ...
                  {intV.Va, intV.Va_n, intV.Vr, intV.Vr_n});
Err_Est.Ta = subs(Err_Est.Ta,{'sTn'}, {sTnn});
Err_Est.Ta = simple(Err_Est.Ta); %This is the error for the internally calibrated Ta

%%%%%EXTERNAL CALIBRATION CODE
%%%%%ESTABLISH EQUATIONS USED FOR EXTERNAL CALIBRATION
intV.Va1 = (sTa1*sL1 + (1-sL1)*sTL1 + sTrec )*sG;
intV.Va_n1 = intV.Va1 + sTn*sG;
intV.Vr1 = (sTr*sL1 + (1-sL1)*sTL1 + sTrec )*sG; %uses same reference temperature as Ta measurement
intV.Vr_n1 = intV.Vr1 + sTn*sG;

intV.Va2 = (sTa2*sL1 + (1-sL1)*sTL1 + sTrec )*sG;
intV.Va_n2 = intV.Va2 + sTn*sG;
intV.Vr2 = (sTr*sL1 + (1-sL1)*sTL1 + sTrec )*sG;
intV.Vr_n2 = intV.Vr2 + sTn*sG;

intV.Va3 = (sTa3*sL1 + (1-sL1)*sTL1 + sTrec )*sG;
intV.Va_n3 = intV.Va3 + sTn*sG;

```

```

intV.Vr3 = ( sTr*sL1 + (1-sL1)*sTL1 + sTrec )*sG;
intV.Vr_n3 = intV.Vr3 + sTn*sG;

%Generate Ta estimator using external 2-point calibration measurements
ExtV.T1 = Est.Ta;
ExtV.T1 = subs(ExtV.T1, {'sVa', 'sVa_n', 'sVr', 'sVr_n'}, {'sVa1', 'sVa_n1', 'sVr1', 'sVr_n1'});

ExtV.T2 = Est.Ta;
ExtV.T2 = subs(ExtV.T2, {'sVa', 'sVa_n', 'sVr', 'sVr_n'}, {'sVa2', 'sVa_n2', 'sVr2', 'sVr_n2'});

%%%%%CALCULATE THE ESTIMATOR FOR Tnp
%Calculate the sum squared error in external calibrations
SumSqr = (ExtV.T1 -sTa1).^2 +(ExtV.T2 -sTa2).^2; %
SumSqr = simple(subs(SumSqr,'sTn', sTnn))

%Differentiate the sum squared error and solve for Tnp
difSumSqr.Tn = diff(SumSqr,sTnp);
SolvTnp = solve(difSumSqr.Tn, 'sTnp')
SolvTnp = simple(SolvTnp); %This is the estimator for Tnp

%%%%%CALCULATE THE ERROR IN THE ESTIMATE OF Tnp
%Calculate derivitives w.r.t. all random variables
diff_Va1 = simple(diff(SolvTnp, sVa1));
diff_Va_n1 = simple(diff(SolvTnp,sVa_n1));
diff_Vr1 = simple(diff(SolvTnp, sVr1));
diff_Vr_n1 = simple(diff(SolvTnp, sVr_n1));
diff_Va2 = simple(diff(SolvTnp, sVa2));
diff_Va_n2 = simple(diff(SolvTnp,sVa_n2));
diff_Vr2 = simple(diff(SolvTnp, sVr2));
diff_Vr_n2 = simple(diff(SolvTnp, sVr_n2));
diff_Ta1 = simple(diff(SolvTnp, sTa1));
diff_Ta2 = simple(diff(SolvTnp, sTa2));
diff_Tr = simple(diff(SolvTnp, sTr));

%Calculate the sum square of all error terms, break sum into two sets and
%add together at end. (This simplifies the computation for Matlab.)
%Substitute back into the expresions the expressions for the voltages.
Err_Ext.Ta1 =(diff_Va1.^2)*(sdV_Ta_ap1.^2) + (diff_Va_n1.^2)*(sdV_Ta_n_ap1.^2) + ...
              (diff_Vr1.^2)*(sdV_Tr_ap1.^2) + (diff_Vr_n1.^2)*(sdV_Tr_n_ap1.^2) + ...
              (diff_Ta1.^2)*(su_Ta1.^2) + (diff_Tr.^2)*(su_Tr.^2); %

Err_Ext.Ta1 = subs(Err_Ext.Ta1, { 'sVa1', 'sVa_n1', 'sVr1', 'sVr_n1','sVa2', 'sVa_n2', 'sVr2', 'sVr_n2', }, ...
                  {intV.Va1, intV.Va_n1, intV.Vr1, intV.Vr_n1, intV.Va2, intV.Va_n2, intV.Vr2, intV.Vr_n2});
Err_Ext.Ta1 = subs(Err_Ext.Ta1,'sTn', sTnn);

Err_Ext.Ta2 =(diff_Va2.^2)*(sdV_Ta_ap2.^2) + (diff_Va_n2.^2)*(sdV_Ta_n_ap2.^2) + ...
              (diff_Vr2.^2)*(sdV_Tr_ap2.^2) + (diff_Vr_n2.^2)*(sdV_Tr_n_ap2.^2) + ...
              (diff_Ta2.^2)*(su_Ta2.^2); %

Err_Ext.Ta2 = subs(Err_Ext.Ta2, { 'sVa1', 'sVa_n1', 'sVr1', 'sVr_n1','sVa2', 'sVa_n2', 'sVr2', 'sVr_n2', }, ...
                  {intV.Va1, intV.Va_n1, intV.Vr1, intV.Vr_n1, intV.Va2, intV.Va_n2, intV.Vr2, intV.Vr_n2});
Err_Ext.Ta2 = subs(Err_Ext.Ta2,'sTn', sTnn);

Err_Ext.Tnp = Err_Ext.Ta1 + Err_Ext.Ta2; %This is the error in the estimator of Tnp based upon the two-point
calibration.

save rad_uncert4_extrnl_cal %Save external calibration equations for other programs to use.

```